University of Strathclyde

Department of Naval Architecture, Ocean and Marine Engineering

# Numerical investigation of ROV deployment onboard a small offshore service vessel for offshore wind farm O&M

YULIN DENG

The thesis submitted in fulfilment of the requirements for the degree of

Doctor of Philosophy

August 2024

# Acknowledgement

I would like to begin by expressing my deepest gratitude to my supervisor, Prof. Longbin Tao, whose expertise and unwavering support have been invaluable throughout my PhD journey. His guidance, particularly in the field of hydrodynamics, has been instrumental in shaping the foundation of my academic career. Prof. Tao's consistent encouragement has not only helped me navigate the challenges of my research but has also inspired me to pursue future endeavors with confidence.

I am also thankful to Dr. Xiudi Ren from PowerChina Huadong Engineering Corporation Limited and Dr. Martin Nuernberg from O.S. Energy (UK) for their significant contributions to my research. Their assistance in developing the numerical model and providing validation data was crucial, and I deeply appreciate their generous support.

My sincere thanks go to Mrs. Susan Pawson and the staff at the Department of NAOME for their help with administrative and technical matters. Their support ensured that I could focus on my research without unnecessary distractions.

I am incredibly grateful to my colleagues and friends at the University of Strathclyde, whose camaraderie and encouragement have been a constant source of strength. Their support in both academic and personal matters made my time in Scotland more enjoyable and fulfilling.

A special note of appreciation goes to my parents, whose unwavering support and wise counsel have guided me throughout my life and academic journey. Their belief in my decisions regarding my studies and career has been a source of immense pride for me.

Lastly, I want to extend my heartfelt thanks to my girlfriend, Yuting Huang. Despite pursuing her own PhD in China, she has been a pillar of support throughout my PhD journey. Her trust and understanding allowed us to overcome the challenges of long-distance, and I am profoundly grateful for her presence in my life.

# List of Publications

Deng, Y., Ren, X., Nuernberg, M. and Tao, L., 2024. Launch and recovery of a work class ROV through wave zone in small offshore service vessel. Ocean Engineering, 309, p.118541.

Yulin Deng, Longbin Tao, Xiudi Ren, Martin Nuernberg, (2024): Numerical analysis of ROV deployment onboard a small OSV coupled with a floating wind turbine by a single point mooring system. Renewable Energy. (submitted to journal 2 August 2024)

Deng Y, Tao L, Ren X, 2024. Research on the interaction between single point mooring service vessel and floating wind turbine. Proceedings of the 13th National Conference on Fluid Mechanics CSTAM2024. The Chinese Society of Theoretical and Applied Mechanics. August 9-13, 2024, Harbin, China.

Deng, Y., Ren, X., Nuernberg, M. and Tao, L., 2023, June. Dynamic Analysis of Launching and Recovering ROV. Proceedings of the ASME 02023 42nd International Conference on Ocean, Offshore and Arctic Engineering (OMAE2023-102185). American Society of Mechanical Engineers. June 11-16, 2023, Melbourne, Australia.

# Table of Contents

# Abstract

Aimed at significant cost reduction and reducing the overall greenhouse gas (GHG) emission during the operation, the deployment of remotely operated underwater vehicle (ROV) from a small offshore service vessel (OSV) based on single point mooring system (SPMS) method is recently adopted in offshore renewable energy sector. However, the tension spike in wire, also known as snap load, often occurs when the ROV passes through the wave zone in launching and lifting operation of deployment. This study developed a coupled numerical model of ROV deployment onboard a small OSV positioned by a SPMS for subsea inspection of a fixed or floating offshore wind turbine. The numerical model for predicting wire tension during launch and recovery of ROV is developed and validated by wave flume test of a 1:10 scaled model.

The numerical simulations reveal that the ROV deployment at vessel stern along with an appropriate reduction of horizontal distance from the hull are reliable safety strategies for reducing wire tension. By adopting the new deployment strategy, the annual operational capacity can be expanded by approximately 6% when the safe operational limit of ROV under a significant wave height of 1.25 m. Based on the comprehensive numerical simulation, the newly developed safe operating envelope provides a practical recommendation for onboard ROV operation in the operations and maintenance (O&M) of offshore wind farms.

As a typical practical offshore operation involving multiple floating body dynamics, the dynamic response characteristics of umbilical cable of ROV, connecting lines of SPMS, and mooring lines of floating offshore wind turbines (FOWT) are investigated under the environmental conditions of the northern North Sea. The coupled numerical model was first validated against the maximum and average tension measurements of connecting lines obtained from full-scale OSV operations at sea for subsea inspection of two different fixed wind turbines. Numerical simulations of coupled OSV-FOWT system indicated that the dynamic tension in umbilical cable and mooring lines, primarily determining the environmental limits of ROV deployment and safe operation, is influenced by wind-wave misalignment and the relative distance between OSV and FOWT. The relationships and safe operational ranges of umbilical cable, connecting

lines, and mooring lines were examined in detail to provide further guidance for onboard ROV operations in offshore wind farm maintenance.

# Abbreviations

| | |
|---|---|
| ASV | autonomous surface vessel |
| CFD | computational fluid dynamics |
| DP | dynamic positioning |
| FOWT | floating offshore wind turbine |
| FPSO | floating production storage and offloading |
| GHG | greenhouse gas |
| IMR | inspection, maintenance and repair |
| LARS | launch and recovery system |
| LC | low condition |
| MC | medium condition |
| HC | high condition |
| O&M | operations and maintenance |
| OSV | offshore service vessel |
| ROV | remotely operated underwater vehicle |
| SOV | service operation vessel |
| SPH | smoothed particle hydrodynamics |
| SPMS | single point mooring system |
| TLP | tension leg platform |
| TMS | tether management system |

# List of Figures

# List of Tables

## List of symbols

| | |
|---|---|
| $\Phi(x, y, z, t)$ | total velocity potential |
| $\Phi^{(1)}(x, y, z, t)$ | total first-order velocity potential |
| $\Phi^{(2)}(x, y, z, t)$ | total second-order velocity potential |
| $\omega$ | circular frequency of incident wave |
| $\phi^{(1)}(x, y, z)$ | complex first-order time-independent total velocity potential |
| $\phi_I^{(1)}$ | complex first-order time-independent incident wave potential |
| $\phi_D^{(1)}$ | complex first-order time-independent diffraction wave potential |
| $\phi_R^{(1)}$ | complex first-order time-independent radiation wave potential |
| $N_i$ | $i$-th body in multi-body platform system |
| $N$ | total number of bodies |
| $\xi_m^{(1)N_i}$ | first-order complex amplitude of the oscillatory motion of body $N_i$ in $m$-th mode |
| $\phi_m^{(1)N_i}$ | first-order unit-amplitude radiation potential for body $N_i$ in $m$-th mode |
| $R^I$ | inertia force vector |
| $R^D$ | damping force vector |
| $R^S$ | internal structural reaction force vector |
| $R^E$ | external force vector |
| $r, \dot{r}, \ddot{r}$ | structural displacement, velocity and acceleration vectors |
| $M^S$ | structural mass matrix |
| $M^F(r)$ | mass matrix accounting for internal fluid flow |
| $M^H(r)$ | displacement-dependent hydrodynamic mass matrix |
| $C^S(r)$ | internal structural damping |
| $C^H(r)$ | hydrodynamic damping matrix |
| $C^D(r, \dot{r})$ | matrix of specified discrete dashpot dampers |
| $M_t$ | tangential mass- at time |
| $C_t$ | damping- at time |
| $K_t$ | stiffness matrices computed at time |
| $\Delta r_t$ | incremental displacement |
| $\Delta \dot{r}_t$ | velocity |

| | |
|---|---|
| $\Delta\ddot{r}_t$ | acceleration |
| $\Delta R_t^E$ | external force vectors |
| $\widehat{K}_t$ | effective stiffness |
| $\Delta\widehat{R}_t$ | effective incremental load vector |
| $\gamma, \beta, \theta$ | time integration parameters based on the Newmark β-family method |
| $K_t$ | stiffness matrix |
| $f$ | frequency |
| F | umbilical axial force |
| H | wave height |
| k | umbilical axial stiffness |
| M | ROV mass |
| T | wave period |
| ν | winch speed |
| $x(t)$ | time-domain signal |
| $X(f)$ | frequency-domain signal |

# 1 Introduction

## 1.1 Research background

One of the greatest threats of this century is climate change, which has already had a significant impact on many regions around the world. The frequency and intensity of extreme weather events have increased, leading to phenomena such as rising sea levels, glacier melting, droughts, and floods, posing severe challenges to ecosystems and human societies. Greenhouse gas emissions in the energy sector account for two-thirds of the global total, making it a major driver of climate change. The use of traditional fossil fuels not only results in substantial carbon dioxide emissions but also brings air pollution and causes health issues (Figure 1.1). Therefore, to address climate change and provide affordable energy, the world urgently needs a radical transformation in energy technology, driving breakthroughs in clean, sustainable, and renewable energy technologies. This will not only help reduce greenhouse gas emissions but also promote economic growth and create job opportunities (IRENA, 2020).

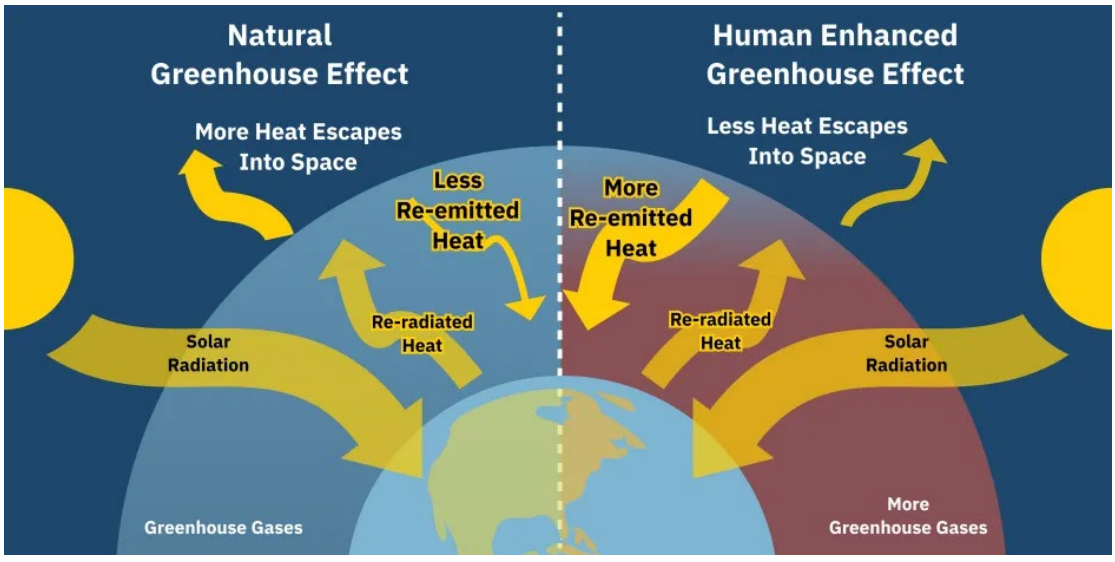


Figure 1.1 The earth's greenhouse effect (University of Michigan, 2023).

Policies formulated by governments during the 2015 Paris Agreement, current energy plans, other planning policies and goals, the widespread application of renewable energy, and continually improving energy efficiency all play crucial roles in achieving these objectives. The signing of the Paris Agreement marked an unprecedented global

consensus on addressing climate change, with countries committing to limit global temperature increases by reducing greenhouse gas emissions. In this context, many countries have set ambitious renewable energy and energy efficiency targets, such as Germany's "Energiewende" and China's "14th Five-Year Plan" (Zhang and Wang, 2022). Additionally, international cooperation and technology transfer have been instrumental in promoting global energy transitions. Renewable energy, energy efficiency, and the electrification of energy consumption are vital for achieving emission reduction targets. These measures not only reduce dependence on fossil fuels but also enhance energy security and sustainability.

With the help of batteries and other supporting technologies, the application of renewable energy technologies in various countries has proven to be effective and cost-efficient. The development of battery storage technology has enabled intermittent renewable energies such as wind and solar power to supply electricity more stably, balancing supply and demand fluctuations. Today, the global potential of renewable energy, whether for direct energy use or as raw materials, is greater than ever before, making it crucial in achieving zero-emission targets. Currently, renewable technologies dominate the global market for new sustainable energy production. Among renewable energies, wind power is the fastest-growing electricity production technology (Singh and Parida, 2013). Wind power is becoming an increasingly cheaper and cost-effective electricity source in many markets and is expected to be fully competitive in the coming years. Many innovative solutions have been developed to make power systems and grids more resilient, allowing for more efficient and cost-effective utilization and dissemination of onshore and offshore wind energy systems.

Offshore wind energy technology has been one of the fastest-growing renewable energy systems in the past decade. With significant reductions in technology costs, major breakthroughs, and improvements in supply chain efficiency, it has achieved remarkable success in various markets, paving the way for further investment. Due to these characteristics, offshore wind energy has become an attractive technology globally. Offshore wind energy not only harnesses higher and more stable wind resources but also avoids land use and noise issues that onshore wind energy might face. Many countries have developed large-scale offshore wind farm projects in coastal areas worldwide, such as the UK's "Dogger Bank" project (Figure 1.2) and China's "Jiangsu

Offshore Wind Power Base." This capability has significantly contributed to the decarbonization of the power sectors in many countries. By the end of 2020, 35.3 GW of offshore wind power capacity had been installed globally, with 90% concentrated in the North Atlantic and North Sea. The UK, China, Germany, the Netherlands, Belgium, and Denmark are the major countries in this field (Bilgili and Alphan, 2022). Moreover, with further technological advancements and continued cost reductions, offshore wind energy is expected to play a crucial role in future power production systems, further driving the global energy transition and the achievement of climate goals.

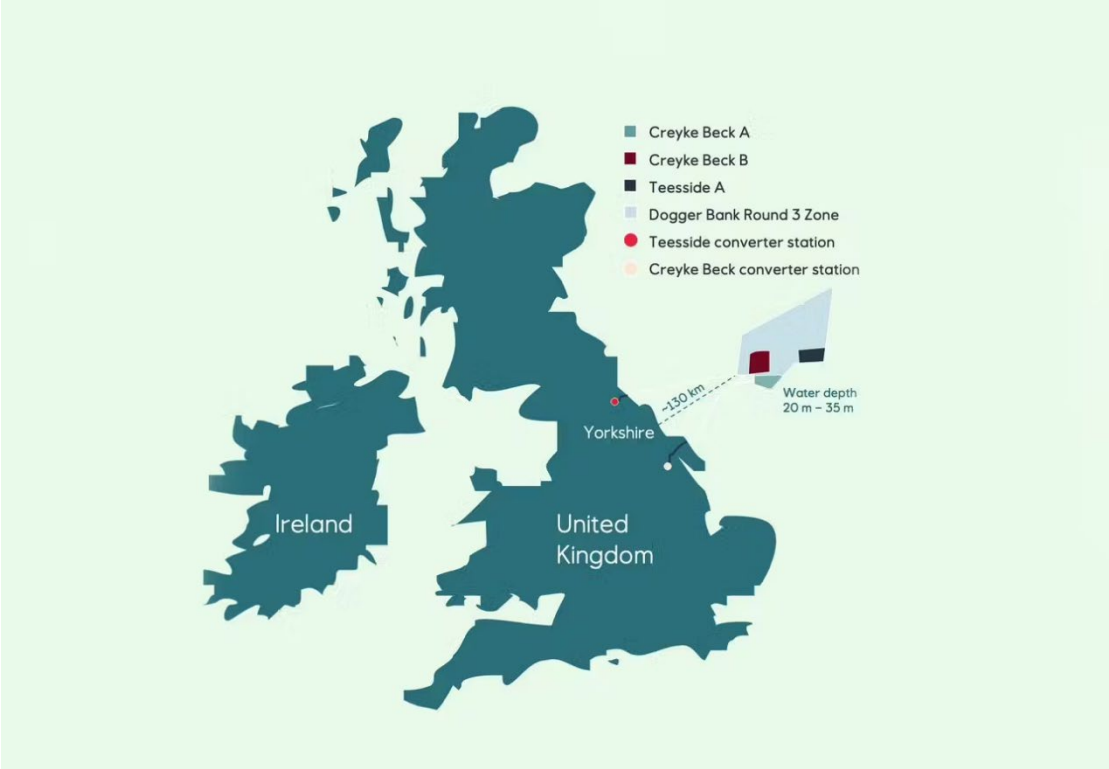


Figure 1.2 The Dogger Bank offshore wind farm will consist of three projects, Creyke Beck A, Creyke Beck B and Teesside A (Offshore magazine, 2019).

Offshore wind farms are typically built in continental shelf areas, approximately 10 kilometers from the coast and at depths of around 10 meters (Zhixin et al., 2009). Unlike onshore wind turbines, offshore turbines need to be secured to the seabed, necessitating more robust support structures. These support structures are typically made of steel or concrete to withstand the strong oceanic forces, including wind, waves, and currents. Submarine power cables are essential for power transmission and must be designed to

withstand long-term operation in a saline environment, ensuring durability and resistance to corrosion. Special vessels and equipment, such as heavy-lift ships and underwater robots, are required for construction and routine maintenance to ensure safety and efficiency. These factors result in high costs, doubling or tripling the costs compared to onshore projects. However, offshore wind farms have many advantages, such as avoiding land-use disputes, no special geological requirements, high wind speeds, and abundant wind energy. With advancements in technology and accumulated experience, the efficiency and economic viability of these wind farms will further improve, prompting more countries and regions to invest in offshore wind energy.

For many years, offshore oil and gas production was primarily confined to shallow waters along coastal regions. These shallow waters had more accessible oil and gas resources due to lower technical requirements and costs. However, as these resources became depleted, the industry began to expand into deeper waters. Advanced seismic exploration technologies and more efficient drilling equipment made it feasible to exploit resources in deepwater and ultra-deepwater areas. Deepwater oil and gas fields involve more complex engineering techniques, such as using floating drilling platforms and subsea production systems that can operate in waters as deep as 1500 m or more. The industry typically categorizes water depths as follows: shallow water (less than 400 m), deepwater (around 1500 m), and ultra-deepwater (greater than 1500 m). This progression into deeper waters has brought new opportunities and challenges to the offshore oil and gas industry. Discovering and exploiting deepwater oil and gas fields have not only increased global reserves but also driven innovation in related technologies and equipment. As global energy demand continues to grow, the development of deepwater and ultra-deepwater oil and gas resources will remain an essential part of the industry.

As oil and gas operations moved into deeper waters, fixed platforms became unsuitable, leading to the development of various floating structures such as floating production storage and offloading (FPSO), spar platform, semi-submersible, and tension leg platform (TLP). These floating platforms can operate stably in deepwater and ultra-deepwater environments, adapting to harsher ocean conditions. In the 21st century, the offshore energy industry has undergone significant diversification, expanding from traditional oil and gas exploration to include renewable energy sources such as offshore

wind. Meanwhile, offshore wind farms have emerged as a frontier in renewable energy, featuring towering wind turbine structures designed to withstand harsh marine environments. These wind turbines, comprising foundations, towers, nacelles, and rotor assemblies, are strategically placed in coastal waters to maximize energy production while minimizing visual impact on land. With the continuous advancement of offshore wind technology, the design and materials of these wind turbines are also constantly improving to enhance their durability and efficiency.

Offshore wind turbine foundations come in two main types: fixed and floating. Fixed foundations are suitable for shallower waters, typically used in depths not exceeding 50 meters. Common fixed foundations include monopile foundations, gravity-based foundations, and jacket foundations. Monopile foundations are large steel tubes driven into the seabed, suitable for medium-shallow waters. Gravity-based foundations, made of concrete or steel, rely on their weight to stay anchored to the seabed and are suitable for soft seabed. Jacket foundations are space frame structures made of steel pipes, used in slightly deeper waters. Floating foundations, on the other hand, can be used in deeper waters, typically beyond 50 meters. These include floating platforms, TLPs, and semi-submersible platforms. Floating foundations are anchored to the seabed by chains or cables, providing greater stability and adaptability. The choice of foundation type depends on water depth, seabed conditions, and environmental factors. Figure 1.3 illustrates the main types of offshore wind turbine foundations classified by different installation methods. As offshore wind technology continues to advance, new foundation designs and construction methods are continually emerging, enabling these wind turbines to operate stably in increasingly complex and variable marine environments.

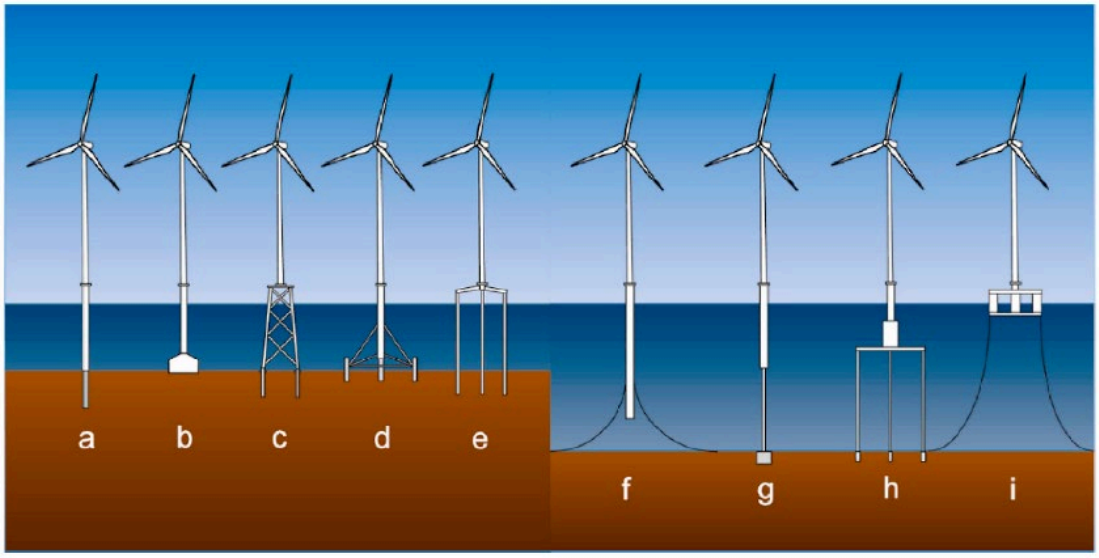


Figure 1.3 Types of offshore wind turbine platforms: (a) monopile, (b) gravity-based platform, (c) jacket, (d) tripod, (e) triple, (f) spar, (g, h) tension-legged platform, and (i) semi-submersible (Chen et al., 2024).

Inspection, maintenance and repair (IMR) are critical terms in underwater intervention operations, primarily aimed at ensuring the safety, reliability, and cost-effectiveness of subsea facilities. These operations are not only essential for extending the lifespan of offshore assets but also crucial for maintaining their sustainable operation. IMR activities are driven by industry demands, particularly in reducing operational costs, mitigating financial and operational risks, and promoting the effective application of new technologies.

In the context of IMR operations, the inspection of subsea structures generally involves visual inspections and non-destructive testing. Visual inspections are typically conducted using camera equipment, while non-destructive testing techniques are applied to ensure the safety and structural integrity of the assets. Maintenance and repair activities are carried out throughout the asset's lifecycle, focusing on timely intervention to prevent significant failures.

Historically, IMR operations in the offshore oil and gas industry relied on floating vessels and modified supply ships. However, between 2008 and 2009, the emergence of dedicated IMR vessels marked a significant shift in industry standards. Companies

began utilizing specially designed vessels such as Subsea 7 equipped with conventional IMR tools. These tools include ROVs, control cabins or control rooms, launch and recovery system (LARS), tether management system (TMS), and potentially additional options such as object recovery systems. These specialized vessels are typically equipped with dynamic positioning (DP) system, a satellite-based navigation technology that uses powerful thrusters to lock the vessel in place at the operational site. Additionally, some vessels feature moon pools located amidships, facilitating the deployment and retrieval of equipment, while onboard cranes are used to deploy ROVs into the water through the moon pool. The ROVs are tethered to the vessel via an umbilical cable, and the pilots control the ROVs remotely from the control room.

IMR operations are typically executed by specialized subsea contractors, who often charter crewed dedicated vessels from shipowners or maritime companies. Large operators generally prefer to secure long-term charters, often leasing vessels year-round to ensure continuous operational capacity. In contrast, smaller operators may opt for short-term charters to meet specific operational needs. An IMR vessel may host up to 70 personnel, belonging to as many as five different companies, working in close coordination to ensure the smooth execution of operations.

From the moment the vessel departs for the operational site, routine maintenance and operational preparations commence. Upon arrival, the vessel is usually positioned near fixed offshore facilities, such as drilling platforms, with the DP system securing the vessel in place. Each operational scenario is unique, necessitating the selection of an appropriate ROV, particularly when large ROVs require more stringent planning and preparation. The operational procedure includes a series of checklists, with pre-dive and post-dive procedures being critical components. Pre-dive procedures involve crew briefings, vehicle preparation, and the completion of pre-dive checklists, while post-dive procedures include post-dive checklists and equipment dismantling.

### 1.2 ROV system for O&M of offshore wind farms

The rapid growth of offshore wind installation, along with subsequent operations and maintenance activities, has placed significant pressure on the availability of personnel and vessels. In 2023, the global installed capacity of offshore wind power reached

72,663 MW, reflecting a 24% increase from 2022 (Statista, 2024b). As the scale of offshore wind farms continues to expand, with further construction aimed at leveraging larger turbines and more favourable wind conditions, the demand for effective operations and maintenance strategies has intensified.

The size of wind turbine is also increasing, with larger blades capable of capturing more wind, which, in turn, generates greater torque to drive the generator housed in the nacelle. Moreover, larger blades boast higher aerodynamic efficiency, resulting in less energy loss when entering the transmission system. The towers supporting these blades are also becoming taller, partly to provide additional structural support for the larger blades and partly because greater heights are more conducive to electricity generation. For instance, the first commercial offshore wind farm in the UK, North Hoyle, installed in 2003, used 2 MW Vestas turbines with a rotor diameter of 80 m (Carter, 2007). In contrast, the Siemens Gamesa SG14-222 DD wind turbine, to be commercially deployed at the Moray West wind farm in 2024, features a rotor diameter of 222 m and a capacity of 14 MW (Siemens Gamesa, 2023).

Despite the initial slow development of offshore wind power, the number of operational offshore wind farms has tripled in the past decade compared to the previous ten years, with numerous new projects currently underway. As of June 2024, China leads the world with 129 operational offshore wind farms, followed by the UK with 39, Germany with 30, and Vietnam with 26 (Statista, 2024a). This growth is largely attributed to economies of scale and technological advancements required for wind farm construction, driven mainly by the cost-reduction pressures of the competitive contracts for difference system introduced in 2014.

The scale of wind turbines in recent projects has significantly increased compared to earlier ones. For instance, the Hornsea One wind farm in the UK, commissioned in 2019, features 174 Siemens Gamesa SWT-7.0-154 turbines with a rotor diameter of 154 m and a rated power of 7,000 kW. By contrast, the Hornsea Project Two, commissioned in 2022, includes 165 Siemens Gamesa 8.0-167 DD turbines with a rotor diameter of 167 m and a rated power of 8,000 kW. This is a stark contrast to the Blyth wind farm, commissioned in 2000, which had only two turbines with a rotor diameter of 66 meters and a total generation capacity of just 4 MW.

As wind farms grow in capacity and scale and are located farther from shore, the demand for vessels capable of accommodating more specialized personnel and equipment has also increased. Consequently, the industry is witnessing a shift from crew transfer vessel to service operation vessel (SOV) for larger and deeper offshore wind farms, both fixed and floating. The demand for SOVs, which are essential for the safe, efficient, and economical installation and maintenance of offshore wind farms worldwide, is expected to rise significantly. By 2030, the global offshore wind project operations and maintenance activities are projected to require between 150 and 250 SOVs (James Fisher Renewables, 2023). In 2023, the supply of construction service operation vessels, SOVs, and newbuild vessels was estimated at 55, with most either committed to long-term charters (over 10 years) for existing wind farms or under construction with contracts already signed. The North Sea remains the largest market for SOVs; as of October 2022, the North Sea had 31 SOVs, compared to 2 in China/East Asia and 1 in Southeast Asia/Australia. Offshore wind continues to dominate the SOV market, with a utilization rate of 60.4% in October 2022, compared to 16.7% in the oil and gas sector.

Given the vast size of offshore wind farms, typically consisting of hundreds of turbines spread across expansive offshore areas, a large number of OSVs is required. This logistical complexity necessitates a substantial fleet of OSVs to ensure that all turbines are efficiently and effectively maintained and operated. In the oil and gas industry, large dynamic positioning vessels are commonly used for routine inspections and maintenance. However, two key factors hinder the direct application of traditional oil and gas industry practices to offshore wind farm O&M. First, the supply of large, heavy-duty OSVs typically used in the oil and gas sector is limited, making it challenging to deploy a sufficient number of these vessels for wind farm operations. Second, using such large vessels incurs significant costs and generates substantial GHG emissions, which are increasingly scrutinized as part of global efforts to reduce carbon footprints. In light of these constraints, there is a growing need for cost-effective, smaller OSVs specifically designed to meet the unique O&M requirements of offshore wind farms. These vessels must efficiently carry out routine maintenance tasks while minimizing operational costs and environmental impacts, particularly given the increasing number of offshore wind farms being developed globally.

When it comes to the routine inspection and maintenance of wind farm subsea facilities, which includes potential issues like scouring, corrosion, welding, and structural integrity, most operators rely on vessel and ROV based inspection methods (Figure 1.4). The ROV system is a crucial piece of equipment for unmanned diving. Due to its outstanding features such as safety, economy, efficiency, and large operational depth, it has gained increasingly widespread application worldwide.

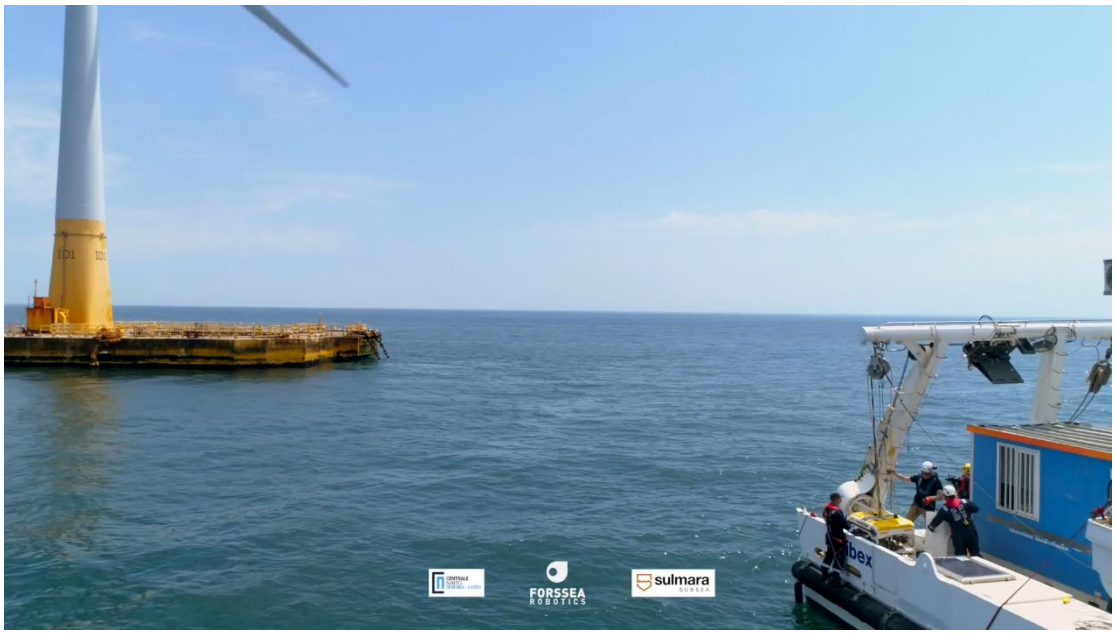


Figure 1.4 Argos ROV underwater survey – visual inspection of mooring lines and dynamic umbilical system integrity for floating wind turbine FLOATGEN (Offshore magazine, 2019).

The ROV system consists of four main parts: the ROV itself, TMS, umbilical cable, and tether. A ROV is a remotely operated underwater robot, primarily used for engineering, detection, and scientific research tasks (Figure 1.5). It is a camera mounted in a waterproof enclosure, equipped with thrusters for maneuvering, and connected to the surface by a cable through which video signals and telemetry are transmitted (Christ and Wernli, Sr., 2014). The movement of these robots can be controlled by autonomous logic or by a remote operator, depending on the robot's functionality and the operator's input level. The power source for robots can vary. It can be onboard (powered by batteries or engines), external (powered through conductors inside the tether), or a

combination of both (for example, powered by onboard batteries and remotely charged through the tether). The function of the TMS is to manage the tether handling system and launch the ROV when it reaches the target depth. In addition, the weight of the TMS is used to overcome the linear drag load imposed on the umbilical, thereby reducing the workload of the ROV. This allows more of the ROV's thrust capability to be reserved for specified tasks, rather than balancing ocean current loads. The shape of the TMS can be a simple winch system, acting as a top hat on the ROV, or it can be integrated into a cage to protect the ROV during launch and recovery in wave zone. The umbilical cable is a cable composed of conductors for power supply and optical fibers or hydraulic hoses for signal transmission. They are covered by a synthetic sheath and are used to connect the TMS to the floating facility, usually at the free water surface. The umbilical cable is then armored with steel wire or synthetic armor as its primary strength component. The tether connects the ROV to the TMS. Compared to the umbilical cable, the secondary cable or tether has no armor, so it can maintain neutral buoyancy and cause less interference to the stability and maneuverability of the ROV.

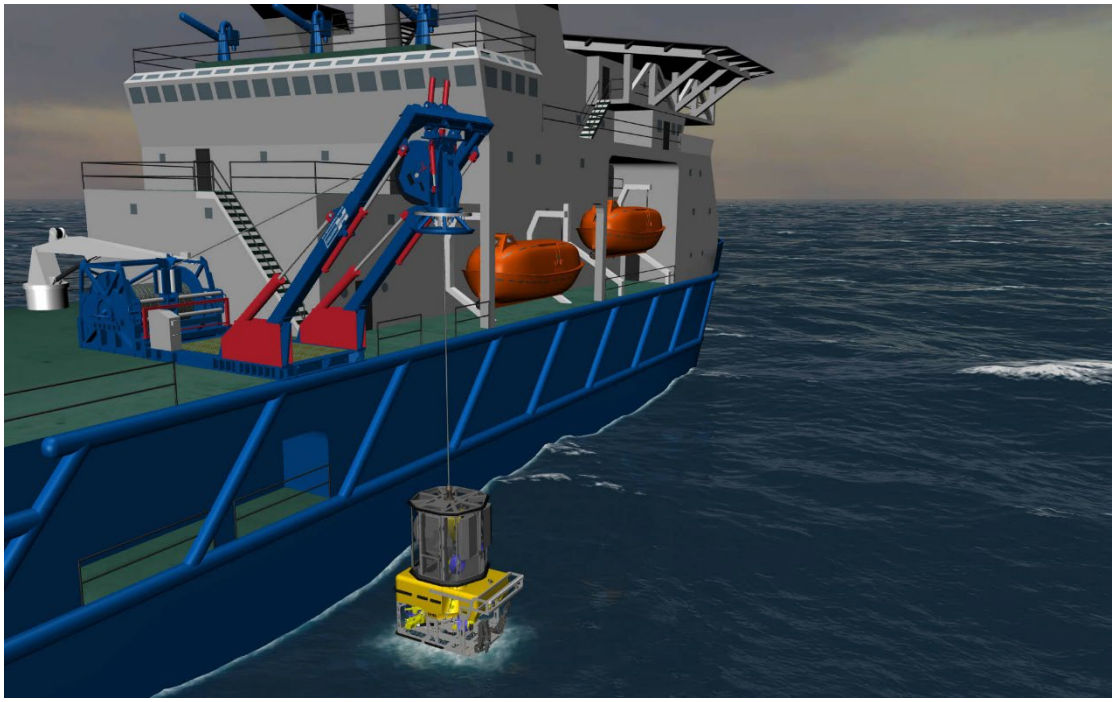

Figure 1.5 Launch and recovery system with the ROV (GRi Simulations Inc., 2018).

The launch and recovery process of an ROV is essentially a lifting operation with special emphasis on navigation in wave zones. The work procedure of ROV deployment can be divided into five stages in this study.

(1) Preparation stage (lift off phase): The service vessel arrives at the designated location and prepares to start operations. This stage includes the inspection of the ROV system to ensure that all equipment is in good condition. Then, the ROV system is lifted from vessel deck to its initial position in the air by a winch crane. This initial position is usually on the side or stern of service vessel for easy deployment of ROV.

(2) Launch stage (lowering or descending stage): The umbilical cable is continuously released from the winch on service ship, and the ROV descends from initial position through wave zone to the target and working depth. In this stage, the ROV needs to pass through the water surface and wave zone on, which is a relatively dangerous stage because the waves may cause impact on ROV.

(3) Operation stage: The ROV is deployed from the TMS and performs its designated tasks at the target depth. This stage is the main work stage of the ROV, where the ROV will perform various tasks such as inspection, repair and sampling. After the task is completed, the ROV is retracted back to the TMS by pulling back the tether. The length of this stage depends on the complexity of task and the battery life of ROV.

(4) Recovery stage (lifting or ascending stage): The umbilical cable is continuously pulled back by the winch crane on service ship, and the ROV rises from the water to the initial position and is finally recovered to the ship. In this stage, the ROV also needs to pass through the wave zone and the water surface, may cause impact on the ROV.

(5) Maintenance stage: This is the last stage of ROV deployment, including the inspection and maintenance of the ROV to ensure that it can work normally in the next deployment. This stage also includes data analysis and report writing on the tasks performed by the ROV.

The launch stage is divided into four load cases. The recovery stage has the same phases as the launch stage but follows an opposite process, so the description of recovery stage is omitted.

(1) ROV is in air. In this case, the ROV is initially stationary in the air. When the winch crane is activated, the ROV is lowered and the load component acting on the ROV is the inertial force due to the heave acceleration of the crane tip. In this case, there are no hydrodynamic forces acting on ROV, see Figure 1.6(a).

(2) ROV penetrates the water surface. The lower part of ROV is subjected to wave impact, resulting in slamming loads on the system. The dynamic forces are primarily due to two components: the slamming impact force on the bottom of ROV and the inertia force from the heave acceleration of vessel. The slamming impact is governed by the relative velocity between the ROV and water particles, see Figure 1.6(b).

(3) ROV is partly submerged. In this case, the load components consist of drag force, mass force, and inertia force. The mass force is composed of contributions from the hydrodynamic mass and the acceleration of water particles at the submerged part of ROV. The forces induced by wave particle velocity and acceleration are linked to the ROV's vertical center of gravity. The varying buoyancy force is dependent on the submerged volume, see Figure 1.6(c).

(4) The ROV is fully submerged. In this case, the main load components acting on the ROV include drag force, mass force, inertia force, and buoyancy force. The drag force primarily results from the relative motion between the ROV and the surrounding water, with the vertical water particle acceleration and velocity being related to the ROV's center of gravity. The vertical drag force is determined by the ROV's projected area and drag coefficient. The mass force is caused by the acceleration of water particles, induced by waves or fluid motion, and depends on the water acceleration and the submerged volume of the ROV. The inertia force arises from the ROV system's acceleration in the water, proportional to the mass and acceleration of the ROV. Buoyancy is the upward force exerted by the water on the ROV, which is typically related to the submerged volume and the density of the water, counteracting part of the ROV's weight, see Figure 1.6(d).

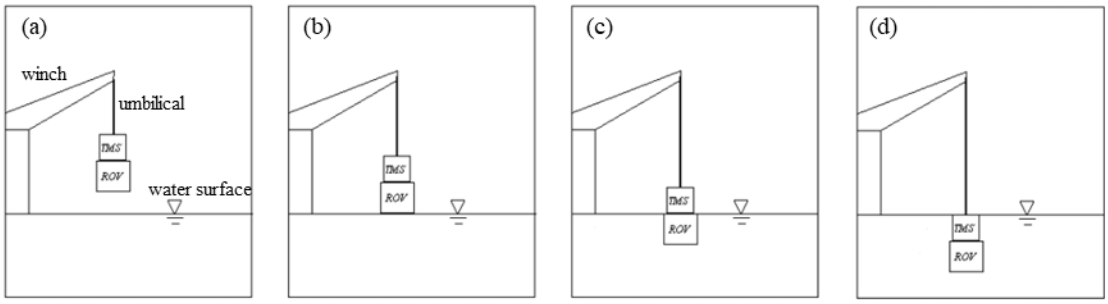


Figure 1.6 Load cases during launch stage (Valen, 2010).

## 1.3 Literature review: lifting operation of subsea module

### 1.3.1 Current recommended practices

The launch and recovery process of an ROV is essentially a lifting operation with special emphasis on navigation in wave zones. The current recommended practices for lifting operation are primarily derived from the guidance provided by DNV (2017). The guidance offers a comprehensive approach and a simplified method to assess all phases of subsea lifting operations including lifting off from the deck, maneuvering from the vessel, lowering through the wave zone, descending to the seabed, and positioning and landing. The guidelines provided by classification societies are usually regarded as the primary reference, and as such, they are directly followed by operators and suppliers when conducting lifting and lowering operations. In numerical simulations of lifting operations, SIMO and OrcaFlex are frequently utilized. SIMO is a software tool commonly used for simulating the dynamic behavior of marine structures and offshore operations. OrcaFlex is a versatile software package widely used for dynamic analysis of offshore systems, including risers, mooring lines, and subsea cables. Several studies have critically analyzed and compared the earlier standards proposed by DNV. These studies often focus on evaluating the effectiveness, applicability, and comprehensiveness of the DNV guidelines in various operational contexts. The regulations governing offshore lifting operations are assessed by Thiagarajan and Yann (2001), particularly focusing on the calculation of crane wire tension and the dynamics of subsea modules during deployment. The authors identify several shortcomings in existing practices, such as the over-prediction of wire tension and underestimation of

underwater heave motion, which can lead to operational inefficiencies and safety risks. Through model tests and numerical simulations, the study highlights the need for revising regulations to better account for factors like added mass, wave-induced motion, and snap loads, thereby improving safety and operational effectiveness in offshore lifting procedures. Kimiaei et al. (2009) primarily compares a simplified numerical model with DNV guidelines for the installation of subsea platforms. The study focuses on evaluating hydrodynamic loads, dynamic amplification factors, and potential snap forces during lifting operations using numerical simulations and DNV guidelines. The results indicate that the DNV 1996 guidelines generally overestimate these loads and factors, while the DNV 2008 guidelines are more accurate but still conservative compared to the numerical model. Overall, the numerical model provides more precise results, which can better optimize the design and safety of subsea installation operations. Valen (2010) examines the operational limits for launching and recovering ROV through splash zone under various sea conditions, a critical phase in offshore operations. The research compares the hydrodynamic forces calculated using DNV Recommended Practices with those obtained from time domain simulations in the SIMO program. The findings reveal that DNV guidelines tend to overestimate hydrodynamic forces, leading to unnecessarily restrictive operational limits. In contrast, the SIMO analysis supports the current operational limit of 4.5 m significant wave height for DOF Subsea's ROV system, with caution advised for potential slack umbilical occurrences, which are dependent on vessel heading and weather conditions. Bjerkholt (2014) critically examines the conservative nature of the Simplified Method proposed by DNV standards for estimating hydrodynamic loads during subsea ROV operations, particularly in the splash zone. His study compares this method with time domain simulation programs, SIMO and OrcaFlex, highlighting significant discrepancies between the analytical approach and simulation results. The research demonstrates that while the Simplified Method suggests an overly restrictive operational wave height, the time domain simulations indicate that higher Hs values can be safely managed, especially when wave period is also considered. Bjerkholt (2014) concludes that time domain simulations offer a more realistic and less conservative alternative for determining operational limits in subsea operations. Jenssen (2015) evaluates the weather criterion for launching and recovering a work class ROV from the semi-submersible rig Snorre B, which is currently set at four meters significant wave height based on simplified DNV calculations. Jenssen's work involves a more detailed domain analysis using SIMO and

motion measurements of the ROV to assess the validity of the existing criteria and identify critical factors influencing the operation. His findings highlight that snap load in the umbilical, caused by slack due to drag force from vertical water particle velocity, are a significant concern during launch, while the recovery phase and pontoon impact risk are less critical. The study suggests that an effective heave suspension system may mitigate these forces, though uncertainties in system simplifications and input parameters complicate a definitive assessment of its impact.

### 1.3.2 Lifting operation of subsea module

When a submerged module passes through the wave splash zone, it represents a critical phase where the structure is most susceptible to waving forces and interactions with the free surface. Extensive research on subsea lifting operations has been reported, covering numerous experimental contributions over the past decades. Faltinsen et al. (2004) provides an in-depth analysis of slamming phenomena in marine applications, particularly focusing on the effects on ships and offshore structures. The authors discuss various types of slamming, such as bottom, bow-flare, bow-stem, and wet deck slamming, which occur under different conditions like ship motions and wave interactions. The study emphasizes the importance of integrating slamming within the broader context of structural dynamics and global flow analysis around the ship or structure. It highlights the need for a comprehensive understanding of two-phase flows, especially in scenarios involving shallow-draft vessels like very large floating structures. The problem of wave impact as an object descends through the splash zone is highly complex and has been investigated by numerous researchers using various approaches. In addition to the common categories of numerical simulations and experimental studies, research can also be grouped based on the modeling approach used. These studies range from partial analyses of water entry in calm conditions or wave impacts on fixed objects to comprehensive investigations considering various entry speeds in disturbed free surfaces. Yettou et al. (2006) conducted an experimental study to analyze the pressure distribution on a symmetrical wedge during water impact. The research aimed to understand the relationship between various parameters, such as drop height, wedge angle, and wedge mass, and the resulting pressures on the wedge as it enters the water. The study is particularly relevant to the design and safety of recreational boats that experience repeated wave impacts, causing significant pressure

on their hulls. The study's findings showed that while the mass and drop height of the wedge had minimal impact on the pressure coefficient, the wedge angle significantly influenced it. Additionally, the proposed method provided a more accurate estimation of peak pressure by accounting for the variation in wedge velocity during the water entry process. An experimental study to investigate the impact of a free-falling wedge with water was carried out by Lewis et al. (2010), focusing on synchronized visualization, pressure, and acceleration measurements. The study was motivated by the need for high-quality experimental data to validate computational fluid dynamics (CFD) simulations and theoretical models related to marine planning craft, which encounter complex hydrodynamic phenomena during water re-entry. A significant finding of the study was the identification of a time delay of approximately 2.5 milliseconds between the visual observation of the wedge's impact and the onset of measurable deceleration. This delay highlights the challenges in accurately capturing the moment of impact and emphasizes the need for synchronized data acquisition in such experiments. Using a two-phase incompressible-compressible Smoothed Particle Hydrodynamics (SPH) method, Lind et al. (2015) predicted the impact pressures during water-air wave slamming. The research focused on the impact of a rigid horizontal plate on wave crests and flat-water surfaces. The study demonstrated that air plays a significant role in cushioning the impact, especially when the plate hits flat water surfaces, resulting in lower impact pressures. The SPH method showed good agreement with experimental results, particularly in predicting the pressure peaks during impact. The study concluded that while the SPH method is effective for modeling the complex dynamics of wave slamming, further improvements are needed to enhance the accuracy of predictions, particularly in cases involving flat surface impacts. The research provides valuable insights into the role of air in reducing impact pressures and offers a basis for future developments in numerical modeling of such phenomena. Zan et al. (2021) investigates the dynamics of a suspended subsea module at various positions in the splash zone during lifting operations. Through experimental tests conducted in a wave tank, the study examines how the module's position relative to the water surface influences the dynamic loads and motions it experiences, particularly under the impact of irregular waves. The results indicate that the highest dynamic loads occur when the module is in a semi-submerged state, with the forces being asymmetric due to the interaction between the perforated plates of the module and the water surface. This asymmetry leads to significant variations in the relative force and motion parameters,

particularly in pitch and roll angles. The study emphasizes the importance of accurately predicting these forces, as they have critical implications for the safety and effectiveness of subsea module installations. A detailed analysis of the process of lowering suction piles through splash zone is carried out by Gordon et al. (2013), focusing on the challenges posed by hydrodynamic forces, vessel motions, and the risk of snap loading. The authors utilize time-domain simulations to model the dynamic behavior of the crane, wire, and pile system, addressing key factors such as wave impacts, drag, and buoyancy. The paper compares this comprehensive simulation approach with other industry models, highlighting the importance of accurately predicting operational limits to ensure the safety and efficiency of offshore lifting operations. Chen et al. (2017) conducted a detailed study on the simulation and motion analysis of deepwater manifold lifting, which is crucial for offshore oil and gas field development. The study focused on the lifting installation method used to install subsea manifolds, particularly in the challenging environment of the Liwan 3-1 Gasfield in the South China Sea. The authors first selected appropriate environmental parameters, including wind and wave spectra, and then analyzed the motion response of the entire lifting system, which includes the vessel, cable, and manifold. Their simulation in the time domain considered the effects of wind, waves, and current on the system throughout different stages of the installation process—namely, the entering, steady lowering, and landing phases. The results demonstrated that the highest motion responses occurred in the direction of the environmental load, and the cable tension peaked during the entering phase. Nam et al. (2017) explored the coupled motion responses of a floating crane vessel and a lifted subsea manifold during deep-water installations using both experiments and numerical simulations. The study found that the vessel's roll motion is significantly influenced by the interaction with the lifted object through the hoisting wire. Heave motion peaks in the subsea manifold were linked to crane-tip motion and vertical resonance. The use of a passive heave compensator effectively reduced dynamic tension in the hoisting wire, particularly in shorter wave periods. Zhang et al. (2017) introduced a sophisticated mathematical model integrated into a virtual reality simulation system designed to improve the training and operational efficiency of deepwater installation processes. By simulating the multi-body interactions between vessels, cranes, and subsea equipment under challenging environmental conditions, their study demonstrated the system's high accuracy and applicability for reducing operational risks in deepwater settings. Li et al.

(2020) analyzes the challenges associated with lowering large subsea spool pieces through the splash zone during offshore lifting operations. The study emphasizes the importance of accurate numerical modeling to predict dynamic responses and assess operational limits under varying sea states. The authors use time-domain simulations to explore the impact of wave direction, shielding effects from the vessel, and wave spreading on the spool's behavior. The findings underscore the necessity of considering these factors in planning to ensure safe and efficient operations, particularly in environments like the Barents Sea.

### 1.3.3 Coupled analysis in ROV deployment

The nonlinear relationship between waves and wire tension is difficult to accurately model through simple mathematical formulas because of the wave impacts act on both ROV and ship simultaneously. Numerical simulation and experimental methods are currently used as the primary means of researching lifting operation. Driscoll et al. (2000) develops and validates a one-dimensional finite-element lumped-mass model for a vertically tethered deep-sea ROV system, focusing on its dynamic behaviour under surface excitation. The model successfully predicts key aspects of system behaviour, including cage motion, tether tension, and natural frequencies. The study emphasizes the importance of accurately modelling hydrodynamic forces, particularly during snap loads, to improve the reliability and safety of offshore operations involving tethered marine systems. The inclusion of a wake model significantly enhanced the accuracy of the predictions. A numerical scheme to evaluate the effects of a communication cable on the dynamics of an underwater flight vehicle is proposed by Feng and Allen (2004). The study demonstrates how the cable, typically used for transmitting data and commands between the vehicle and a control station, introduces significant drag and affects the vehicle's motion, particularly during manoeuvres such as diving and turning. By incorporating the cable's dynamics into the vehicle's control system, the model helps in developing a more effective autopilot system that compensates for these effects, ensuring better operational performance. The phenomenon of snap loading in synthetic ropes, which occurs when a slack rope suddenly becomes taut and leads to large dynamic forces that can potentially damage the rope or connected masses, is investigated by Hennessey et al. (2004). Through a series of drop tests, the research examines the effects of different rope materials, drop heights, weights, and precycling

on the magnitude of snap loads. The findings reveal that ropes with looser braiding exhibit greater elongation and energy dissipation under dynamic loading, while precycled ropes demonstrate increased stiffness and reduced energy absorption over successive tests. A mathematical model is proposed to predict the snap load as a function of displacement and velocity, providing a useful tool for analysing the dynamic behaviour of ropes in various engineering applications, including mooring and towing operations. Sayer (2008) investigates the hydrodynamic loads experienced during the deployment of ROV, with a focus on the accuracy of current prediction methods used in industry guidelines. The research demonstrates that conventional methods, particularly those using Morison's equation with standard coefficients, may overestimate the hydrodynamic forces, leading to overly conservative operational limits. The study proposes the use of total (substantive) acceleration instead of local acceleration in force calculations, which improves the accuracy of predictions even in steep wave conditions. The findings emphasize that ROVs near the surface experience significant upward forces, potentially causing slack in the tether, which has implications for operational safety during launch and recovery phases. Hsu et al. (2017) explore the extreme mooring tensions experienced by FOWT due to snap loads, which occur when a mooring line temporarily goes slack and then re-engages with a sudden increase in tension. The research includes experimental tests under 100-year storm conditions, demonstrating that snap loads can significantly exceed typical dynamic tension levels, posing risks to the structural integrity of FOWT. The study proposes a composite Weibull probability distribution model to better predict the extreme tensions in mooring lines, highlighting the need for more robust design practices to account for the impact of snap events. Based on stability theory and nonlinear time-domain simulation methods, Huo et al. (2018) investigate the fishtailing oscillations of a single point moored vessel in shallow waters. The research analyzes the effects of environmental forces such as wind, waves, and current on the dynamic stability of the Single Point Mooring (SPM) system, highlighting the significant impact of these forces on mooring tension and vessel motion. The study provides a comprehensive approach to predicting the occurrence of fishtailing oscillations, offering valuable insights for the design and emergency response planning of mooring systems in shallow water environments. Asmara et al. (2020) conducts a safety analysis of the mooring hawser between a floating storage offloading unit and an SPM buoy under irregular wave conditions. Using motion simulations in both the frequency and time domains, the research

compares the performance of different hawser line lengths (45 m and 70 m) over 1-year and 100-year wave periods. The results show that a longer hawser line significantly reduces tension and improves the safety factor, minimizing the risk of mooring failure during extreme weather conditions. The study emphasizes the importance of optimizing hawser length to enhance the durability and safety of offshore mooring systems. Lubis and Kimiaei (2021) focused on the measurement and prediction of umbilical tension during the launch and recovery of an ultra-deep-water ROV through splash zone. The ship motion was simplified to simple harmonic motion in tests and regular waves were used for environmental simulation. Through experiments and numerical simulations, it was found that the recovery process generally experiences higher tension than the launch process, and the study also explored the impact of winch speed and ship motion on tension control, providing guidance for safe operations. Lubis et al. (2021) examined methods to reduce tension in the umbilical of work-class ROVs to enable operations in ultra-deep waters, beyond the typical 3 km depth limit. They investigate three configurations—hook, hook & top floaters, and mid-depth hook—compared to the conventional free-flying ROV setup. Simulations under extreme conditions demonstrate that the hook configuration effectively reduces tension and the risk of snap loads for 3 km operations. For 6 km depths, the mid-depth hook configuration is preferred due to its broader operational window, although it increases ROV offset. A detailed hydrodynamic analysis of the launch and recovery process for a ROV from an autonomous surface vessel (ASV) is presented by Zhao et al. (2021). The study explores the dynamic interactions between the ASV, ROV, and the umbilical cable, using both time-domain and frequency-domain models to simulate real-world conditions. The research highlights the challenges of maintaining system stability under varying environmental conditions, particularly focusing on the impact of tidal currents and wave forces. The results demonstrate that the control strategies for the winch and umbilical system are critical for minimizing tension and ensuring safe operations, especially during launch and recovery phases. Ju et al. (2023) provides a comprehensive numerical analysis of the dynamic behavior of a catenary anchor leg mooring system, focusing on the fishtailing motion, buoy kissing, and the effectiveness of pullback force in maintaining stability. The research demonstrates that fishtailing, characterized by large yaw motions, can lead to significant mooring forces and risks of buoy kissing (collision between the tanker and buoy). The application of an 800 kN pullback force significantly reduces these risks, ensuring safer and more stable mooring operations.

The study underscores the importance of having a tug on standby to mitigate the effects of environmental forces on the mooring system. Tran et al. (2023) investigates the operability of control systems for the launch and recovery of ROV from small ASV. The study utilizes numerical simulations to evaluate the impact of various control algorithms, including wave-compensating dynamic positioning and active heave compensation, on the stability and operability of the ROV and ASV system. The research highlights the critical importance of optimizing control parameters to enhance operability limits under different sea states, with a particular focus on minimizing the risk of slack in the umbilical and ensuring safe docking procedures. The findings underscore the need for integrated control system designs that account for both the hydrodynamic interactions and the dynamic responses of the entire system during complex marine operations.

The literature review indicates that the motion of the support vessel directly affects the movement of the crane tip, which in turn excites the top of the cable. There are two common approaches to represent this process:

(1) Utilizing the vessel's response amplitude operator (RAO) and the crane tip position to calculate the vertical motion: By combining the RAO with the geometric position of the crane tip, it is possible to accurately determine the vertical displacement of the crane tip under various sea conditions. This method accounts for the frequency characteristics and nonlinear factors of the vessel's motion, thereby providing a more precise simulation of the dynamic behavior encountered during actual operations.

(2) Applying a sinusoidal motion directly at the top of cable (crane tip): This approach simplifies the calculation process by imposing a sinusoidal motion with a known frequency and amplitude on the cable top. The sinusoidal motion represents the influence of the vessel's motion on the cable top, particularly in idealized scenarios where it can effectively simulate the vessel's behavior under regular wave conditions.

The following key points can be identified as consolidated characteristics of the phenomenon related to lifting operations and ROV deployment:

-(1) Transient nature of the problem: The ROV deployment operation is characterized by a highly transient phase, with rapid changes in cable tension and dynamic conditions throughout the process. Sudden increases in tension can cause damage to the cable. To address this issue, numerical simulations are employed to capture these rapid changes in cable tension, particularly at the start and end of the crane phase. Furthermore, a set of improvement measures, including optimized crane control strategies, are proposed to reduce the risk of cable damage. The solution and detailed measures are discussed in Chapter 5.

(2) Incorporation of vessel movements in calculations: The vessel's movements must be accounted for in the calculations. Typically, the rigid body motion of the vessel is computed using radiation-diffraction methods, and the resulting motions at the crane tip are considered in the analysis. Time-domain simulations that account for vessel movement can be utilized to accurately model crane tip motions and their effects. This is detailed in Section 2.5.

(3) Assumption of rigid hoisting cable: During this phase, the hoisting cable is usually assumed to be rigid due to its relatively short length. Consequently, the motions at the top of the sling are assumed to mirror those at the crane tip. This solution is presented in Section 2.5.

(4) Critical role of lowering velocity: The velocity at which the object is lowered through the splash zone is a critical parameter. High lowering velocities can result in intense and undesirable slamming loads, while low velocities increase the duration of exposure to wave actions, slamming events, and water exit phenomena, thereby extending the time during which the module is vulnerable to these forces. Parametric studies can be conducted to determine optimal lowering velocities that minimize slamming loads while reducing exposure to wave actions. Variable speed control systems can be implemented to adapt the lowering velocity based on real-time wave conditions. This is covered in Section 5.2.

## 1.4 ROV deployment under single point mooring system

During routine inspection and maintenance of subsea facilities, which include assessing potential scour around foundations, corrosion, welding, and structural integrity, operators typically rely on vessel and ROV-based inspection methods as an integral part of field O&M. Large dynamic positioning vessels are commonly used to deploy ROVs in the oil and gas industry. However, the lack of suitable large offshore service vessels to perform regular inspections and maintenance of offshore wind farms is an obvious bottleneck with the rapid development of global offshore wind energy. Driven by the ongoing efforts of the offshore renewable energy industry to reduce the levelized cost, the motivation for deploying ROVs using smaller vessels based on the single point mooring system (SPMS) approach is evident (Nuernberg et al., 2021). The single point mooring system is originally developed to provide secure mooring for large oil tankers to facilitate the high-volume loading and unloading of petroleum products (Amaechi et al., 2021). It allows large ships restricted from ports to transfer cargo outside port limits or in sheltered anchorages. The vessel is affixed to the mooring buoy using a single line or chain, allowing it to pivot with wind and sea conditions while maintaining a constant position. A tug vessel is often positioned at the cargo vessel's stern to maintain distance from the buoy, as shown in Figure 1.7.

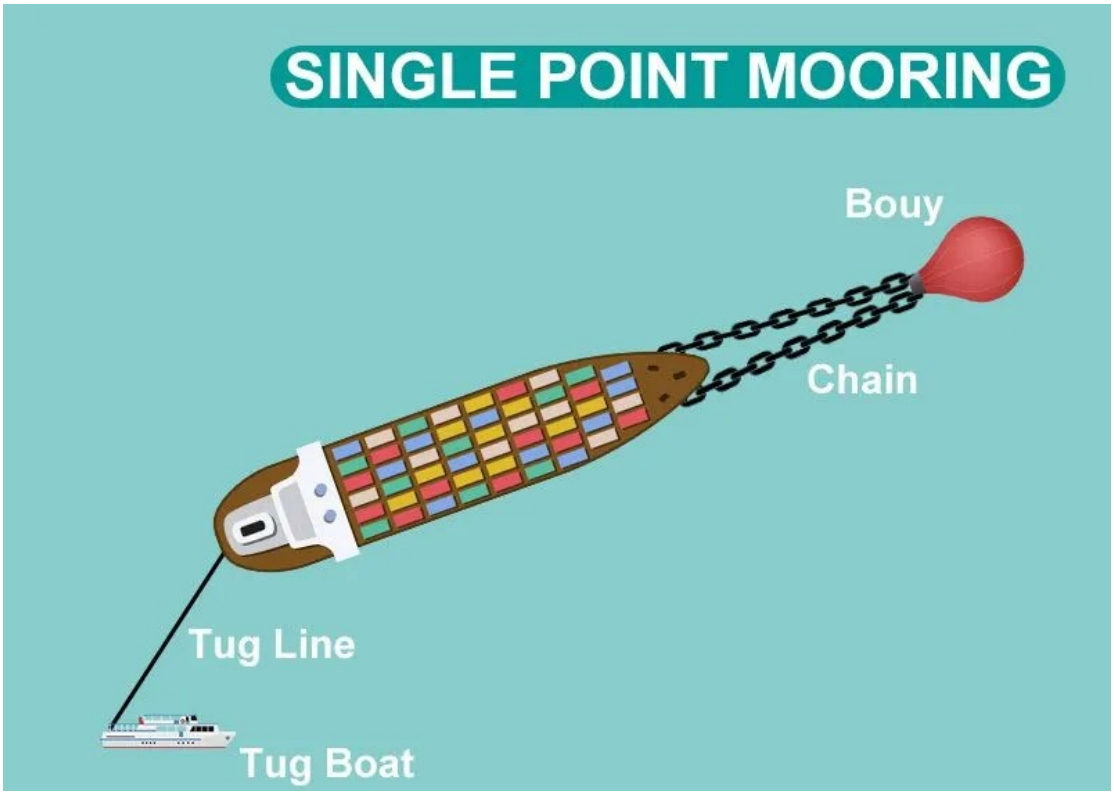


Figure 1.7 The schematic of single point mooring system (OUCO Group, 2024).

In the offshore wind industry, small vessels without dynamic positioning systems are used to deploy ROVs. The small vessels do not require tug assistance because they offer greater maneuverability and flexibility, allowing them to independently carry out tasks such as docking and adjusting courses. For wind turbines that cannot be directly connected, the small vessel establishes a connection by wrapping a line around the tower. Specifically, one end of the line, attached to a buoy, is placed on the water surface. The vessel then carries the other end of the line completing a full circle around the wind turbine, before connecting it back to the line's initial end. The smaller vessel achieves a stable position by connecting to the wind turbine foundation via mooring lines to limit its movement in wind, waves, swells and currents. The ROV is then deployed on the ship stern or side to conduct subsea inspections from a distance of approximately 30 - 45 m, as shown in Figure 1.8. Larger ships do not significantly increase operating times even though they offer higher payload and stability in harsher environmental conditions. Moreover, the daily cost of a small ship is about one-tenth to one-fifth of the cost of large machinery required by a large ship. Another advantage of using smaller OSVs is

the significant reduction in greenhouse gas emissions compared to the larger vessels used by conventional offshore O&G industry.

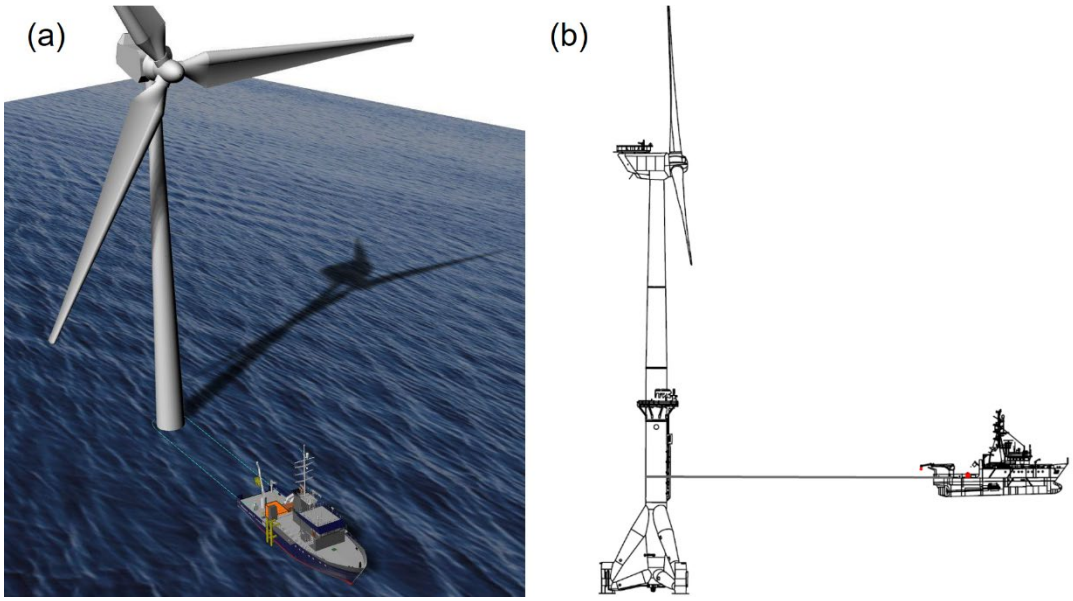


Figure 1.8 3D Model (a) and 2D Schematic (b) of ROV deployment in smaller vessel using SPMS method (Nuernberg et al., 2021).

The ROV passes through wave zone from the initial position in the air and then reaches its working position in the water through the gradual extension of wire during the launch phase. During the recovery phase, the wire is gradually retracted to lift the ROV from underwater to the original position after it has completed assigned tasks. Interactions between the ROV, ocean waves, and the support vessel can cause the wire to suddenly change from internal slack to taut state, significantly amplifying the tension experienced. Such occurrence, commonly referred to as snap load or sudden loading, may exceed the specified safe working load or allowable strain leading to component damage (Lubis and Kimiaei, 2021). In contrast to large OSV operating in offshore O&G development, interaction between a small OSV and ROV in the field of combined wave and current sea-state can be significantly more complex. Therefore, a comprehensive analysis of ROV deployment procedures should be performed to determine the operational limits, taking into account nonlinear interactions between the ROV, wire, vessel, and wave dynamics.

The SPMS method applied to ROV deployment onboard a small OSV for offshore wind farm O&M requires establishing a connection between offshore support vessel and offshore wind turbine via connecting wire lines. The motion response of support vessel may further compromise the stability and safety of mooring system of floating wind turbine during routine inspections and maintenance operations. Furthermore, the deployment of ROV from support vessel introduces additional complexities. The ascent and descent of ROV are controlled through the umbilical cable connected to a winch crane on service vessel. This process involves the snap load of umbilical cable as the ROV traverses wave zone due to interactions among waves, support vessel, and floating wind turbine. Sudden loading occurs when a cable transitions abruptly from a slack to a taut state, amplifying tension and potentially exceeding safe operating thresholds. Additionally, there is a potential impact on connecting lines and mooring lines as the ROV traverses the wave zone. This rapid increase in line tension underscores the complex challenges and risks associated with SPMS operations.

### 1.5 Research aims and objectives

This study develops a coupled numerical model that integrates a floating wind turbine, a small service vessel, and a work class ROV to predict the dynamic tension in umbilical cable and winch wire during the launch and recovery procedure when passing through wave zone. The model also evaluates the interactions and impacts between the SPMS method, ROV deployment, and the FOWT mooring system. Realistic operating sea conditions are simulated using weather forecast data on waves, swells, winds, and currents from the DanTysk wind farm in the North Sea. The developed model is validated through experimental tests on a 1:10 scaled model in a wave flume under calm water and regular waves, as well as through full-scale tension data of connecting lines obtained by operators at sea. The following objectives are set to achieve the project aims:

1. To develop a coupled numerical model incorporating a fixed or floating offshore wind turbine, a small service vessel, and an ROV operating onboard OSV to evaluate the interactions and impacts among SPMS method, ROV deployment, and the mooring system of FOWT.

2. To study the effects of various combinations of key factors including winch speed, waves, ship motion and deployment positions on the magnitude of snap load in detail.

3. To determine the environmental limit for safe operation of the work class ROV on board a small OSV based on comprehensive parametric analysis, a new multi-parameter criterion is proposed.

4. To explore potential methods expanding the limit for safe operation of ROV deployment onboard a small OSV.

5. To determine a safe operational window for the work class ROV deployed from the small vessel when navigating wave zone during launch and recovery procedure, provide a practical operational recommendation onboard the small OSV.

6. To determine the environmental limit and key influencing factors for inspection operations by examining the tension relationships among umbilical cable, connecting lines, and mooring lines.

Through this comprehensive evaluation, the study seeks to establish the feasibility and effectiveness of the proposed approach in ensuring the robustness and reliability of offshore wind energy O&M operations.

## 1.6 Thesis organization

This thesis is organized into seven chapters. Chapter 1 provides a brief introduction to the ROV system for operation and maintenance of offshore wind farm and includes a comprehensive literature review of related studies. Chapter 2 details the development and implementation of numerical models, including experimental tests, numerical model validation and detailed results and discussions about dynamic tensions in winch wire. Chapter 3 presents the dynamic analysis of launching and recovering an ROV from a small offshore support vessel. Chapter 4 discusses the interaction between an offshore wind turbine and offshore support vessel. Chapter 5 demonstrates the operational capabilities of small OSVs for a fixed wind turbine. Chapter 6 explores the

deployment of an ROV onboard a small OSV in conjunction with a floating wind turbine. Finally, Chapter 7 concludes the study and discusses potential directions for future research.

# 2 Model development and validation

## 2.1 Numerical methodology – potential flow theory

### 2.1.1 Frequency domain analysis

In the present study, the fluid is assumed inviscid, irrotational and incompressible. The total velocity potential $\Phi(x, y, z, t)$ satisfies the Laplace equation and different boundary conditions. The boundary value problems will be solved in the following part in first order to investigate the hydrodynamic characteristics of multi-body system.

With the assumption of a perturbation solution in terms of a small wave slope of the incident waves, the velocity potential is expanded in a form (HydroD theory manual, 2021):

$$\Phi(x, y, z, t) = \Phi^{(1)}(x, y, z, t) + \Phi^{(2)}(x, y, z, t) + \cdots \quad (2.1)$$

According to the perturbation of the total velocity potential, the first order boundary value problem is considered separately. Additionally, the nonlinear incremental equation of motion is applied in the time domain coupled analysis making the stiffness on each platform update at each time step.

The total first-order velocity potential $\Phi^{(1)}(x, y, z, t)$ for the wave-body interaction can be expressed by a sum of components having circular frequency $\omega$:

$$\begin{aligned} \Phi^{(1)}(x, y, z, t) &= Re\left\{\phi^{(1)}(x, y, z)e^{-i\omega t}\right\} \\ &= Re\left\{\left[\phi_I^{(1)} + \phi_D^{(1)} + \phi_R^{(1)}\right]e^{-i\omega t}\right\} \end{aligned} \quad (2.2)$$

Here the $\phi^{(1)}(x, y, z, t)$ is the complex first-order velocity potential which is independent of time. The subscript $m = 1,2, \ldots,6$ represents the six degrees of freedom of motion (surge, sway, heave, roll, pitch and yaw respectively). The $N = 1,2, \ldots N_i \ldots N_j \ldots N$ is the number of the platforms in multi-body system. The

$\phi^{(1)}(x, y, z, t)$ can be decomposed to the sum of incident wave potential $\phi_I^{(1)}$, diffraction potential $\phi_D^{(1)}$, and radiation potential $\phi_R^{(1)}$.

The first-order incident wave spatial potential $\phi_I^{(1)}$ can be expressed as:

$$\phi_I^{(1)} = \frac{-igA}{\omega} \frac{\cosh k(z+h)}{\cosh kh} e^{ikx} \tag{2.3}$$

The radiation potential $\phi_R^{(1)}$ is a linear combination of the modes of motion components that:

$$\phi_R^{(1)} = -i\omega \sum_{m=1}^{6} \sum_{N_i=1}^{N_i=N} \left( \xi_m^{(1)N_i} \phi_m^{(1)N_i} \right) \tag{2.4}$$

where $N_i$ is the $i$-th body in multi-body platform system with total number of bodies $N$. $\xi_m^{(1)N_i}$ is the first-order complex amplitude of the oscillatory motion in mode of the $i$-th body of multibody body platform system in $m$-th degrees of freedom. $\Phi_m^{(1)N_i}$ is the first-order unit-amplitude radiation potential (specifically, unit amplitude means the unit-amplitude linear or angular velocity of the rigid body motion). These modes are referred to as surge, sway, heave, roll, pitch and yaw in the increasing order of "$m$". The $N_i = 1,2, \ldots, N$ is the order of the platform of each body in multibody system.

### 2.1.2 Dynamic time domain analysis

A time-domain coupled analysis was performed to solve the motion equations of a multi-platform system with full 6 degrees of freedom, taking into account the fully coupled interactions between the platforms and the attached mooring lines and risers. The time-domain coupled analysis involves two main steps. The first step, known as static analysis, involves calculating the static equilibrium position of the system. This is done using the kinetic parameters—such as added mass, damping matrix, and hydrostatic matrix—obtained from a prior frequency-domain analysis. These parameters provide the necessary inputs for determining the system's equilibrium under static conditions. The second step, referred to as dynamic analysis, involves performing

a coupled dynamic simulation in the time domain. In this step, the equilibrium position calculated during the static analysis serves as the initial condition for the dynamic analysis. The dynamic analysis accounts for the time-varying effects and interactions between the platforms and mooring lines as the system responds to external forces.

In this approach, the effect of the mooring system is comprehensively considered. Each platform in the system is modeled as a rigid body component within a 3D finite element method framework. The mooring lines and risers are represented as slender structures using finite elements, with each being modeled as a line of interconnected elements. This full arrangement ensures that the interactions and couplings between the platforms and the mooring lines and risers are accurately captured, providing a realistic simulation of the system's behavior under various operating conditions. The dynamic equilibrium of a finite element model that has been spatially discretized can generally be represented as:

$$R^I(r, \ddot{r}, t) + R^D(r, \dot{r}, t) + R^S(r, t) = R^E(r, \dot{r}, t) \tag{2.5}$$

where $R^I$ is inertia force vector, $R^D$ is damping force vector, $R^S$ is internal structural reaction force vector, $R^E$ is external force vector, and $r, \dot{r}, t$ are structural displacement, velocity and acceleration vectors.

This system is characterized as a nonlinear system of differential equations due to several factors. The dependencies of inertia and damping forces on displacement introduce nonlinearity, as does the coupling between the external load vector and the system’s structural displacement and velocity. Additionally, the relationship between internal forces and displacements is inherently nonlinear, further complicating the system's behavior.

All force vectors within the system are established through the assembly of contributions from individual elements, along with specified discrete nodal forces. This assembly process integrates the various forces acting on the system into a cohesive model that accurately reflects the interactions between different components.

The external force vector incorporates several key factors:

Weight and buoyancy: The gravitational forces acting on the structure and the buoyant forces due to the displacement of fluid by the structure.

Forced displacements due to support vessel motions: Movements imposed on the structure by the motions of a supporting vessel, which can induce additional displacements and forces.

Drag and wave particle acceleration terms in the Morison equation: The effects of drag forces due to water flow and the acceleration of wave particles, which are significant in the Morison equation used for calculating the hydrodynamic forces on slender structures.

Specified discrete nodal point forces: Forces applied at specific nodal points in the finite element model, representing concentrated loads or other localized effects.

These components together define the external forces acting on the system, each contributing to the overall dynamic response of the structure. The complexity of this system requires careful consideration of both the nonlinear relationships and the interactions between various forces to accurately predict the system's behavior under different operating conditions.

The inertia force vector can be expressed as

$$R^I(r, \ddot{r}, t) = [M^S + M^F(r) + M^H(r)]\ddot{r} \tag{2.6}$$

where $M^S$ is structural mass matrix, $M^F(r)$ is mass matrix accounting for internal fluid flow, and $M^H(r)$ is displacement-dependent hydrodynamic mass matrix accounting for the structural acceleration terms in the Morison equation as added mass contributions in local directions.

The damping force vector is expressed as

$$R^D(r,\dot{r}) = [C^S(r) + C^H(r) + C^D(r,\dot{r})]\dot{r} \tag{2.7}$$

where $C^S(r)$ is internal structural damping matrix, $C^H(r)$ is hydrodynamic damping matrix accounting for diffraction effects for floating, partly submerged elements, and $C^D(r,\dot{r})$ is matrix of specified discrete dashpot dampers which may be displacement- (and velocity-) dependent.

The incremental form of the dynamic equilibrium equation, is obtained by considering dynamic equilibrium at two configurations a short time interval apart:

$$(R^I_{t+\Delta t} - R^I_t) + (R^D_{t+\Delta t} - R^D_t) + \left(R^S_{t+\Delta t} - R^S_t\right) = (R^E_{t+\Delta t} - R^E_t) \tag{2.8}$$

Equation states that the increment in external loading is balanced by increments in inertia-, damping- and structural reaction forces over the time interval.

For numerical solution, the nonlinear incremental equation of motion is linearized by introducing the tangential mass-, damping- and stiffness matrices at the start of the increment. The linearized incremental equation of motion can be expressed as:

$$M_t\Delta\ddot{r}_t + C_t\Delta\dot{r}_t + K_t\Delta r_t = \Delta R^E_t \tag{2.9}$$

where $M_t$, $C_t$ and $K_t$ denote the tangential mass-, damping- and stiffness matrices computed at time $t$. $\Delta r_t$, $\Delta\dot{r}_t$, $\Delta\ddot{r}_t$ and $\Delta R^E_t$ are the incremental displacement, velocity, acceleration and external force vectors, respectively.

To prevent error accumulation, the residual force vector is added to the incremental equilibrium equation at the next time step. Thus, the incremental equation of motion including equilibrium correction is written as

$$M_t\Delta\ddot{r}_t + C_t\Delta\dot{r}_t + K_t\Delta r_t = R^E_{t+\Delta t} - (R^I_t + R^D_t + R^S_t) \tag{2.10}$$

By rewriting Equation for dynamic equilibrium at time $t + \Delta t$ and inserting Equation 2.11, the incremental equation expressed by the incremental displacement vector over the time interval $t + \Delta t$, is written

$$\widehat{K}_t \Delta r_t = \Delta \hat{R}_t \tag{2.11}$$

where the effective stiffness, $\widehat{K}_t$, and effective incremental load vector, $\Delta \hat{R}_t$, are defined by the relations.

$$\widehat{K}_t = \frac{1}{\rho(\Delta\tau)^2} M_t + \frac{\gamma}{\beta \Delta\tau} C_t + K_t \tag{2.12}$$

$$\Delta \hat{R}_t = R^E_{t+\Delta\tau} - (R^I_t + R^D_t + R^S_t) + \left(\frac{1}{\beta\Delta\tau}\dot{r}_t + \frac{1}{2\beta}\ddot{r}_t\right) + C_t\left(\frac{\gamma}{\beta}\dot{r}_t + \left(\frac{\gamma}{2\beta} - 1\right)\Delta\tau\ddot{r}_t\right) \tag{2.13}$$

In Equation 2.13, the parameters $\gamma$, $\beta$, and $\theta$ are the time integration parameters based on the Newmark β-family methods.

The Fourier transform (FT) is a mathematical model that facilitates the conversion of signals between two different domains, such as transforming a signal from the frequency domain to the time domain, or vice versa. In signal processing, a time-domain signal can be transformed into the frequency domain using the FT to analyze its frequency components. The mathematical expression for the Fourier Transform is:

$$X(f) = \int_{-\infty}^{+\infty} x(t) e^{-j2\pi f t} dt \tag{2.14}$$

where $x(t)$ is the original time-domain signal, $X(f)$ is its frequency-domain representation, and $f$ represents the frequency. The fundamental concept behind the Fourier Transform is to decompose a signal into a combination of sinusoidal components at different frequencies. This transformation helps in applications such as audio analysis, image processing, and wireless communication, where frequency-domain analysis is essential for filtering and spectral analysis.

After processing a signal in the frequency domain, it is often necessary to convert it back to the time domain using the Inverse Fourier Transform (IFT) to reconstruct the original signal. The mathematical formula for the Inverse Fourier Transform is:

$$x(t) = \int_{-\infty}^{+\infty} X(f) e^{j2\pi ft} df \tag{2.15}$$

where $X(f)$ represents the frequency-domain signal, and $x(t)$ is the reconstructed time-domain signal. The purpose of the inverse transform is to recombine different frequency components into a time-domain waveform. This process is widely used in applications such as image reconstruction, audio signal processing, and radar signal analysis. For example, in MP3 audio decoding, compressed frequency-domain data is transformed back into a time-domain waveform for playback. Further details regarding the numerical time integration methods are given in user document for SIMA (2021) and standard textbooks on structural dynamics, see for instance Clough et al. (1975).

## 2.2 Description of the multi-body system

### 2.2.1 Offshore service vessel

The Fortuna Kingfisher is a sophisticated offshore support vessel currently operating under the Danish flag. Over the past five years, this specialized ship has been extensively involved in conducting foundation inspections for offshore wind farms, utilizing advanced ROV. Figure 2.1 presents both the overview and side view drawings of the Fortuna Kingfisher, offering a comprehensive visual representation of its design and layout. Table 2.1 outlines the vessel's key specifications and technical characteristics, providing essential details about its capabilities and features. All pertinent data, including a detailed panel model of the OSV Fortuna Kingfisher, have been generously supplied by O.S. Energy Ltd. We have chosen these models because O.S. Energy Ltd. generously provided both the models and the necessary data for our research. We are grateful for their support, which made the use of these models possible.

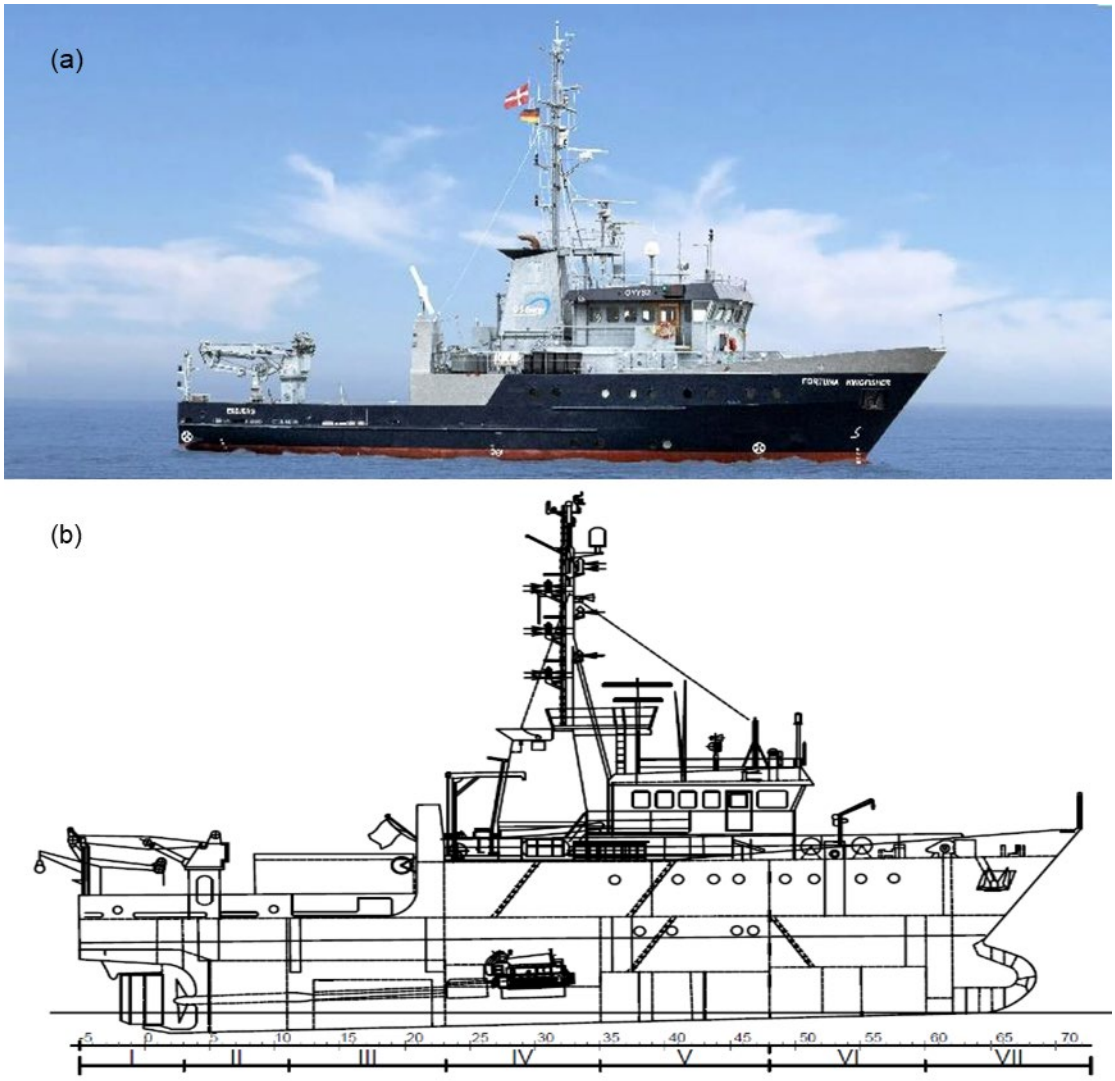


Figure 2.1 Overview (a) and sideview drawing (b) of offshore service vessel - Fortuna Kingfisher (Nuernberg et al., 2021).

Table 2.1 Main dimensions of offshore support vessel – Fortuna Kingfisher.

| Main dimensions | Vessel |
|---|---|
| Length overall (m) | 38.92 |
| Length waterline (m) | 34.60 |
| Length moulded (m) | 32.10 |
| Breadth moulded (m) | 9.20 |
| Depth moulded (m) | 4.50 |

| | |
|---|---|
| Draught (m) | 3.10 |
| Displacement at design water line ($m^3$) | 495.0 |
| Lightship mass (t) | 393 |
| Gross tonnage (t) | 387 |
| Net tonnage (t) | 116 |

### 2.2.2 Fixed wind turbine

The fixed wind turbine for this project is a mono-pile bottom fixed wind turbine located at the DanTysk wind farm. It is a Siemens SWT-3.6-120 Offshore with a tripod support structure. The tower's height is designated as 120 m, and the support structure's column diameter is 6.5 m. Figure 2.2 illustrates the overview and configuration of fixed offshore wind turbine. Its further details are shown in Table 2.2.

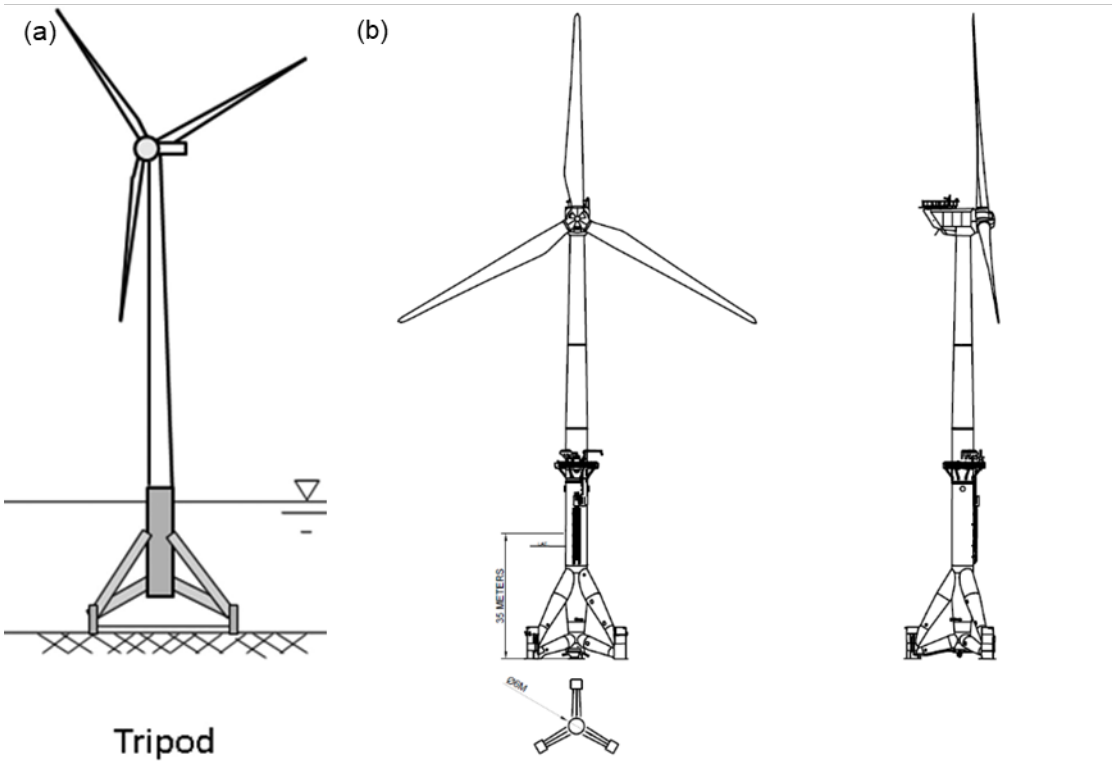


Figure 2.2 Overview (a) and configuration (b) of fixed offshore wind turbine (Nuernberg et al., 2021).

Table 2.2 Particulars of fixed wind turbine.

| Main dimensions | Fixed wind turbine |
|---|---|
| Depth to platform base (m) | 35 |
| Height of tower (m) | 120 |
| Elevation to platform top (m) | 10 |
| Depth to top of taper (m) | 4 |
| Depth to bottom of taper (m) | 12 |
| Platform diameter above taper (m) | 6.5 |
| Platform diameter below taper (m) | 9.4 |

### 2.2.3 Floating wind turbine and mooring line

The floating wind turbine utilized in this study is the NREL 5-MW wind turbine mounted on the OC3-Hywind spar, located in 320 m of water (Jonkman et al., 2010). This turbine is based on the spar-buoy design developed by Statoil of Norway for the "Hywind" project. While the rotor-nacelle assembly of the turbine remains the same as the original version (Jonkman et al., 2009), modifications have been made to the support structure (tower and substructure) and control system characteristics. Figure 2.3 and Table 2.3 illustrate the platform's configuration and features, and more detailed information can be found in the referenced literature (Jonkman, 2010). The numerical model for floating wind turbines was developed by SINTEF, an independent research organization.

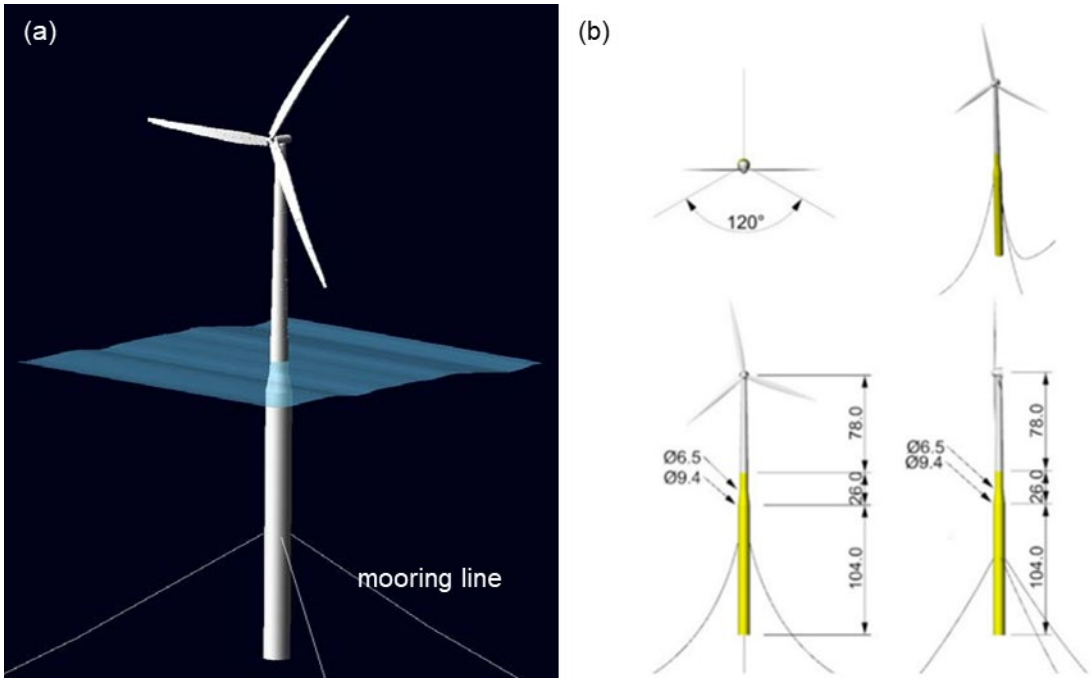


Figure 2.3 Model (a) and illustration (b) of the NREL 5-MW wind turbine on the OC3-Hywind spar (Jonkman et al., 2009).

Table 2.3 Specification of floating wind turbine.

| Main dimensions | Floating wind turbine |
|---|---|
| Depth to platform base (m) | 120 |
| Elevation to platform top (m) | 10 |
| Depth to taper top (m) | 4 |
| Depth to taper bottom (m) | 12 |
| Platform diameter above taper (m) | 6.5 |
| Platform diameter below taper (m) | 9.4 |
| Platform mass (kg) | 7,466,330 |
| Platform roll inertia (kg*m$^2$) | 4,229,230,000 |
| Platform pitch inertia (kg*m$^2$) | 4,229,230,000 |
| Platform yaw inertia (kg*m$^2$) | 164,230,000 |

The Hywind floating platform employs a three-line catenary mooring system to prevent drift. These lines are connected to the platform via a delta connection in the prototype design, enhancing the mooring's yaw stiffness. However, for simplification purposes, this delta connection has been eliminated in the current model. Each mooring line is composed of multiple segments with distinct properties, and the basic properties are shown in Table 2.4.

Table 2.4 Specification of mooring line.

| Properties | Mooring line |
|---|---|
| Number of mooring lines | 3 |
| Angle between mooring lines (deg) | 120 |
| Depth to anchors (m) | 320 |
| Mooring line diameter (m) | 0.09 |
| Mooring line mass density (kg/m) | 77.7066 |
| Mooring line weight in water (N/m) | 698.094 |

### 2.2.4 ROV and TMS system

The offshore support vessel is equipped with an ROV called Seaeye Cougar-XT and specially retrofitted to perform inspection, maintenance, and repair work on facilities located below the water surface. The 3D model of Seaeye Cougar-XT is obtained from Bluestream company, as shown in Figure 2.4. A whole work class ROV system contains ROV and TMS type 8, as shown in Figure 2.5. The ROV remains connected to the TMS during the deployment procedure and detaches from the TMS during the operational phase. The primary characteristics of the ROV and the entire system can be found in Table 2.5 and Table 2.6.

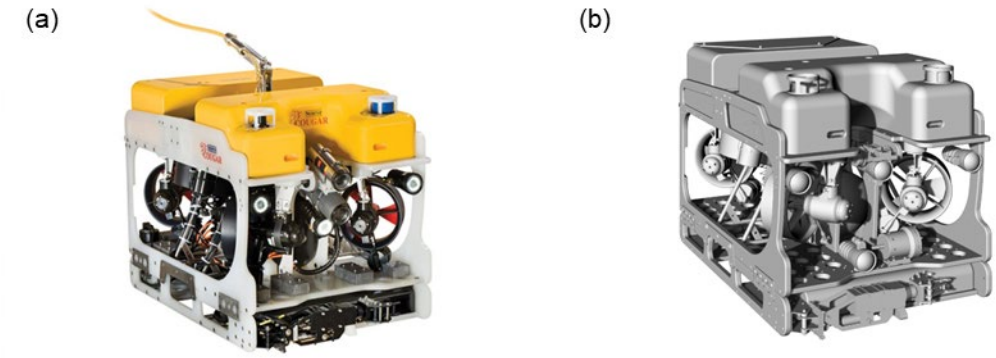


Figure 2.4 Prototype (a) and 3D model (b) of ROV - Seaeye Cougar-XT (SAAB, 2021).

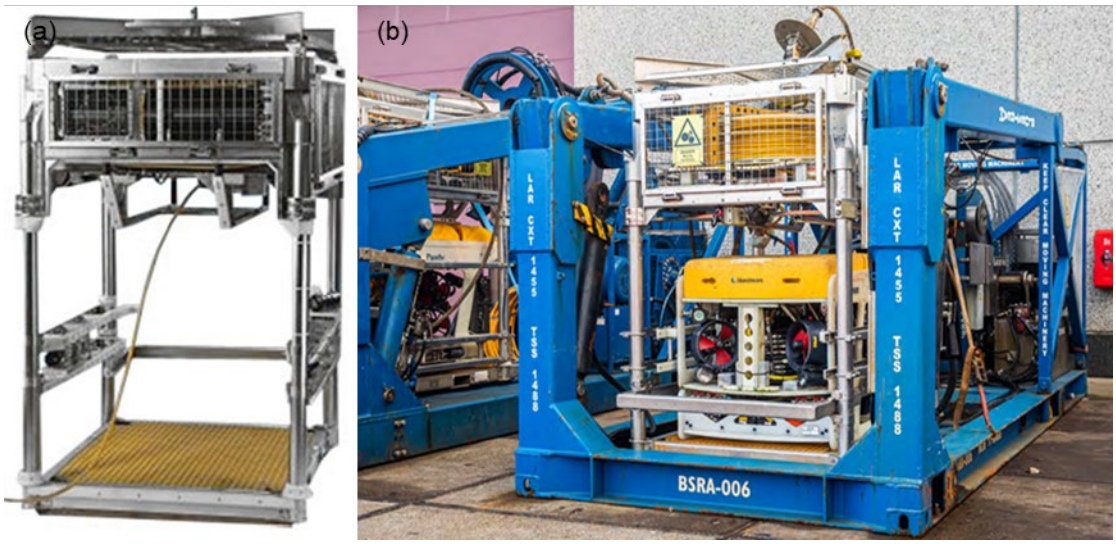


Figure 2.5 Prototype of TMS (a) and the entire system (b) (Marine Vision S.L, 2021).

Table 2.5 Properties of the ROV.

| Main dimensions | ROV |
|---|---|
| Length (mm) | 1515 |
| Width (mm) | 1000 |
| Height (mm) | 790 |
| Launch weight (kg) | 409 |
| Forward speed (knots) | 3.2 |

| | |
|---|---|
| Thrust forward (kgf) | 170 |
| Thrust lateral (kgf) | 120 |
| Thrust vertical (kgf) | 110 |

Table 2.6 Properties of the whole work class ROV and TMS system.

| Properties | TMS | ROV | ROV and TMS |
|---|---|---|---|
| Length (m) | 1.792 | 1.515 | 1.792 |
| Width (m) | 1.491 | 0.790 | 1.491 |
| Height (m) | 2.317 | 1.0 | 2.317 |
| Mass (kg) | 1400 | 409 | 1809 |
| Displacement ($m^3$) | 0.394 | 0.401 | 0.795 |

The ROV can be represented by a simplified structural model consisting of slender elements recommended by the SIMO theory manual (SINTEF Ocean, 2022) due to limitations of available drawings and data. The numerical model of ROV is composed of 65 slender elements and its structural dimensions align with those listed in Table 2.6. The visualization of ROV is shown in Figure 2.15. Certain hydrodynamic coefficients of ROV including added mass and drag coefficients must be provided as inputs to estimate the motion and response as it traverses the wave zone. However, these coefficients are challenging to determine, and there is a scarcity of information and data on ROV correlation coefficients. The added mass coefficients are determined with reference to the hydrodynamic problems in viscous flow of square prisms in the DNV recommended practice (Bjerkholt, 2014; Jenssen, 2015). The drag coefficients are based on the data of characteristic parameters describing the subsea structure in the investigation of fluid dynamics of idealized complex objects from Sarkar and Gudmestad (2010). The ROV is a neutrally buoyant floating body with approximately equal gravity and buoyancy, and the TMS is described as a container carrier module with more gravity than buoyancy but with relatively insignificant excess mass in Sarkar and Gudmestad (2010). The final estimated hydrodynamic coefficients of the ROV model are displayed in Table 2.7.

Table 2.7 The properties and coefficients of slender elements.

| Properties | TMS | ROV | ROV and TMS |
|---|---|---|---|
| Porosity | 0.94 | 0.67 | 0.87 |
| Element number | 39 | 26 | 65 |
| Added mass coefficient | 0.55 | 0.72 | - |
| Linear drag coefficient | 0.3 | 0.3 | - |
| Quadratic drag coefficient | 4.0 | 2.5 | - |

### 2.2.5 Umbilical cable and winch wire

The ROV is connected to the winch crane mounted on service vessel by a cable/rope, and its launch and recovery are conducted using this vessel-based crane. The choice between using a standalone ROV or a complete ROV system depends on the requirements of the task and the operating environment. An umbilical cable is employed for the deployment of standalone ROV (Figure 2.6(b)), while a winch wire is employed for the entire ROV system due to the greater weight (Figure 2.6(a)). The umbilical cable used for launch and recovery of ROV is a 20 mm single mode tether made of Hytrel®, and the single winch wire line is a polyester rope. The data of umbilical cable and winch wire is acquired from Randers Reb and Bridon Bekaert, as shown in Table 2.8. The winch wire model will be used in Chapters 3 and 5, and the umbilical cable model will be used in Chapter 6.

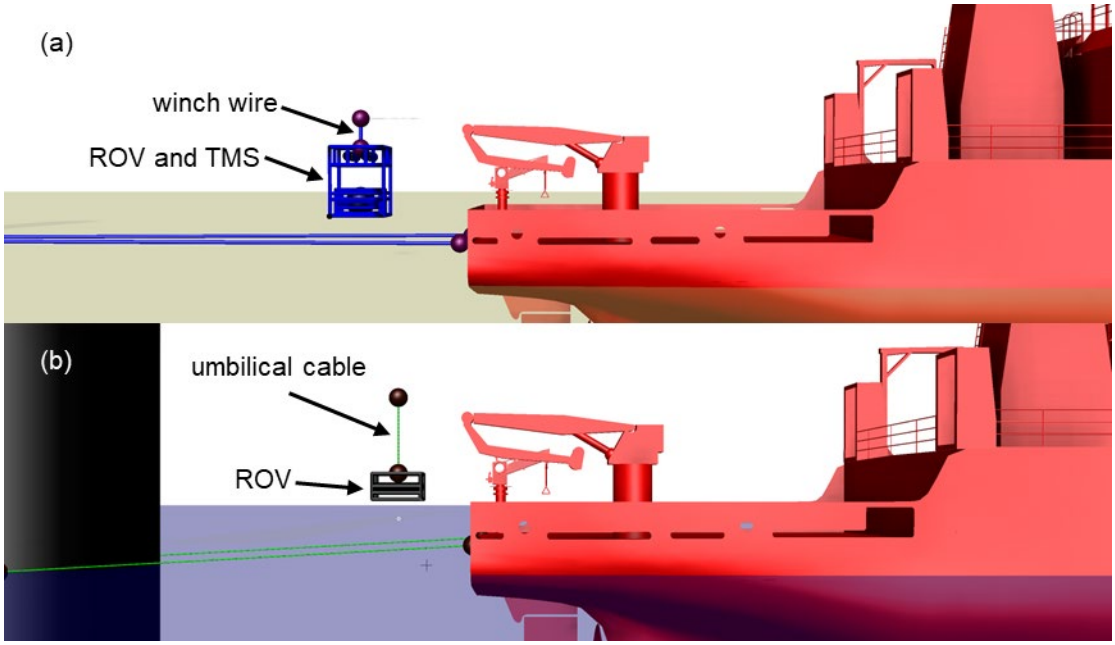


Figure 2.6 Models of winch wire (a) and umbilical cable (b) in SIMA.

Table 2.8 Properties of umbilical cable and winch wire.

| Properties | Umbilical cable | Winch wire |
|---|---|---|
| Outer diameter (mm) | 20.6 | 24.0 |
| Weight in air (kg/m) | 0.582 | 0.26 |
| Weight in seawater (kg/m) | 0.24 | 0.23 |
| Axial stiffness (MN) | 31.67 | 30.0 |
| Bending stiffness (MN) | 6.034 | 5.172 |
| Max dynamic load (kN) | 32.2 | 100.0 |

### 2.2.6 Connecting line

The service vessel is connected to the fixed or floating offshore wind turbine through two connecting wire lines to restrain motion of the vessel at a fixed radius around the foundation (Figure 2.7). The single connecting line is a 3-strand Superflex polyester rope with dimension of 24 mm, and its properties are shown in Table 2.9. The relationship between elongation and load of connecting line is shown in Table 2.10. The

data of connecting lines are acquired from Randers Reb. The connecting line model will be used in Chapters 4, 5 and 6.

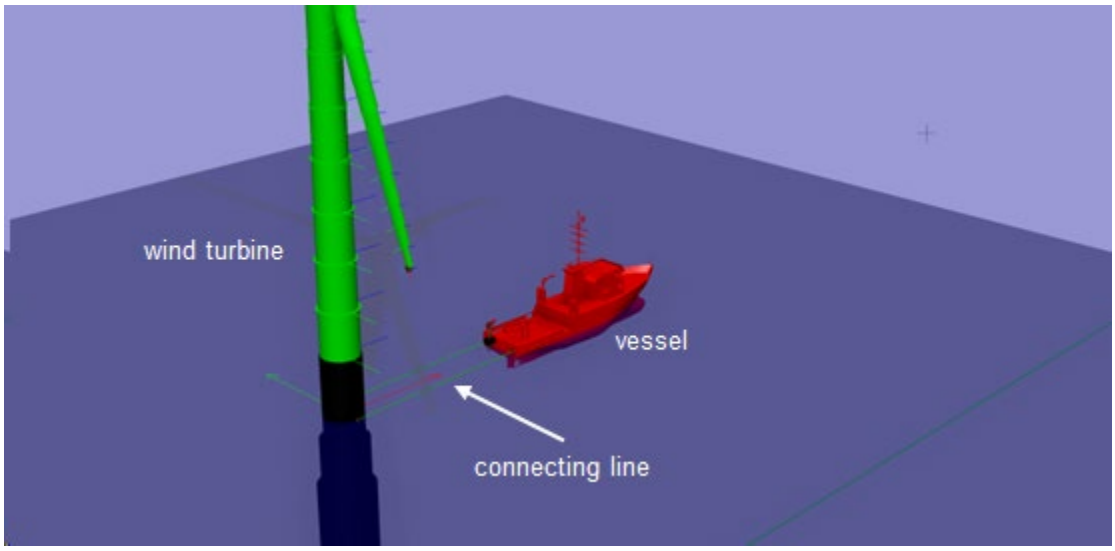


Figure 2.7 Model of connecting line in SIMA.

Table 2.9 Properties of connecting line.

| Properties | Wire line |
|---|---|
| Outer diameter (mm) | 24.0 |
| Weight in air (kg/m) | 0.26 |
| Weight in seawater (kg/m) | 0.23 |
| Axial stiffness (MN) | 30.0 |
| Bending stiffness (MN) | 5.172 |
| MBF (kN) | 100.0 |

Table 2.10 The relationship between elongation and load of connecting line.

| Elongation (%) | Force (N) |
|---|---|
| 0.049 | 318.19 |
| 0.075 | 3210.88 |
| 0.100 | 10081.04 |

| | |
|---|---|
| 0.122 | 19482.25 |
| 0.138 | 30329.86 |
| 0.155 | 50940.26 |
| 0.163 | 66850.11 |
| 0.167 | 78782.44 |
| 0.183 | 89268.48 |
| 0.189 | 100116.09 |
| 0.195 | 108432.59 |
| 0.199 | 111686.85 |

### 2.3 Model development for multi-body system dynamics

The operation of launching and recovering an ROV, a typical offshore crane operation, will be simulated using GeniE, Hydrodynamic Analysis and Stability Analysis (HydroD) and SIMA software developed by DNV in this study. GeniE, an advanced geometric modelling tool for beams, plates and stiffened shells, is used to create the numerical model and generate mesh models. HydroD is a software tool for frequency domain analysis of barges, ships and platforms with advanced wave load analysis options. SIMA is an advanced module for time domain simulation of the motion and position-keeping behavior of complex marine structures, operations and floating systems.

These software tools are used to simulate the displacement, motion response and line tension of the coupled wind turbine, vessel, and ROV model. The mesh models of vessel and wind turbine are generated by GeniE. These mesh models are imported into HydroD, a hydrodynamic and stability analysis software, which is used to calculate the first-order forces and motion transfer functions of the vessel and turbine, generating RAO results. These RAO results are then imported into SIMA, a time-domain analysis software for coupled marine systems, to compute the total motion, tension response, body forces and mass forces. It considers excitation forces, added mass, potential and damping matrices, and environmental forces such as wind waves, swell waves, wind, and currents. The complexity of the model structure is managed using super nodes and

lines. These elements detail system connections, constraints, and dynamic responses. Methodology flowchart of numerical simulation is shown in Figure 2.8.

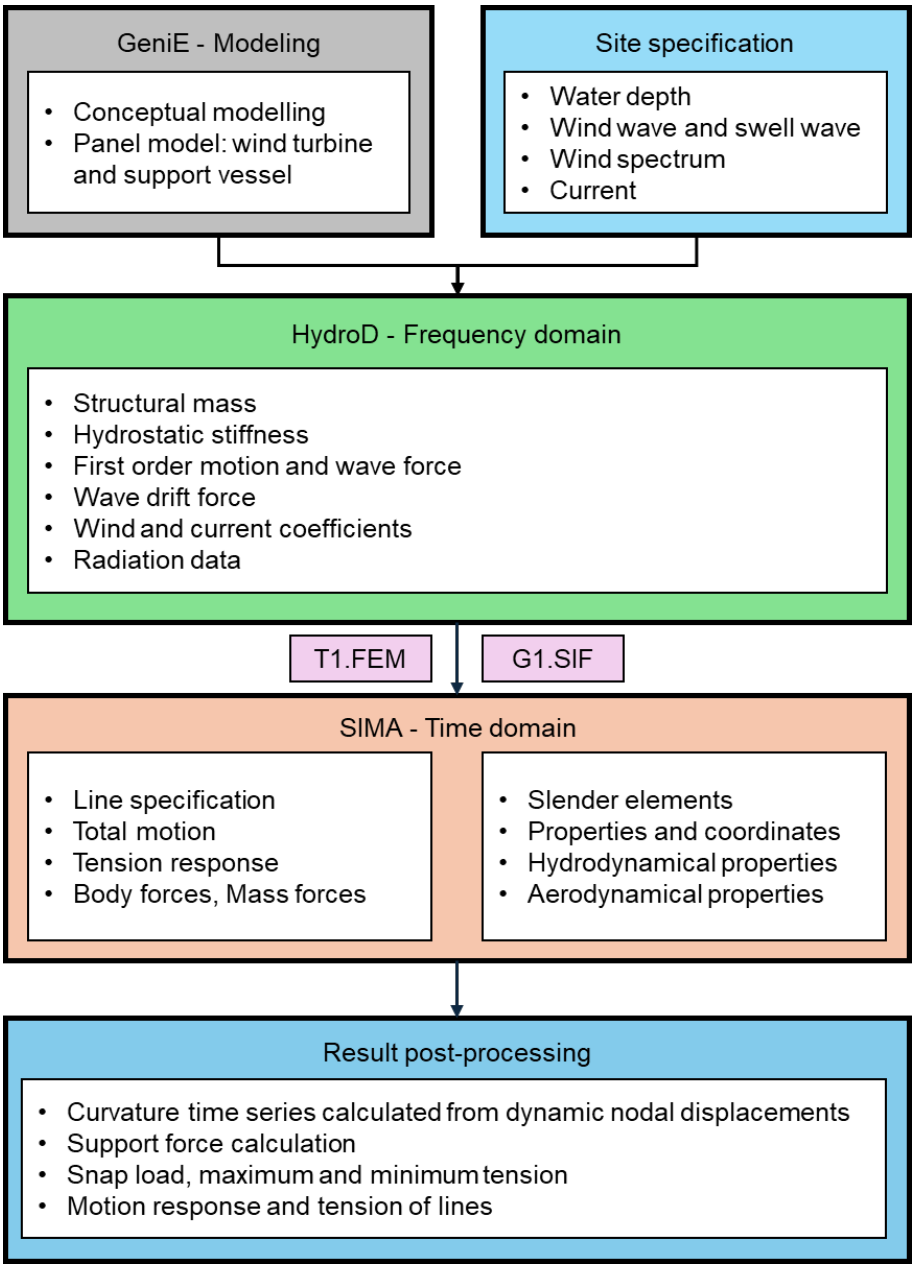


Figure 2.8 Methodology flowchart of coupled wind turbine, vessel and ROV analysis.

The crane tip is modelled as a unified body point integrated with the winch. The motion and response of crane tip are represented by response amplitude operator (RAO) of vessel in frequency domain analysis. The vessel RAO is calculated by HydroD and then imported into SIMA for coupling time domain analysis. The wind turbine has been

simplified to a simple cylinder and is simulated as a fixed mass body point. The winch wire is a separate model that connects the crane tip to the top of ROV and it is conceptualized as a simple wire coupling. Two identical mooring lines are modelled as simple wire couplings used to connect the ship to the wind turbine. The time integration step and time increment are 0.005 s based on the convergence test.

The offshore vessel is located approximately 40 m in front of the wind turbine. The winch that extends and shortens the wire is represented by a crane tip located 5.0 m above the free water surface. The ROV top is connected to the winch by a wire and is located 0.7 m below the position of crane tip. The ROV will be lowered to a depth of 20.0 m below the free surface at the set winch speed after the winch is started, and then the ROV will be lifted out of the water to its initial position at the same speed after the winch stops for a period of time representing the underwater work. The models and specific settings for each chapter will be explained in the respective chapters.

Following the validation against the purposely conducted laboratory experiments of ROV launch and recovery process, and the results of the OSV vessel dynamics and the mooring tension from the previous numerical study (Ren et al., 2022), the present numerical model is applied to investigate the ROV operation onboard a small OSV using a single point mooring system. Numerical simulation is focused on factors crucial to the operation including effects of deployment position, influence of winch speed, and environmental limit to the ROV operation. Based on the detailed study, an improved ROV deployment strategy is recommended for expanding ROV operational capacity onboard a small OSV for offshore wind farms.

### 2.4 Convergence analysis of mesh, strip and time step

Since there are three objects in the hydrodynamic interaction in this study, the panel mesh of service vessel model and the strip of slender element for ROV and TMS model are required. The panel model and mesh model of service vessel are shown in Figure 2.9. Because the coupled vessel and ROV model needs to be hydrodynamically analysed by time domain analysis, a convergence analysis for the time step is also necessary. Figure 2.10 shows the mesh convergence analysis for the case of headed waves and a wave frequency of 1.21 rad/s. The numerical model of ROV and TMS is

composed of 65 slender elements, and each slender element specified is divided into strips with equal length. The strip convergence analysis of ROV and TMS model is shown in Figure 2.11. The convergence analysis of time step for coupled system is shown in Figure 2.12.

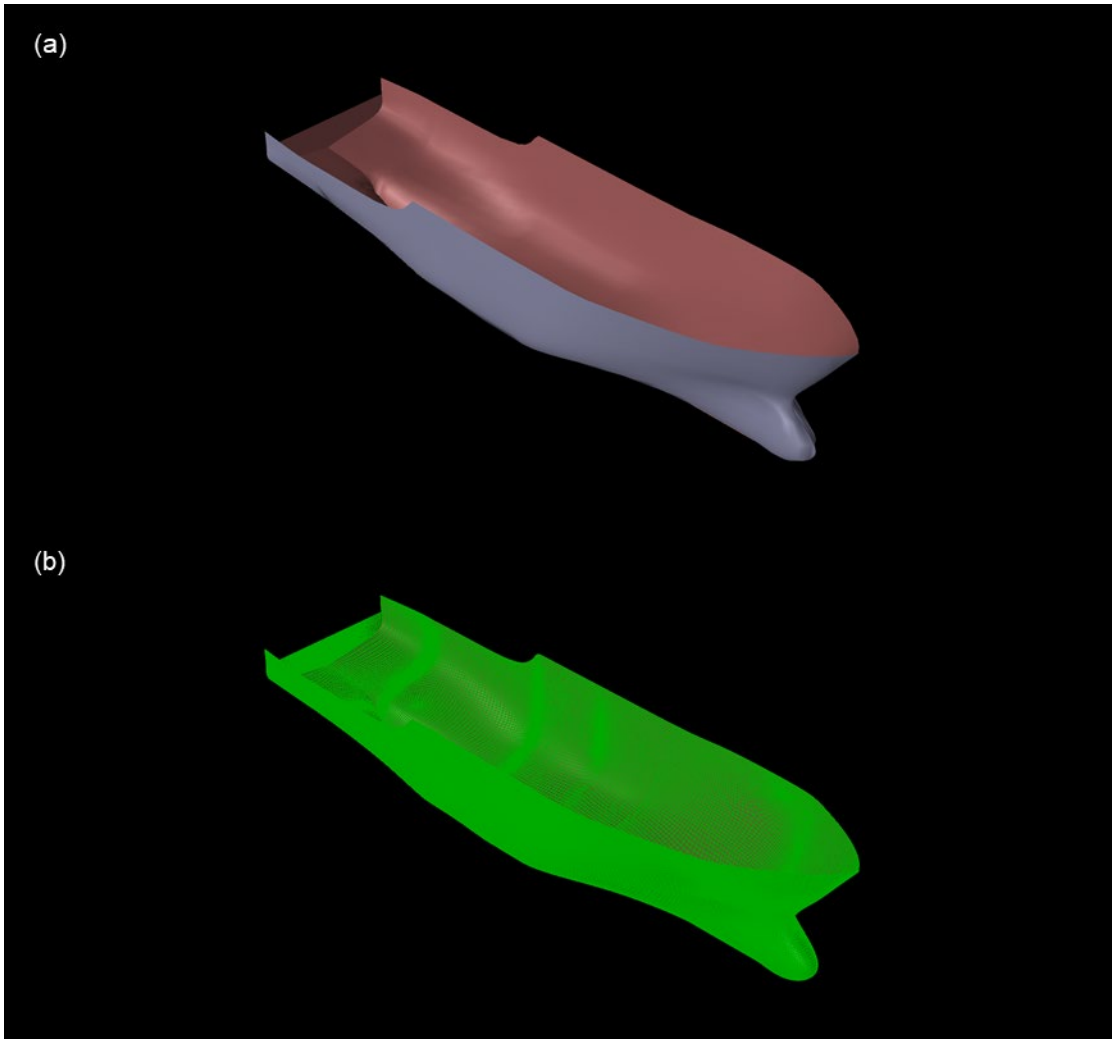


Figure 2.9 The panel model (a) and mesh model (b) of service vessel.

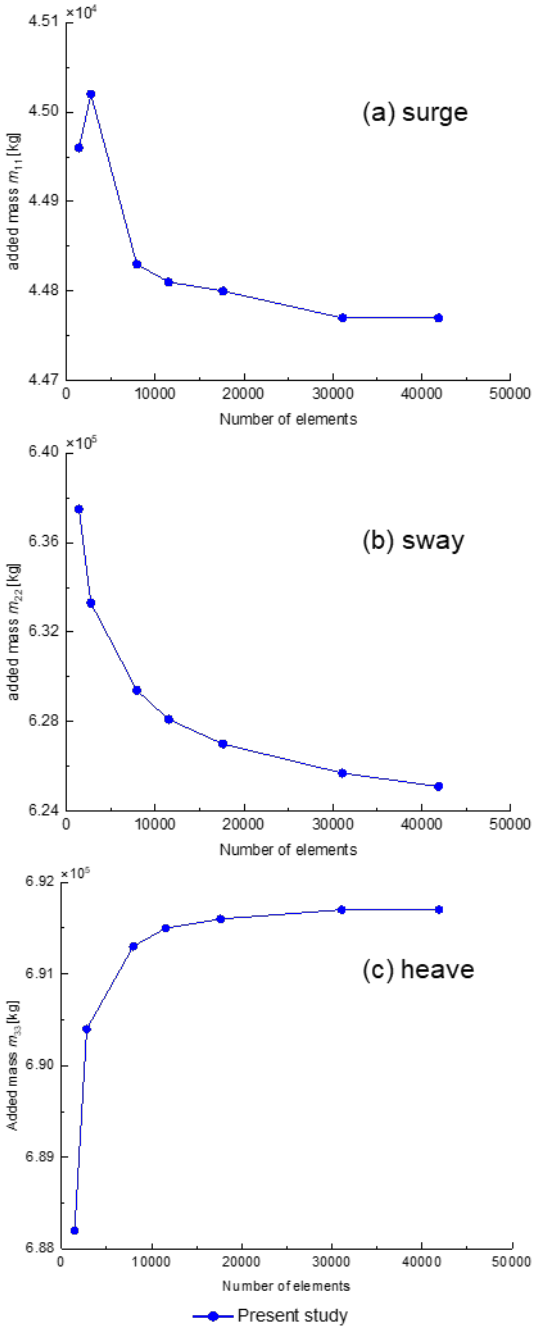


Figure 2.10 Mesh convergence and validation of added mass in surge (a), sway (b) and heave (c) for hull model elements.

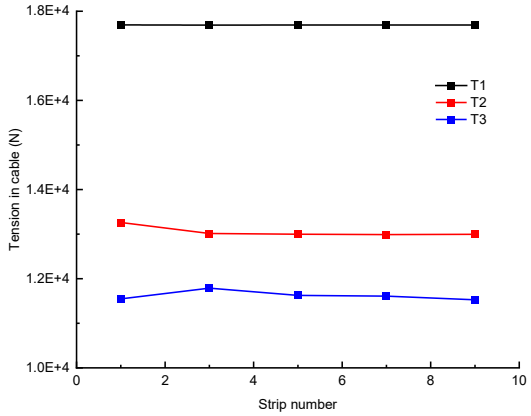


Figure 2.11 Strip convergence of slender element for ROV and TMS model.

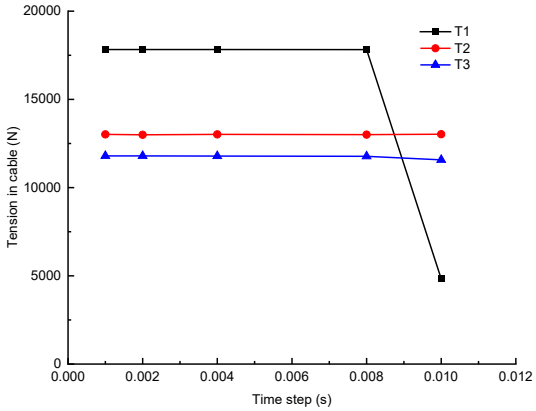


Figure 2.12 Time step convergence of the coupled vessel and ROV model.

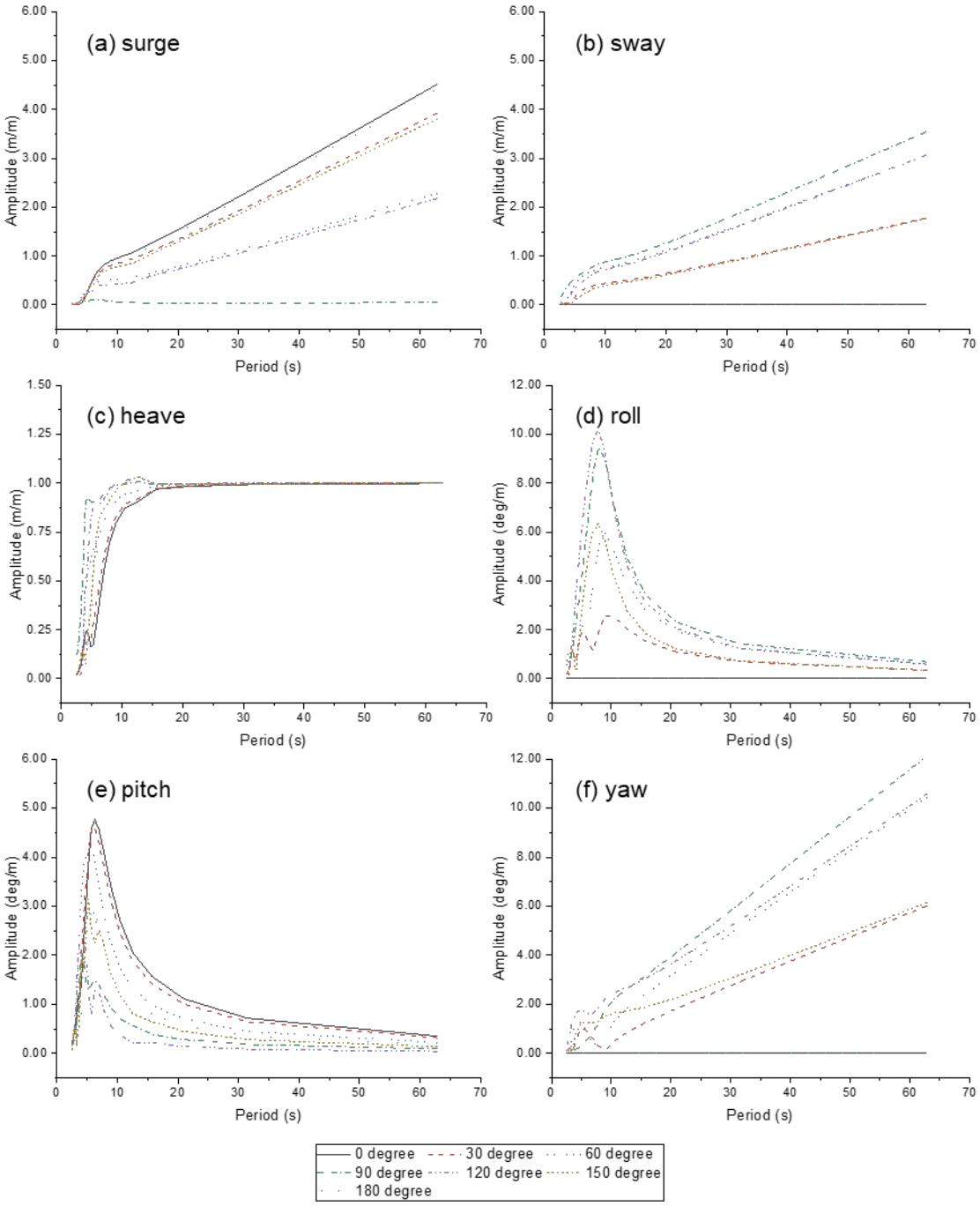


Figure 2.13 The first-order motion of service vessel in different directions under different wave periods.

Figure 2.10 shows the first-order force of the offshore support vessel in different directions under different mesh numbers obtained. As the mesh number increases, the first-order forces in the surge, sway and heave directions continue to converge very fast. When the mesh number is larger than 20,000, the first-order force in all directions converges. Approximately 35,000 ship hull panel elements are sufficient to accurately

estimate wave loads in the present case. Figure 2.11 shows the tension in winch wire under different strip numbers. Figure 2.12 shows the tension in winch wire under different time steps. T1, T2 and T3 are different times for launching and recovering ROV and TMS system. T1 represents that ROV and TMS is still in the air, T2 represents the descending stage, and T3 indicates that the ROV and TMS is fully submerged in water. When the number of strips is greater than 5, the tension in winch wire converges. In time domain analysis, the tension in winch wire converges when the time step is less than 0.006 s. Clearly, the figures indicate that the present numerical model is reliable. Figure 2.13 shows the first order motion transfer function of service vessel.

## 2.5 Experimental test and validation of ROV deployment

### 2.5.1 Scaling System

According to Buckingham's π theorem (Buckingham, 1914), all variables involved in the experimental test can be expressed through a set of dimensionless parameters (π). In this experiment, three parameters are chosen to normalize the others: the ROV length (L), gravitational acceleration ($g$), and water density (ρ). The resulting dimensionless parameters are:

$$\pi_1 = \mathrm{F}/(\rho \mathrm{g} \mathrm{L}) \tag{2.16}$$

$$\pi_2 = \mathrm{M}/(\mathrm{g}L^3) \tag{2.17}$$

$$\pi_3 = \mathrm{k}/(\rho \mathrm{g}L^2) \tag{2.18}$$

$$\pi_4 = \mathrm{H}/\mathrm{L} \tag{2.19}$$

$$\pi_5 = T^2(\frac{g}{L}) \tag{2.20}$$

$$\pi_6 = v^2/(gL) \tag{2.21}$$

where F is umbilical axial force (N), M is ROV mass (kg), k is umbilical axial stiffness (N/m), H is wave height (m), T is wave period (s) and ν is winch speed (m/s).

The normalizing parameters are scaled as follows:

$$L_{model}: L_{prototype} = 1:10 \tag{2.22}$$

$$\rho_{model}: \rho_{prototype} = 1:1 \tag{2.23}$$

$$g_{model}: g_{prototype} = 1:1 \tag{2.24}$$

The normalized parameters are scaled by ensuring the similitude of the dimensionless parameter between model and prototype, which brings to scaling system presented in above equations The resulted scaling system is similar to Froude scaling system.

$$F_{model}: F_{prototype} = 1:1000 \tag{2.25}$$

$$M_{model}: M_{prototype} = 1:1000 \tag{2.26}$$

$$k_{model}: k_{prototype} = 1:100 \tag{2.27}$$

$$H_{model}: H_{prototype} = 1:10 \tag{2.28}$$

$$T_{model}: T_{prototype} = 1:\sqrt{10} \tag{2.29}$$

$$\nu_{model}: \nu_{prototype} = 1:\sqrt{10} \tag{2.30}$$

### 2.5.2 Experimental setup

To provide reliable data of cable dynamics during ROV deployment for validate the numerical model developed this study, the experiment is conducted in a wave flume at the Kelvin Hydrodynamics Laboratory, University of Strathclyde. The purpose of this

experiment is to validate the process of ROV launch and recovery by comparing the tension in umbilical during experimental test and in numerical simulation. The umbilical is introduced in Section 2.2.5. An electric motor representing the crane tip motion and winch operation is mounted on a rigid frame 1.5 m above the water surface. It worth noting that it is difficult to obtain a wire for model testing with exact mechanical properties consistent with the scaling parameters of the actual wire, a soft rope with low bending stiffness was chosen for connecting the electric motor and the ROV model. The rope is supported by a pulley mounted on the frame. A load cell is placed between the pulley and the ROV model to monitor and record the axial load in the wire representation. The tank is filled with fresh water to a depth of 1.1 m. The ROV is positioned at the midpoint of wave flume to access the area with stable wave condition. The wave generator on one side of the water tank generates the set waves, and a wave gauge is installed 0.5 m in front of the position of the ROV model to measure the wave characteristics and transformation. It is noteworthy that the experiment does not account for the motion of vessel. Similarly, in Section 2.5.4, the validation of the numerical simulation results excludes the ship's motion (the ship is set to be stationary). In the subsequent Chapter 3, 4, 5 and 6, the ship's motion is included in the numerical simulations. The picture of field measurement and schematic of the experimental setup are shown in Figure 2.14.

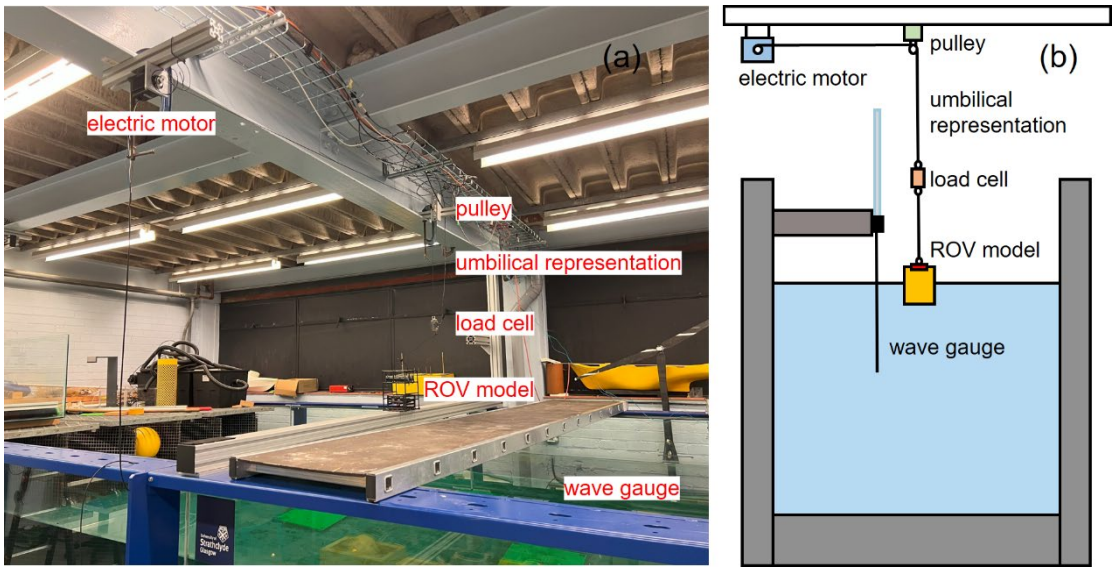


Figure 2.14 Picture of field measurement (a) and sketch of experiment setup (b).

### 2.5.3 ROV-umbilical model

The experiment uses a 1:10 work class ROV model composed of several small cylinders. The parameters of the ROV prototype and model are shown in Table 2.11. The shape and volume of each cylinder are determined by the pultruded carbon fibre pipe shell, and the weight is determined by the inner core made of stainless-steel rods. The experiment model achieves the same properties as each slender element in the numerical simulation at the scale dimension. The ROV prototype, numerical model and experimental model are shown in Figure 2.15. The characteristics of waves at a specific location and moment often have a significant impact on the ROV. However, the properties of irregular waves are difficult to precisely define and reproduce at any given time and place. In contrast, calm water and regular waves provide more controllable experimental conditions, making it easier to study the influence of specific variables on the launch and recovery process while ensuring the repeatability of experiments. Therefore, calm water and regular waves are chosen as the testing conditions for such experiments. Launch and recovery operation tests are conducted in calm water and regular waves, and the time histories of wire tension are recorded. The wave height and period of regular waves are shown in Table 2.12.

Table 2.11 Dimensions of ROV prototype, numerical and experimental model.

| Dimensions | Prototype | Simulation | Experiment |
|---|---|---|---|
| Length (m) | 1.792 | 1.792 | 0.18 |
| Width (m) | 1.491 | 1.491 | 0.15 |
| Height (m) | 2.317 | 2.317 | 0.23 |
| Mass (m) | 1809 | 1809 | 1.81 |
| Displacement ($m^3$) | 0.795 | 0.795 | $0.80 \times 10^{-3}$ |
| Weight in water (kg) | 996.2 | 996.2 | 1.00 |

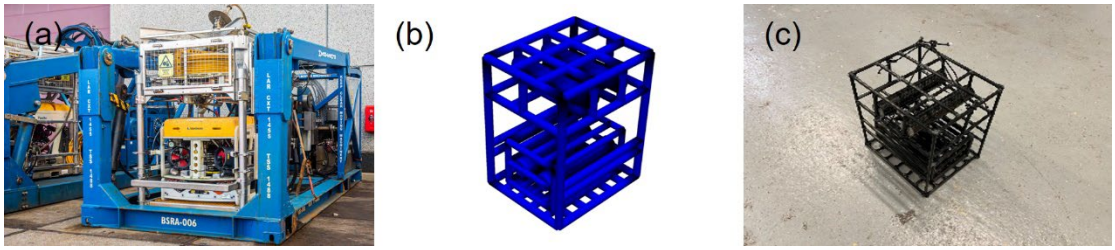


Figure 2.15 Prototype (a), numerical model (b) and experimental model (c) of ROV.

Table 2.12 Experimental test conditions of regular waves.

| Water | Conditions | Prototype | Simulation | Experiment |
|---|---|---|---|---|
| Calm water | Winch speed (m/s) | 0.5 | 0.5 | 0.16 |
| Regular waves | Wave height (m) | 0.60 | 0.60 | 0.06 |
| | Wave period (s) | 7.03 | 7.03 | 2.22 |
| | Winch speed (m/s) | 0.5 | 0.5 | 0.16 |

At the start of the test, the ROV is positioned 0.5 m below the water surface and then lowered to a depth of 1.5 m below the surface (a descent of 2.0 m) at a selected winch speed to simulate the launch process. Due to the short initial distance between the ROV and the wave tank's water surface at the beginning of the launch, it is not possible to smoothly accelerate the winch speed. Therefore, in all experiments, the winch is abruptly started at the selected speed without an acceleration phase. This unavoidable sudden change in winch speed induces transient fluctuations in the cable tension, which dissipate after a certain period. At the end of the descent, when the ROV reaches a depth of 1.5 m, the winch operation is abruptly stopped, generating another transient tension fluctuation. A 30-second delay is then applied to prevent the mixing of transient fluctuations between consecutive deployment and retrieval simulations. Subsequently, the winch is abruptly started in the reverse direction at the same speed to simulate the recovery process. At the end of the recovery, when the ROV returns to a depth of 0.5 m, the winch is suddenly stopped. Another 30-second delay is then applied before the entire launch-delay-recovery process is repeated at a different winch speed.

### 2.5.4 Validation of ROV deployment

The experimental tests first simulated the launch procedure and then the recovery phase. Due to the short initial distance between the bottom of ROV model and the water surface, the winch is suddenly activated at a selected speed excluding an acceleration procedure. Sudden changes in winch speed when starting and stopping inevitably result in brief fluctuations in wire tension that disappear after a certain duration. Figure 2.16 shows a set of snapshots of ROV launch test in regular waves. The ship motion in numerical simulation is removed by restraining six degrees of freedom of the hull to achieve conditions comparable to those in the experiment. The experimental test results at model scale are scaled up and compared with the numerical simulation results at full scale, as shown in Figure 2.17. The experimental data are processed using a low-pass filter with a cutoff frequency of 2 Hz. The free water surface positions in ROV launch operation are shown in Figure 2.18.

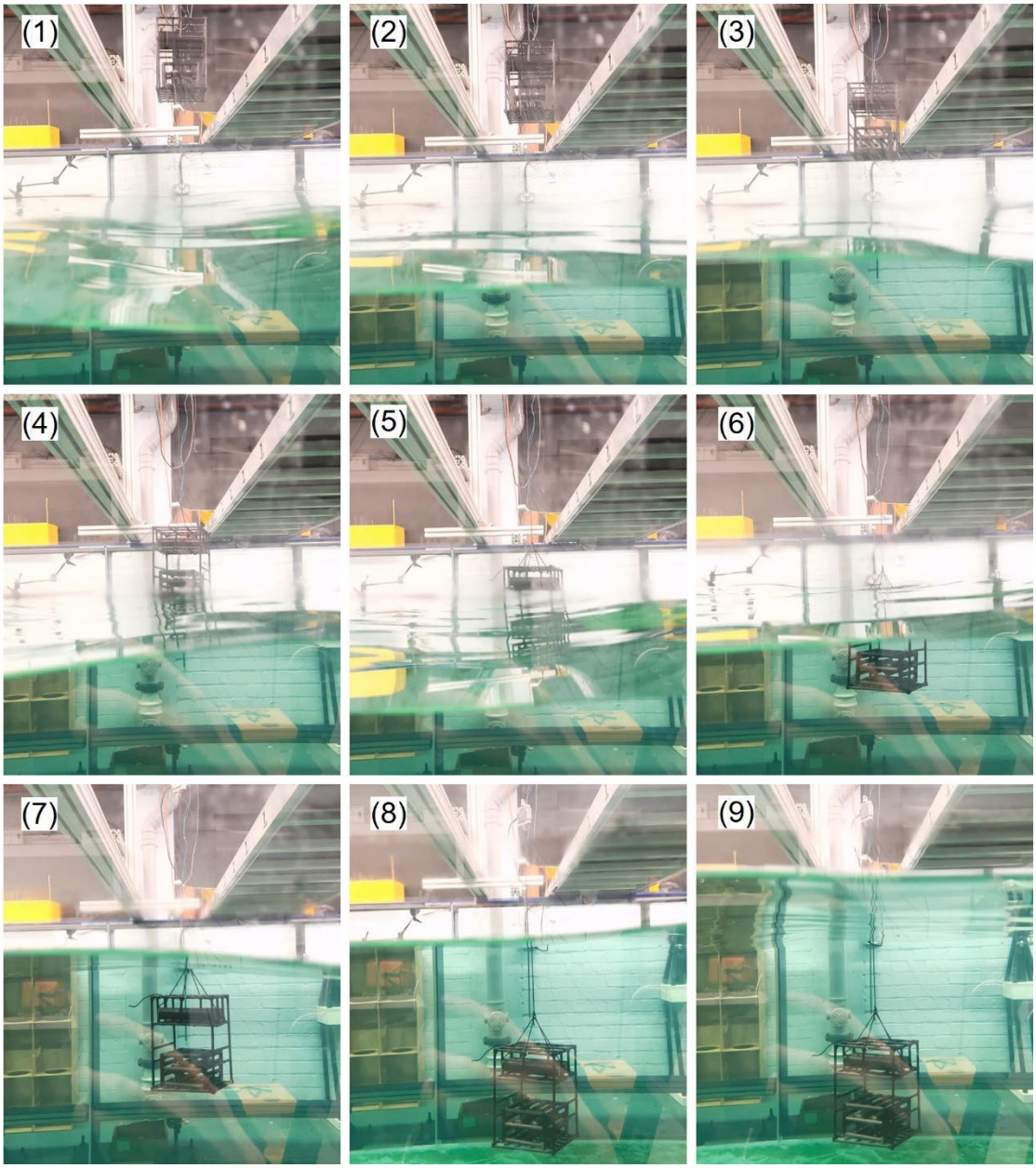


Figure 2.16 Snapshots of ROV launch operation in regular waves.

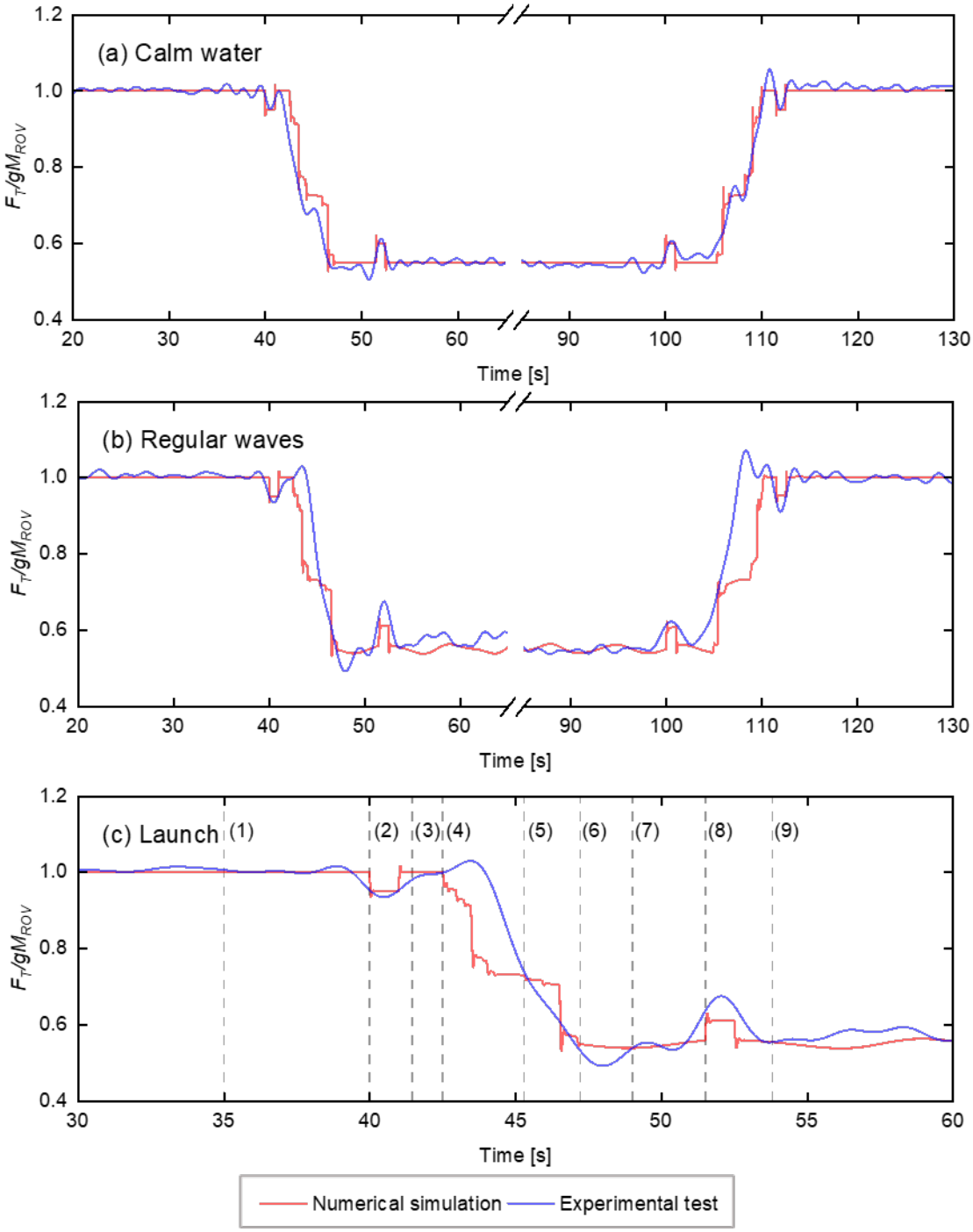


Figure 2.17 Comparison of dynamic tensions in wire from simulation and test in calm water (a), regular waves (b) and launch phase in regular waves (c).

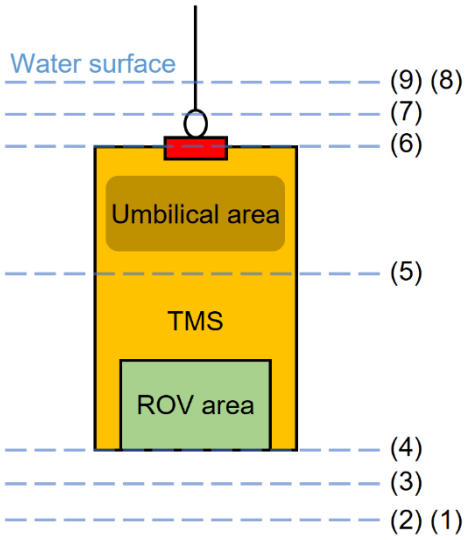


Figure 2.18 The free water surface positions in ROV launch operation.

The serial numbers (1) - (9) represent the snapshot of the shooting moment of the ROV launch operation in regular waves in Figure 2.16, the time instants in the dynamic tensions in the wire from the simulation and test results in Figure 2.17(c), and the free water surface positions in the ROV launch operation in Figure 2.18. These serial numbers correspond across the three parts. By observing Figs. 6-8, the ROV initially remains stationary in air and the wire tension is equal to the object gravity in case as shown in Figure 2.16(1). A sudden slack of wire occurs when the speed is transferred from the wire to the load cell after winch starts in Figure 2.16(2) which causes a rapid reduction and then recovery of the tension. Figure 2.16(3) represents the uniform linear motion of ROV in vertical direction in air. The bottom of the ROV touches the free water surface in Figure 2.16(4) and the wire tension decreases with increasing buoyancy. The load components that make up the dynamic force are the slamming impact force from waves on the bottom of ROV and the inertial force. The slamming impact force is controlled by the relative velocity between the ROV and waves. Figure 2.16(5) shows a slight decrease because the buoyancy volume change in middle section is smaller compared to the ROV storage area and wire storage area. The load components including drag force, mass force and inertial force act together on the ROV. The mass force is composed of the hydrodynamic mass of ROV submerged part and the acceleration of water particles. The ROV is fully submerged in Figure 2.16(6), and then the ROV continues to move a certain distance in water represented by Figure 2.16(7).

The load components are drag forces and mass forces on the ROV. It is seen that the crane stops descending showing in Figure 2.16(8) and a sudden increase in wire tension will occur due to the downward vertical inertia of ROV. Finally, the launch procedure ends and the ROV stays in the working position represented by Figure 2.16(9). The wire tension for the recovery procedure is reversed. The results of numerical simulation show a good agreement with experimental measurements with similar phase trend in Figure 2.17, indicating that the present numerical model is reliable with high degree of accuracy.

## 2.6 Verification and validation of coupled vessel-wind turbine model

To verify and validate the effectiveness of coupled vessel-wind turbine model, the numerical simulation results from this study are compared with full-scale measurement data during field operation of offshore wind farm O&M and numerical simulation results of Ren et al. (2022). The purpose of this section is to verify and validate the coupled vessel-wind turbine model by comparing the tension in connecting lines, as shown in. The connecting line is introduced in Section 2.2.6. Without detailed information of ROV cable dynamics, both the field measurements and numerical simulation of Ren et al. (2022) focused on the tension in connecting lines of the SPMS during the operation. The specific environmental conditions applied during numerical simulations are detailed in Table 2.13. These conditions correspond to the scenarios when service vessels docked at wind turbines for cases numbered 26 and 72 in the DanTysk wind farm. Figure 2.20 illustrates the comparison between the actual measured values and the numerical simulations for the maximum and average tensions of connecting line under cases 26 and 72, respectively.

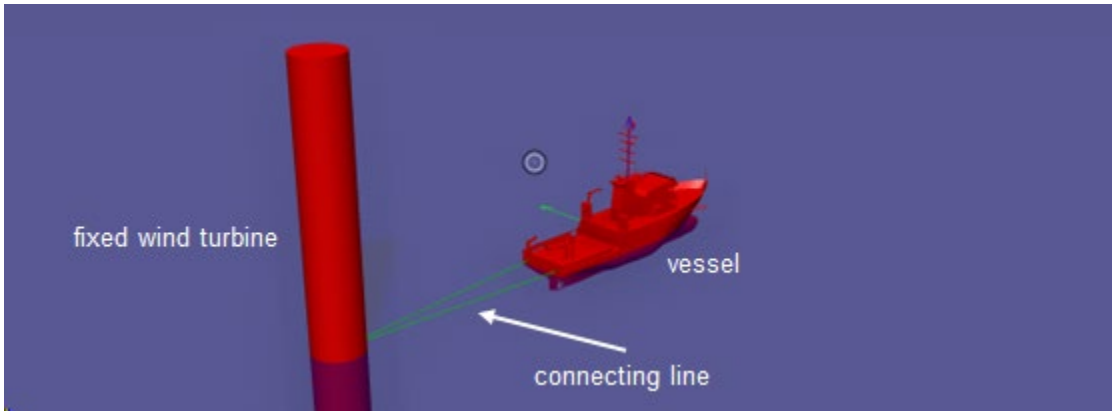


Figure 2.19 The numerical model of coupled vessel-wind turbine.

Table 2.13 Environmental data of condition 26 and 72 collected from DanTysk wind farm.

| Environment | | Condition 26 | Condition 72 |
|---|---|---|---|
| Wind | Direction (deg) | 150 | 125 |
| | Speed (m/s) | 2.4-3.6 | 3.6-7.9 |
| Wind wave | Direction (deg) | 150 | 125 |
| | Significant wave height (m) | 0.2 | 0.5 |
| Swell wave | Direction (deg) | 220 | 250 |
| | Significant wave height (m) | 0.2 | 0.2 |
| Current | Direction (deg) | 125 | 325 |
| | Velocity (m/s) | 0.07-0.15 | 0.14-0.22 |

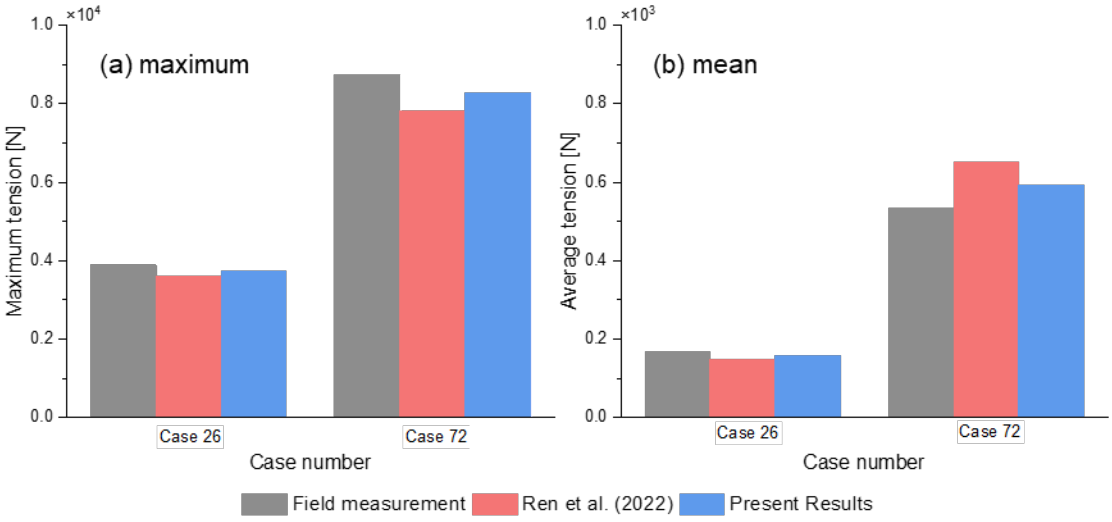


Figure 2.20 Comparison between the field measurement, Ren et al. (2022) and the present numerical simulation of maximum (a) and mean (b) tension in connecting line.

In Figure 2.20. "Field Measurements" refers to the full-scale field measurements from the literature; "Ren et al. (2022)" denotes the numerical simulation results from the same literature; and "Present Results" represents the results from the present numerical simulation results of this study. The differences between the results of this study and the two sets of results from the literature are approximately 5.0% for both maximum and mean tension under case 26 in Figure 2.20. However, the differences in maximum and average tensions are about 5% (Figure 2.20(a)) and 10% (Figure 2.20(b)) under case 72, respectively. The discrepancies in maximum and mean tensions of connecting lines under condition 72 are slightly larger than those under condition 26. The numerical results from this study are comparable to the full-scale measurements and the numerical results of Ren et al. (2022) for both cases, confirming the reliability of the present model developed in this study. Thus, the couple model will be applied to the comprehensive number simulation of a vessel coupled with a fixed or a floating offshore wind turbine focusing on ROV deployment during offshore wind farm O&M.

# 3 Dynamic analysis of launching and recovering process of ROV from a small OSV

The aim of this Chapter is to investigate the dynamic response of the crane tip, ROV, and winch wire during offshore crane operations. This study utilizes numerical simulations to analyze the variations in winch wire tension under different sea conditions, with a particular focus on the deployment and recovery of the ROV in irregular wave environments, as well as the impact of winch speed on wire tension. The crane tip is modelled as a unified body point integrated with the winch. The motion and response of crane tip are represented by RAO of vessel in frequency domain analysis. The vessel RAO is calculated by HydroD and then imported into SIMA for coupling time domain analysis. The time integration step and time increment are 0.005 s based on the convergence test. The same settings are used in Chapter 3, 4, 5 and 6. The offshore vessel is located approximately 40 m in front of the wind turbine, as shown in Figure 3.1. The environmental data used in numerical simulation is shown in Table 3.1.

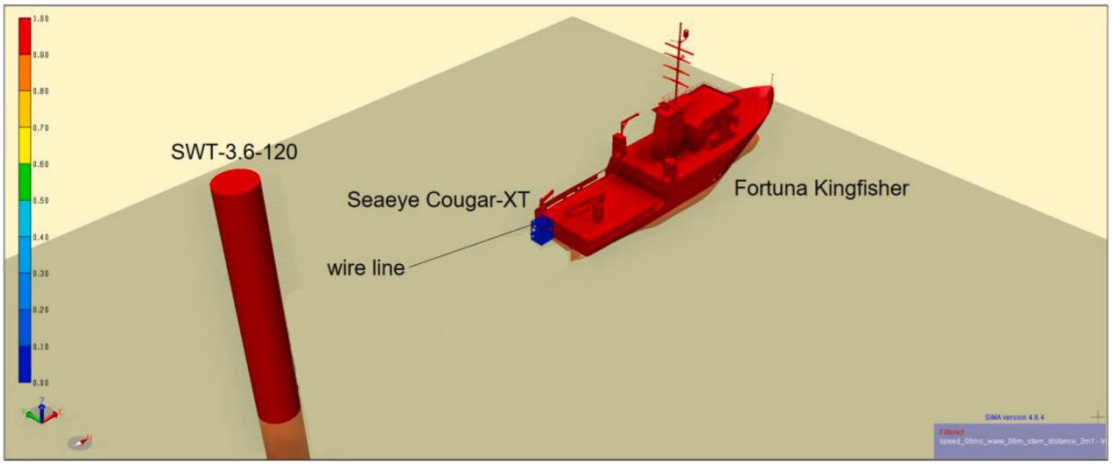


Figure 3.1 The numerical model of support vessel and ROV in SIMA.

Table 3.1 The environmental data used in numerical simulation.

| Sea conditions | Properties | Values |
|---|---|---|
| Wind wave | Direction (deg) | 330/SW |
| | Significant wave height (m) | 0.5 - 1.25 |
| | Peak periods (s) | 3.0 – 5.0 |
| Swell wave | Direction (deg) | 40/SE |
| | Significant wave height (m) | 0.2 |

| | | |
|---|---|---|
| | Peak periods (s) | 4.5 |
| Wind | Direction (deg) | 330/SW |
| | Velocity (m/s) | 5.4 |
| Current | Direction (deg) | 305/SW |
| | Velocity (m/s) | 0.07 - 0.14 |

### 3.1 Stationary analysis of winch wire tension in irregular waves

When the lower part of ROV is at the still water level, the winch wire supports the full weight of ROV, while the lower part of ROV is continuously impacted by sea waves, potentially leading to higher average tension and sudden load spikes. Consequently, a stationary analysis of dynamic tension in winch wire was conducted under irregular wave conditions with a significant wave height of 1.0 m and a peak period ranging from 3.5 to 5.0 s, within the operational limit. It is recommended that the numerical simulation for marine crane operations be conducted within a 30-minute period, including contingency time (DNV, 2017). During the numerical simulation, the ROV is positioned so that its bottom just touches the water surface, with no winch speed applied, and the total simulation duration is 30 minutes. Table 3.2 provides stationary analysis of dynamic tension in winch wire under different sea conditions, while the time histories of dynamic tension in winch wire for each sea state are presented in Figure 3.2.

Table 3.2 Stationary analysis of dynamic tension in winch wire under different sea states.

| Wave peak period (s) | 3.5 | 4.0 | 4.5 | 5.0 |
|---|---|---|---|---|
| Mean tension (N) | 16452.9 | 16403.0 | 16256.5 | 16160.4 |
| Minimum tension (N) | 11407 | 11763 | 10859 | 10911 |
| Maximum tension (N) | 22085 | 21693 | 21274 | 21537 |

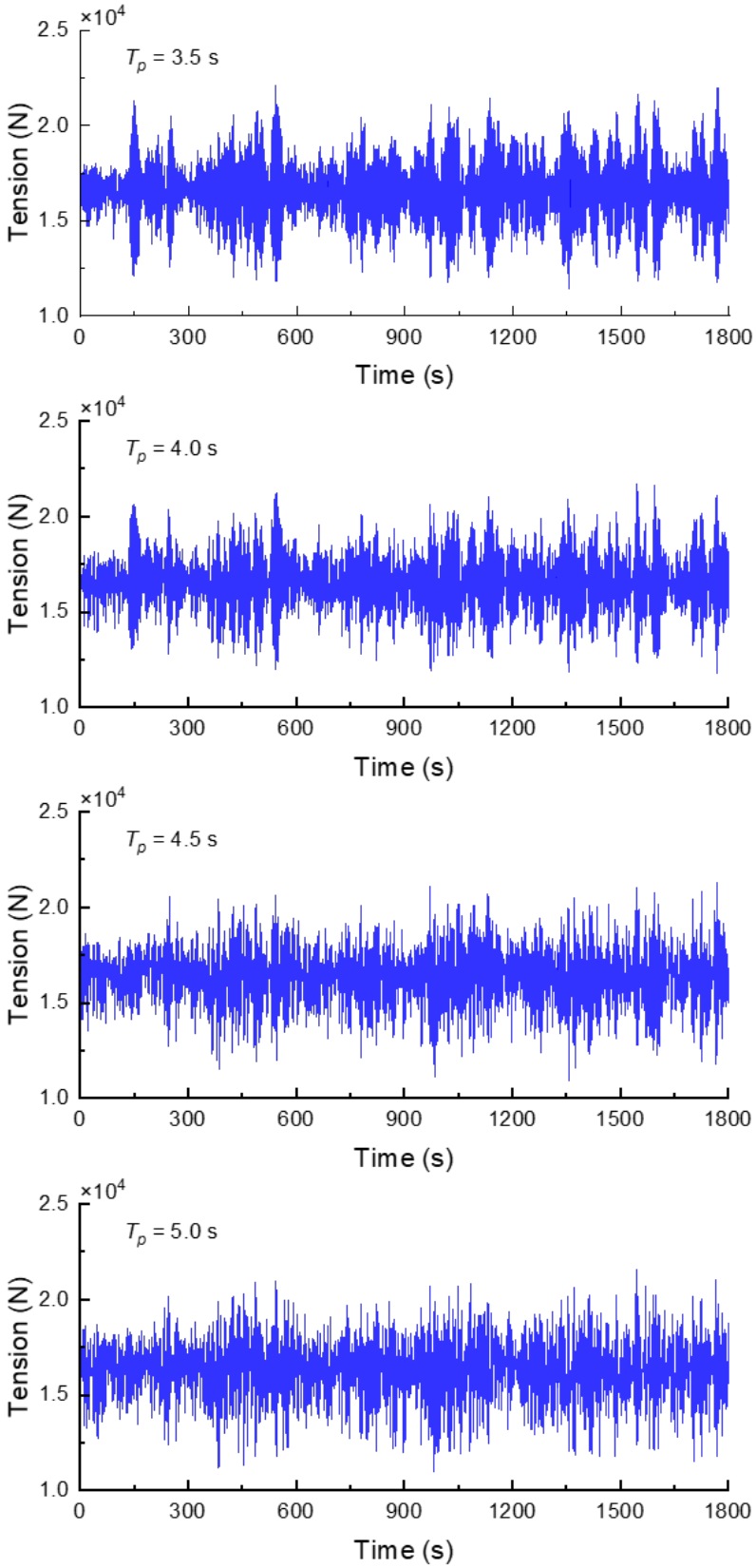


Figure 3.2 Time histories of dynamic tension in winch wire under different sea states.

According to the time histories of dynamic tension in winch wire under different sea states in Figure 3.2, the maximum tension in winch wire frequently exceeds the total weight of ROV, leading to snap loads. The stationary results presented in Table 3.2 indicate that as the wave period increases, the average, minimum and maximum tension in winch wire exhibit similar values. The overall trend shows a slight decrease in both average and maximum tensions, likely due to the reduced likelihood of ROV encountering maximum wave heights. However, the cable tension at the 4.0 s period was slightly higher than at other wave periods, which may be attributed to the nonlinear behavior of transient loads and the significant relative motion between the ROV, TMS systems, and the crane in the 4.0 s sea state. When the bottom part of the ROV and TMS system is in contact with still water, the connecting cables are likely subjected to maximum tension due to snap loads caused by slack cables.

### 3.2 Repeated launch through wave zone

The launch and recovery of ROV mainly include two processes of descent and ascent. Because the sea conditions are irregular waves, the tension of the cable is not the same every time when descending and ascending. Multiple simulations are required for each sea state at each stage so that good estimates of maximum and minimum cable tensions can be obtained. Therefore, the analysis is performed for the same operationally limited sea conditions. The initial position of the ROV system is 7.0 m above the free surface. Before the crane is operated, the ROV system will be stationary for a period 10 s in the initial position, and then the winch is started at a running speed of 0.5 m/s. When the ROV descends to a certain position where it is completely submerged, the winch stops, and 10 simulations are run for each sea state. The statistics for all sea state analysis are listed in Table 3.3, and the time histories of dynamic tension in winch wire for each sea state are shown in Figure 3.3.

Table 3.3 Stationary analysis of dynamic tension in winch wire when lowering ROV in different sea states.

| Wave peak period (s) | 3.5 | 4.0 | 4.5 | 5.0 |
|---|---|---|---|---|
| Mean tension (N) | 13449 | 13386.1 | 13392.3 | 13391.8 |

| | | | | |
|---|---|---|---|---|
| Minimum tension (N) | 3823.3 | 4127 | 3866.7 | 4231.4 |
| Maximum tension (N) | 18555 | 18695 | 18990 | 19527 |

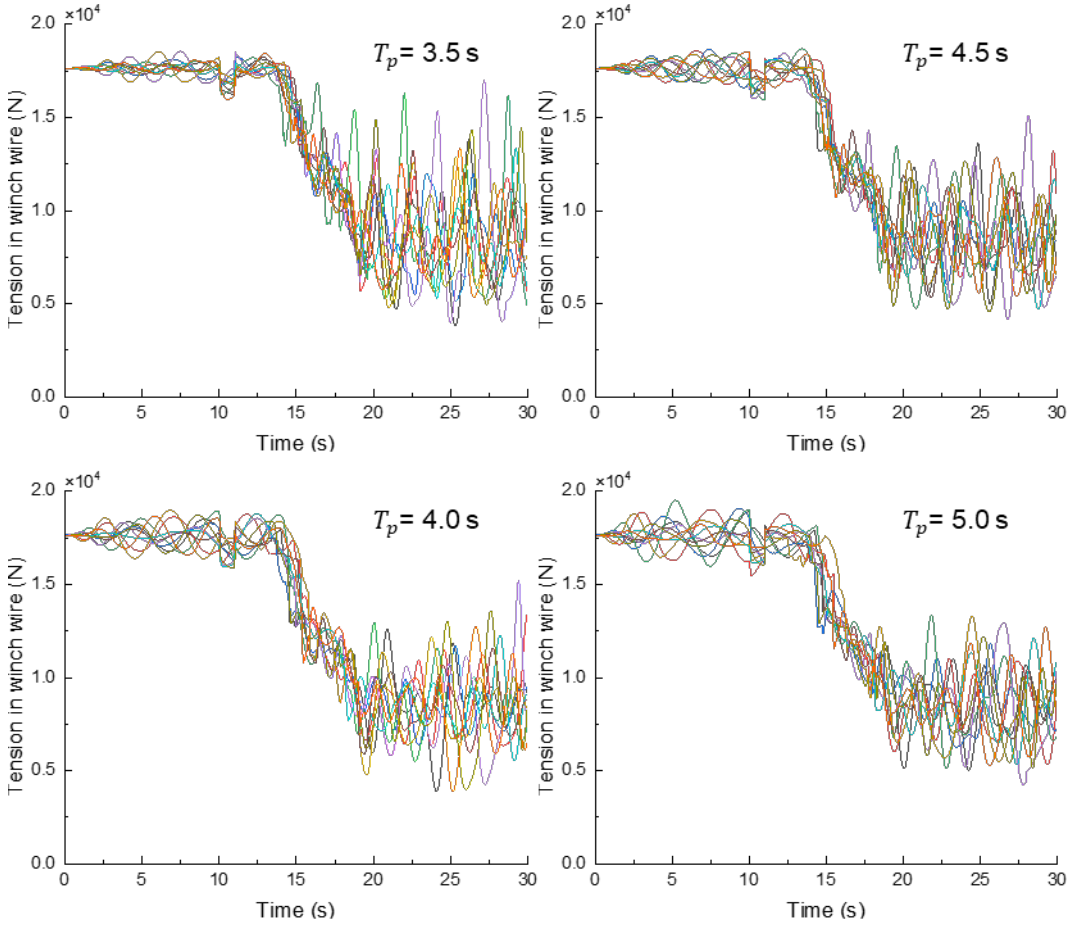


Figure 3.3 Time histories of dynamic tension in winch wire when lowering ROV in different sea states.

In Figure 3.3, each colored line represents the dynamic tension in the winch wire under different wave seeds. The same setting is also applied in Figure 3.4 and Figure 3.5. The results in Table 3.3 show that as the peak period of the ocean wave increases, the average tension and the minimum tension of the rope remain basically stable, but the maximum tension continues to increase. As shown in Figure 3.3, at time 10 s, due to the sudden movement of the crane, there was a brief drop in the tension of the rope and then recovered. At 16 s and 17 s, the bottom of the ROV system had just touched the water surface, and there was a brief increase in cable tension due to the sudden loading caused by the slack umbilical. In the following 18-20 s, the tension of the rope will

increase due to the impact force and quadratic drag. From the time history and statistical data, the sea state will have a loose umbilical phenomenon in the peak range of 15-19 s.

### 3.3 Repeated recovery through wave zone

During the ascent of ROV, the same software program, winch operating speed and the number of simulations were used. However, the ROV was recovered from 25 m below the tip of crane. The ROV will be still for 10 s in the initial position, and then the crane will start. Table 3.4 shows the results of dynamic tension in winch wire in ascent procedure, while Figure 3.4 shows the time histories of dynamic tension in winch wire when recovering ROV in different sea states.

Table 3.4 Stationary analysis of dynamic tension in winch wire when recovering ROV in different sea states.

| Wave peak period (s) | 3.5 | 4.0 | 4.5 | 5.0 |
|---|---|---|---|---|
| Mean tension (N) | 11278.5 | 11269.3 | 11299.5 | 11293.4 |
| Minimum tension (N) | 7267.3 | 6361.6 | 6459.7 | 6225.2 |
| Maximum tension (N) | 18733 | 19212 | 18946 | 18833 |

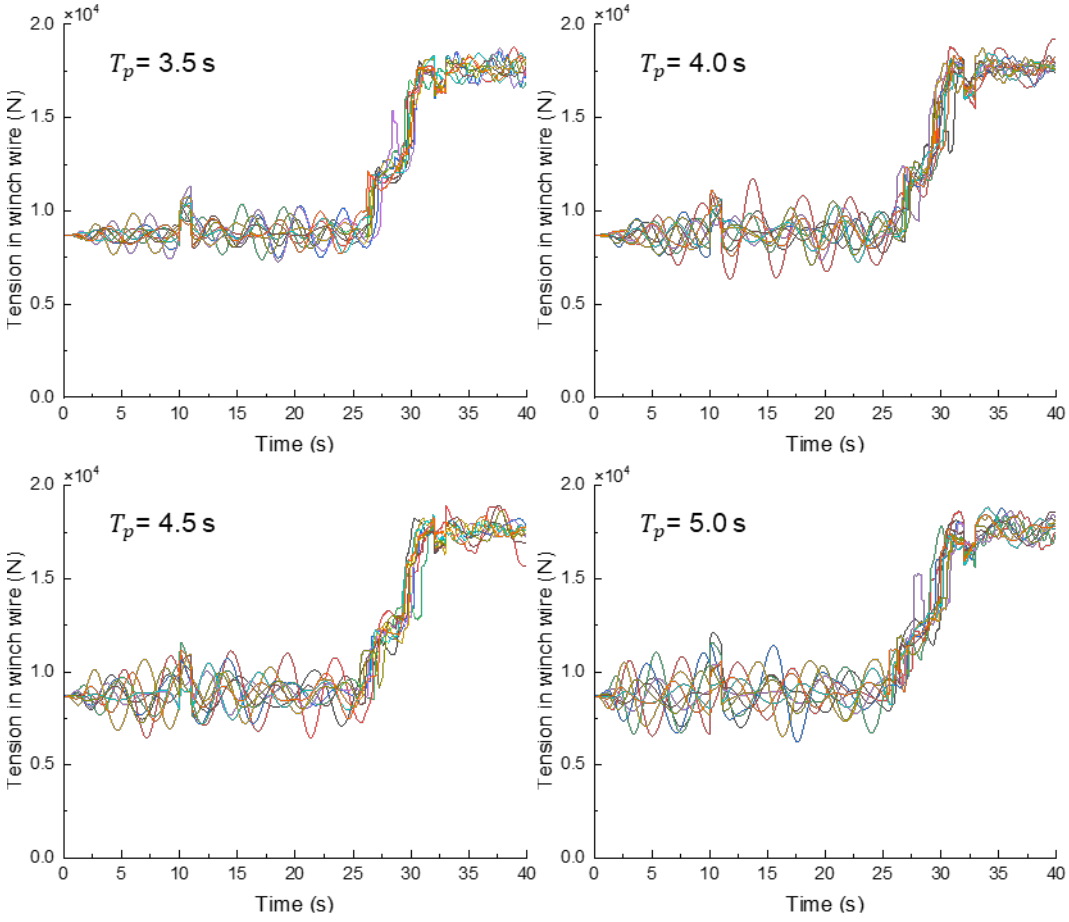


Figure 3.4 Time histories of dynamic tension in winch wire when recovering ROV in different sea states.

It can be seen from Table 3.4 that when the ROV rises, the change of peak period has little effect on the mean and maximum tension of winch wire. As shown in Figure 3.4, there is a sudden increase in the rope tension at 10 s, which is due to the sudden start of the winch. At about 32 s, the crane stopped running suddenly, and there was a sudden decrease in winch wire tension due to the vertical upward inertia of the ROV system. When passing through the wave zone, due to exit forces and quadratic drag, slack of the umbilical occurs at about 26 s, resulting in a significant transient load. However, the winch wire tension may be subjected to greater snap loads during recovery compared to the launch phase of ROV. The maximum and average tensions of winch wire under different conditions during the launch and recovery phases do not experience significant change, but the snap load due to umbilical slack tends to be greater during the ascending phase, indicating that the recovery phase is more critical for the operating conditions investigated.

### 3.4 Investigation of winch speed in launching and recovering ROV

Winch speed is a critical parameter in the launch and recovery process of ROV. Proper control of winch speed ensures the safe deployment of ROV, preventing excessive winch wire movement or slack, thereby avoiding sudden loading and potential damage to the winch wire components. Dynamically adjusting the winch speed according to environmental conditions and support vessel motion can enhance the efficiency of both launch and recovery operations while reducing the risk of operational delays and equipment damage. Since the winch wire typically encounters higher instantaneous loads during the recovery process compared to the launch process (as described in Section 3.3), this section focuses on investigating the impact of winch speed on the dynamic tension in winch wire during the recovery phase. ROV recovery operations were conducted at the significant wave height of 1.0 m and the peak period of 4.5 s, using three common winch speeds of 0.5, 0.7, and 0.9 m/s. Other conditions were consistent with those in the repeated recovery through wave zone described in Section 3.3. The stationary analysis of dynamic tension in winch wire at different winch speeds is presented in Table 3.5, while Figure 3.5 illustrates the time histories of dynamic tension in winch wire under varying winch speeds.

Table 3.5 Stationary analysis of dynamic tension in winch wire at different winch speeds.

| Winch speed (m/s) | 0.5 | 0.7 | 0.9 |
|---|---|---|---|
| Mean tension (N) | 11299.5 | 12398.3 | 13136.4 |
| Minimum tension (N) | 6459.7 | 6854.1 | 6854.1 |
| Maximum tension (N) | 18946 | 19091 | 18957 |

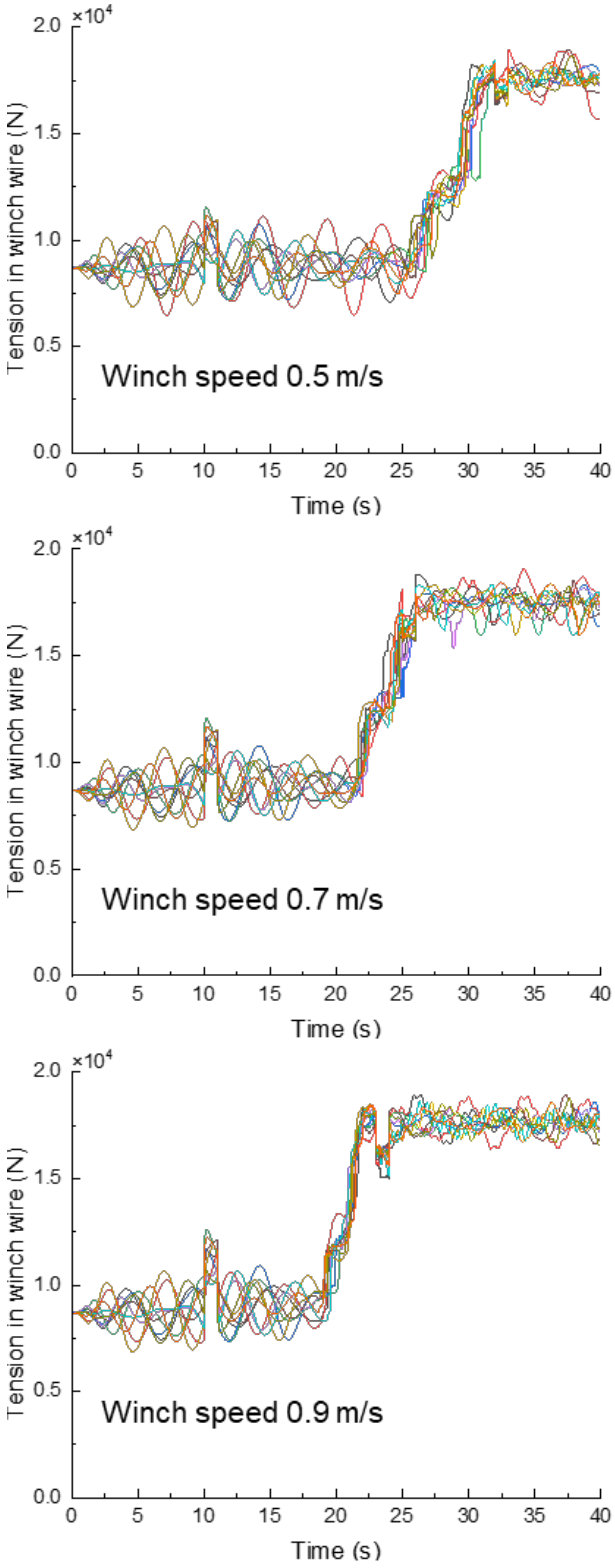


Figure 3.5 Time histories of dynamic tension in winch wire when lowering ROV in different winch speed.

As the winch speed increases, the mean of tension and minimum cable tension of the cable will decrease due to resistance, as shown in Table 3.5. It can be obtained from Figure 3.5 that the change of rope tension at about 10 s and 24 s will increase with the increase of winch speed, which is caused by inertia. However, when ROV travel through wave zones faster at higher winch speeds, the system is exposed to wave forces for less time, which reduces the chance of cable slack. In the case of a certain significant wave height, the winch speed has little effect on the maximum tension at different peak periods, but a lower winch speed can reduce the probability of snap load generation.

## 4 Interaction between floating wind turbine and offshore support vessel

The main purpose of Chapter 4 is to analyze the impact of environmental and operational conditions on the dynamic tension of connecting and mooring lines in a floating wind turbine system. The winch wire is a separate model that connects the crane tip to the top of ROV and it is conceptualized as a simple wire coupling. Two identical mooring lines are modelled as the simple wire couplings used to connect the ship to the wind turbine. The time integration step and time increment are 0.005 s based on the convergence test. The offshore vessel is located approximately 40 m in front of the wind turbine. The same settings are used in Chapters 4, 5, and 6. The numerical simulation model of floating wind turbine and offshore support vessel is shown in Figure 4.1. The simulated sea environment is based on data from the DanTysk wind farm data. DanTysk is a 288-megawatt offshore wind farm located in the North Sea, 70 km west of the island of Sylt. The sea condition data for the DanTysk wind farm were obtained from the StormGeo weather forecast during a routine seabed inspection in 2020. The significant wave height and peak periods of the JONSWAP spectrum for wind wave follow the DNV recommendation (DNV, 2017). The direction differences between the wind wave and wind range from 0° to 30°. The environmental conditions are categorized into low condition (LC), medium condition (MC), and high condition (HC), covering 95% of the wind and wave variability at sea (Ren et al., 2022), as shown in Table 4.1.

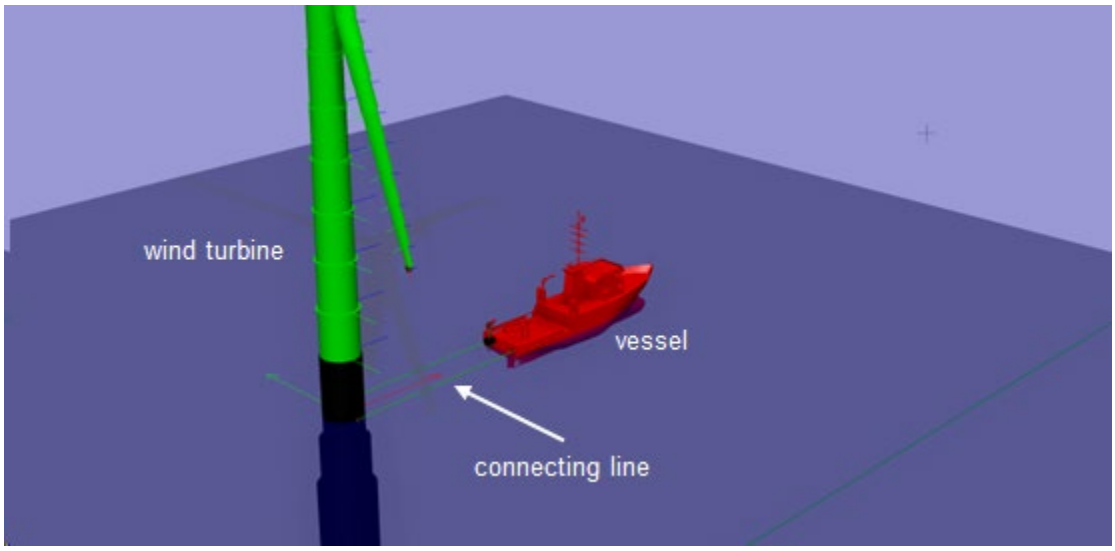

Figure 4.1 The numerical model of floating wind turbine, support vessel and connecting lines in SIMA.

Table 4.1 Environmental data collected from DanTysk weather forecast.

| Environmental condition | | LC | MC | HC |
|---|---|---|---|---|
| Wind | Direction (deg) | 0 - 30 | 0 - 30 | 0 - 30 |
| | Speed (m/s) | 3.4 | 5.4 | 7.9 |
| Wind wave | Direction (deg) | 0 - 30 | 0 - 30 | 0 - 30 |
| | Significant wave height (m) | 0.4 | 0.8 | 1.3 |
| | Peak wave period (s) | 4.5 | 5.5 | 6.5 |
| Swell wave | Direction (deg) | 40 | 40 | 40 |
| | Significant wave height (m) | 0.2 | 0.2 | 0.2 |
| | Peak wave period (s) | 4.5 | 4.5 | 4.5 |
| Current | Direction (deg) | 5 | 5 | 5 |
| | Velocity (m/s) | 0.5 | 0.75 | 0.75 |

## 4.1 Impact of single point mooring system on floating wind turbine

This section examines the impact of SPMS on the safety of mooring lines for floating wind turbine. The relative distance between the FOWT and the OSV is set to 30 m, with the significant wave height increasing from 0.5 m to 1.5 m, while other environmental conditions remain consistent with those in Table 6.1. The numerical model used is shown in Figure 6.1, with the ROV component removed. Figure 4.2 illustrates the maximum and mean tension in mooring lines of FOWT under different sea conditions when the FOWT is present alone. Figure 4.3 shows the maximum and average tension in mooring lines of FOWT under different sea states when connecting to offshore support vessel by SPMS.

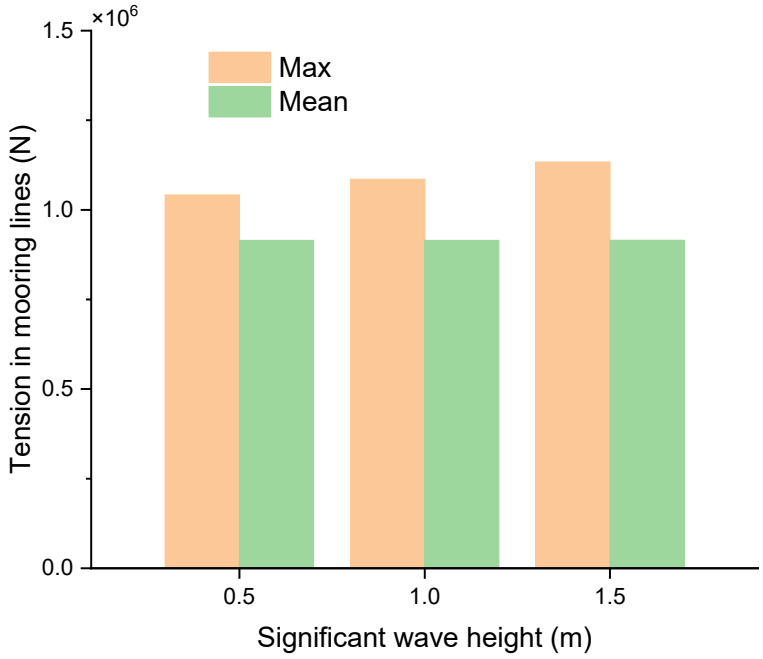


Figure 4.2 Maximum and mean tension in mooring lines of floating wind turbine alone under different sea conditions.

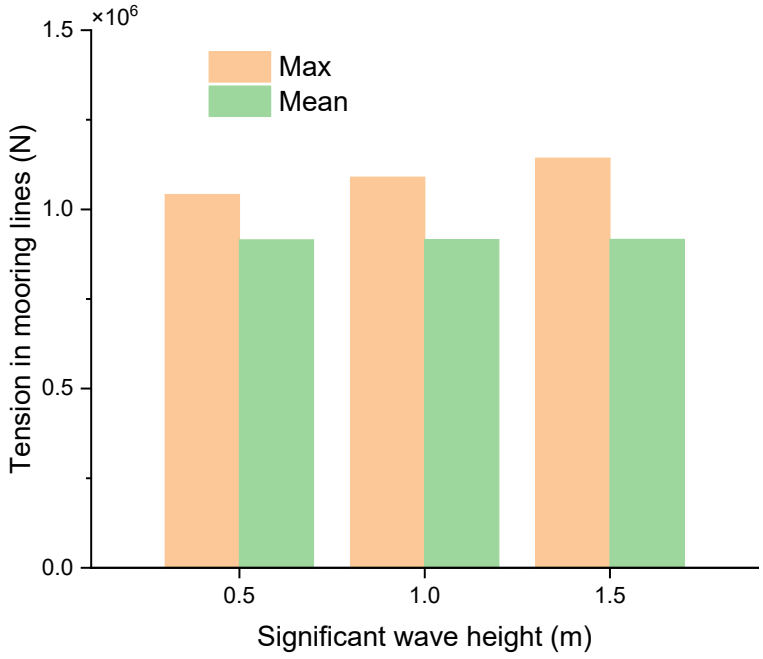


Figure 4.3 Maximum and average tension in mooring lines based on SPMS method under different sea conditions.

Figure 4.2 illustrates the maximum and average tension in mooring lines of floating wind turbine under different significant wave heights. As the significant wave height increases from 0.5 m to 1.5 m, both the maximum and average tensions show an upward trend. The maximum tension increases from approximately $1.05\times10^6$ N to $1.15\times10^6$ N, while the average tension increases from around $0.90\times10^6$ N to $0.95\times10^6$ N. Figure 4.3 depicts the maximum and average tension in the mooring lines under different significant wave heights during ROV operation onboard a small OSV using the SPMS method. Similar to Figure 4.2, both the maximum and average tensions increase as the significant wave height increases. The maximum tension increases from approximately $1.06\times10^6$ N to $1.16\times10^6$ N, while the average tension increases from about $0.91\times10^6$ N to $0.96\times10^6$ N. A comparison of Figure 4.2 and Figure 4.3 shows that the maximum and average tensions in mooring lines increase slightly due to the coupling effect from the OSV positioned by SPMS method, with the increase not exceeding $0.10\times10^6$ N. The overall trend and range of values in both figures are very similar, indicating that the introduction of SPMS method for OSV operation has not significantly altered the dynamic tension experienced by mooring lines of the FOWT. Even at the highest significant wave height of 1.5 m investigated in the present numerical simulation, the increase in dynamic tension due to SPMS method is limited. These small increases can be considered within the safety margin of the mooring system design. Therefore, the SPMS method does not pose a significant impact on the safety of mooring lines for floating wind turbine and can be safely applied in floating wind farm system.

## 4.2 Effect of the relative distance on the tension in connecting and mooring lines

This section discusses the effect of relative distance between floating wind turbine and offshore support vessel on the dynamic tension in connecting and mooring lines. The significant wave height is uniformly set to 0.8 m. Figure 4.4 and Figure 4.5 show the maximum tension and average tension in connecting and mooring lines at different relative distances of 10, 20, 30 and 40 m, respectively.

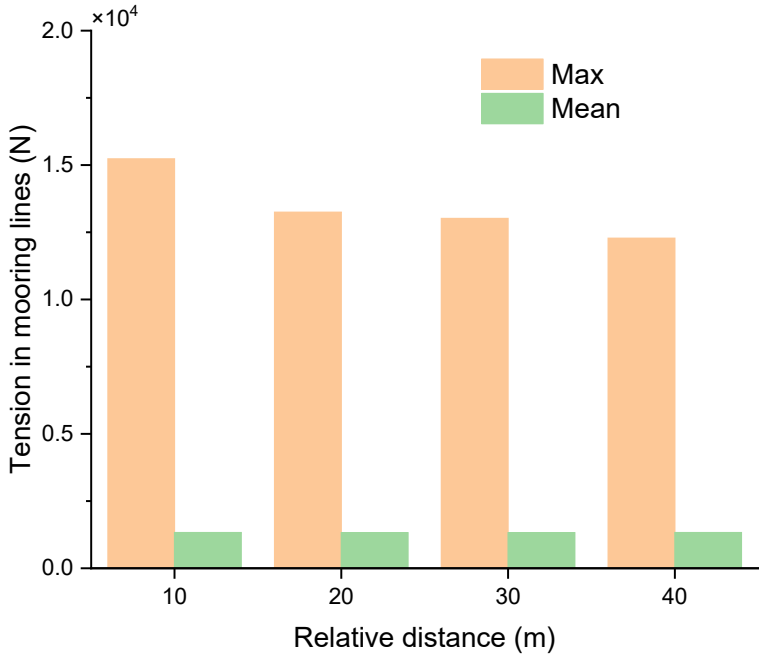


Figure 4.4 Maximum and average tension in connecting lines at different relative distances.

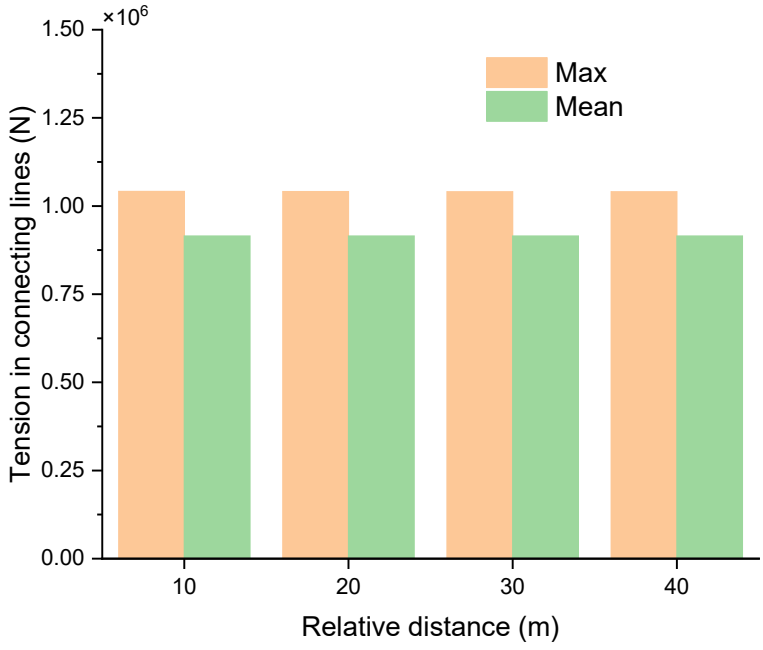


Figure 4.5 Maximum and average tension in mooring lines at different relative distances.

As shown in Figure 4.4, the average tension in connecting lines remains relatively stable at around $0.2\times10^4$ N across different distances. This suggests that under normal operating conditions, the relative distance has minimal impact on the average load of connecting line. However, as the relative distance between floating wind turbine and the offshore support vessel increases, the maximum tension in connecting lines decreases—from approximately $1.50\times10^4$ N at a distance of 10 m to about $1.25\times10^4$ N at 40 m. This decrease occurs because the movement of the offshore support vessel is more restricted at shorter distances, leading to more intense interactions. This phenomenon indicates that increasing relative distance can effectively reduce the maximum tension in connecting line under extreme conditions, potentially enhancing the SPMS system's safety and reliability. As shown in Figure 4.5, the maximum and average tension in mooring line remain approximately $1.04\times10^6$ N and $0.91\times10^6$ N, respectively, as the relative distance increases. This indicates that variations in relative distance have little effect on the tension in mooring lines. The relative distance between the offshore support vessel and the floating wind turbine significantly affects the tension in the connecting lines of the SPMS. As the relative distance increases, the maximum tension in the connecting lines exhibits a clear downward trend, while the average tension remains relatively stable. This indicates that increasing the relative distance can effectively reduce the maximum tension the connecting lines experienced under extreme sea conditions, thereby enhancing system safety.

### 4.3 Tension in connecting and mooring lines under different wave heights

This section examines the tension in connecting lines and mooring lines under various wave height conditions, with the distance between floating wind turbine and the OSV set at 10 m. Because the operational limit of the ROV in this study is 1.5 m, the maximum significant wave height considered is 1.5 m. Figure 4.6 and Figure 4.7 illustrate the variations in maximum and average tension of connecting and mooring lines under significant wave heights of 0.5, 1.0, and 1.5 m, respectively.

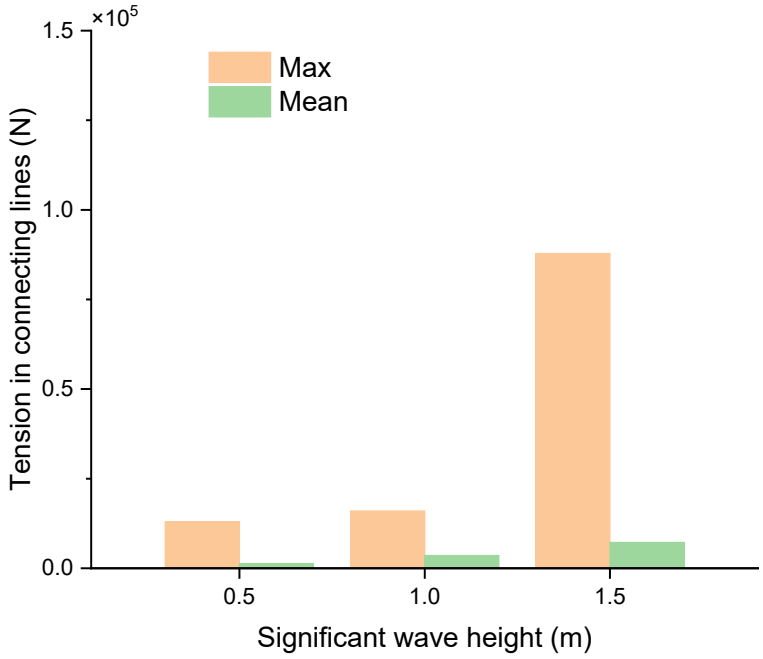


Figure 4.6 Maximum and average tension of connecting line under different sea conditions.

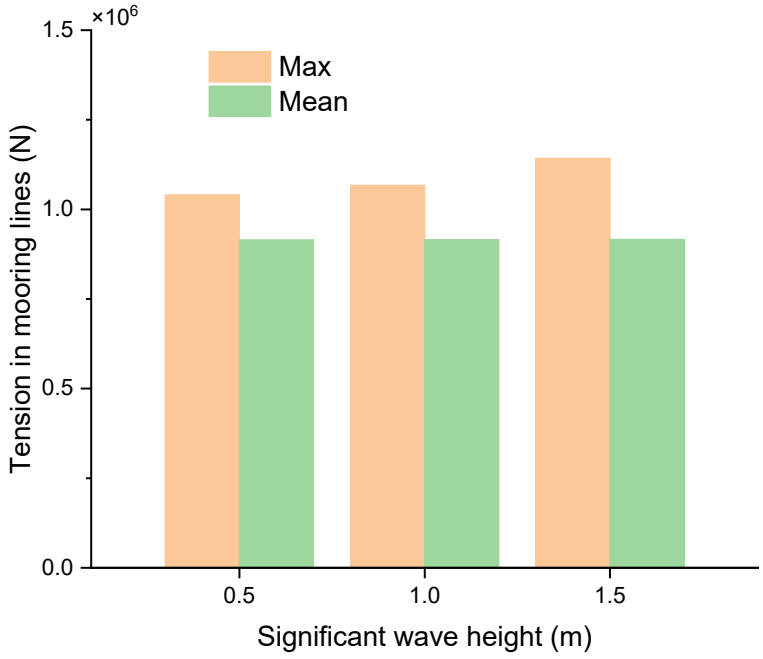


Figure 4.7 Maximum and average tension of mooring lines under different sea conditions.

The maximum and mean tension of connecting lines under different sea conditions, as shown in Figure 4.6, exhibit distinct characteristics. As the significant wave height increases from 0.5 m to 1.5 m, the maximum tension in connecting lines shows a pronounced nonlinear increase. At the significant wave height of 1.5 meters, the maximum tension reaches approximately $0.9\times10^5$ N, which is significantly higher than the levels observed at the significant wave height of 0.5 m and 1.0 m. In contrast, the mean tension in connecting lines increases more moderately, increasing from $0.1\times10^5$ N (0.5 m) to $0.7\times10^5$ N (1.5 m). Figure 4.7 illustrates that the maximum tension in mooring lines increases slightly with the increase in significant wave height, from $1.0\times10^5$ N (0.5 m) to $1.1\times10^5$ N (1.5 m). However, the mean tension in mooring lines remains stable at around $0.91\times10^5$ N. Overall, as the significant wave height increases, the maximum tension in connecting lines shows a significant nonlinear increase, while the maximum tension in mooring lines changes more gradually. This suggests that the connecting lines are more sensitive to changes in sea conditions and may experience substantial increases in maximum tension, particularly under extreme conditions.

### 4.4 Tension in connection line under different wind and wave conditions

In this section, three conditions outlined in Table 6.1 are considered to study the motion characteristics of an offshore support vessel connected to a wind turbine during ROV operation. The angle difference between the wind and wave directions is varied from 0° to 30°. The distance between the center of floating wind turbine and the original position of vessel is set at 30 m. The environmental conditions gradually increase from low (LC) to high (HC), with corresponding increases in wave height, wind speed, and current velocity. Figure 4.8 shows the maximum and average tension in connecting lines under different environmental conditions when the wind and wave directions are aligned at 0°. Figure 4.9 illustrates the maximum and average tension in connecting lines under different conditions when the wind and wave directions differ by 30°.

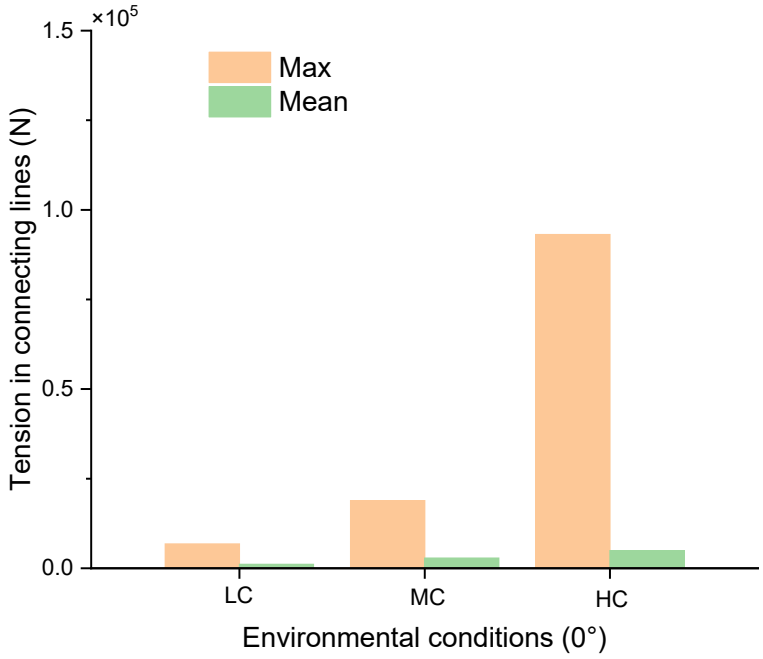


Figure 4.8 Maximum and average tension of connecting line under 0 misalignment angle between wind and wave directions.

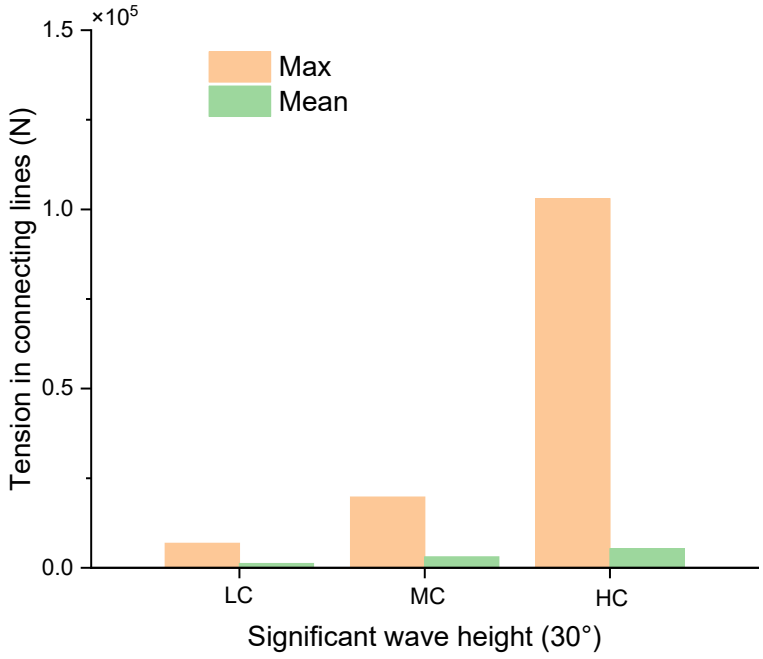


Figure 4.9 Maximum and average tension of connecting line under a 30-degree misalignment angle between wind and wave directions.

Figure 4.8 and Figure 4.9 indicate that as the environmental conditions intensify from low (LC) to high (HC), both the maximum and average tension in connecting lines increase significantly. Under low conditions, the maximum and average tensions are relatively low, while under high conditions, the maximum tension reaches its peak. In all environmental conditions with a 30° angle (Figure 4.9), both the maximum and average tensions are slightly higher than in the 0° scenario (Figure 4.8). A comparison of the two figures reveals that the angle has a minimal impact on the tension in the connecting lines. This suggests that while wind and wave angles do have some effect on the tension, the overall trend is that the more severe the environmental conditions, the greater the tension in connecting lines. The directions of wind and waves also play a crucial role in affecting the tension of the connecting lines. When the relative distance between the offshore maintenance vessel and the floating wind turbine is short, complex hydrodynamic interactions between the two can lead to a sharp, nonlinear increase in the tension of the connecting lines.

## 5 Small OSV operation capability for subsea inspection of fixed wind turbines

The purpose of Chapter 5 is to optimize deployment strategies by evaluating the effects of deployment position, winch speed, and environmental conditions on wire tension. The study establishes a safe operating envelope by identifying critical limits for safe ROV deployment under different sea states. The wind turbine has been simplified to a simple cylinder and is simulated as a fixed mass body point. The winch wire is a separate model that connects the crane tip to the top of ROV and it is conceptualized as a simple wire coupling. Two identical mooring lines are modelled as the simple wire couplings used to connect the ship to the wind turbine. The offshore vessel is located approximately 40 m in front of the wind turbine. The winch that extends and shortens the wire is represented by a crane tip located 5.0 m above the free water surface. The ROV top is connected to the winch by a wire and is located 0.7 m below the position of crane tip. The ROV will be lowered to a depth of 20.0 m below the free surface at the set winch speed after the winch is started, and then the ROV will be lifted out of the water to its initial position at the same speed after the winch stops for a period of time representing the underwater work. The numerical simulation model of launching and recovering ROV is shown in Figure 5.1. The data of sea conditions for the DanTysk wind farm are derived from the 2020 StormGeo weather forecast during regular seabed inspection, as shown in Table 5.1.

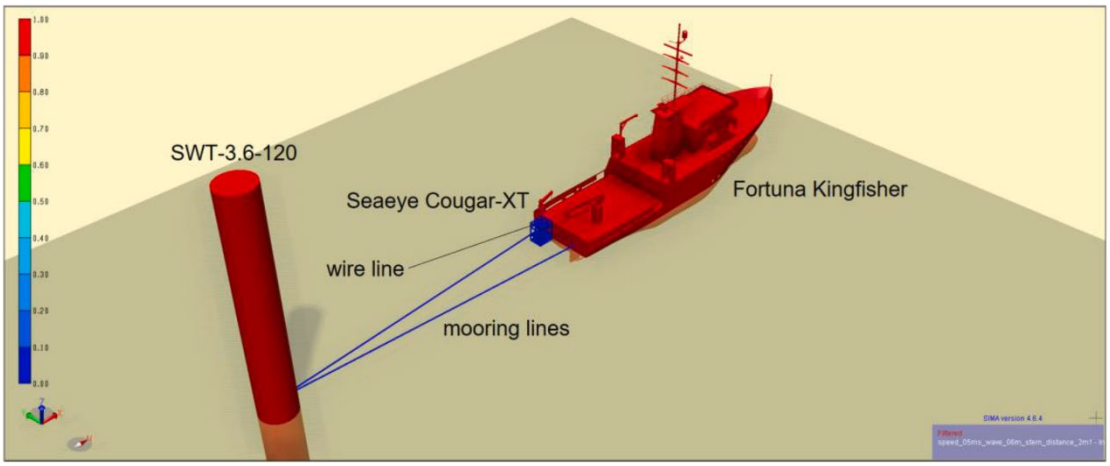


Figure 5.1 The coupled numerical model of fixed wind turbine, support vessel and ROV model in SIMA.

Table 5.1 Environmental data collected from weather forecast for the offshore operation.

| Sea conditions | Properties | Values |
|---|---|---|
| Wind wave | Direction (deg) | 330/SW |
| | Significant wave height (m) | 0.5 - 1.25 |
| | Peak periods (s) | 3.0 – 5.0 |
| Swell wave | Direction (deg) | 40/SE |
| | Significant wave height (m) | 0.2 |
| | Peak periods (s) | 4.5 |
| Wind | Direction (deg) | 330/SW |
| | Velocity (m/s) | 5.4 |
| Current | Direction (deg) | 305/SW |
| | Velocity (m/s) | 0.07 - 0.14 |

## 5.1 Effect of deployment position

The deployment position of ROV is situated either at the vessel side or stern, ensuring a specific horizontal distance from the hull. The minimum horizontal distance is typically set at half the ROV's length to prevent collisions during operational maneuverers, while the maximum distance from the hull is constrained by the crane boom's length. In this study, the launch location of ROV is positioned centrally between two mooring lines at the vessel stern. However, deployment on the ship side is sometimes necessary due to obstructions from mooring lines. The crane arm can extend up to a maximum distance of 4.0 m for the ROV operated onboard a small OSV. Figure 5.2 shows the time history of wire tension at three horizontal distances from the vessel stern at a significant wave height 0.6 m and winch speed 0.5 m/s. Figure 5.3 shows the simulation results of ROV being deployed on the ship side with different distance from the hull.

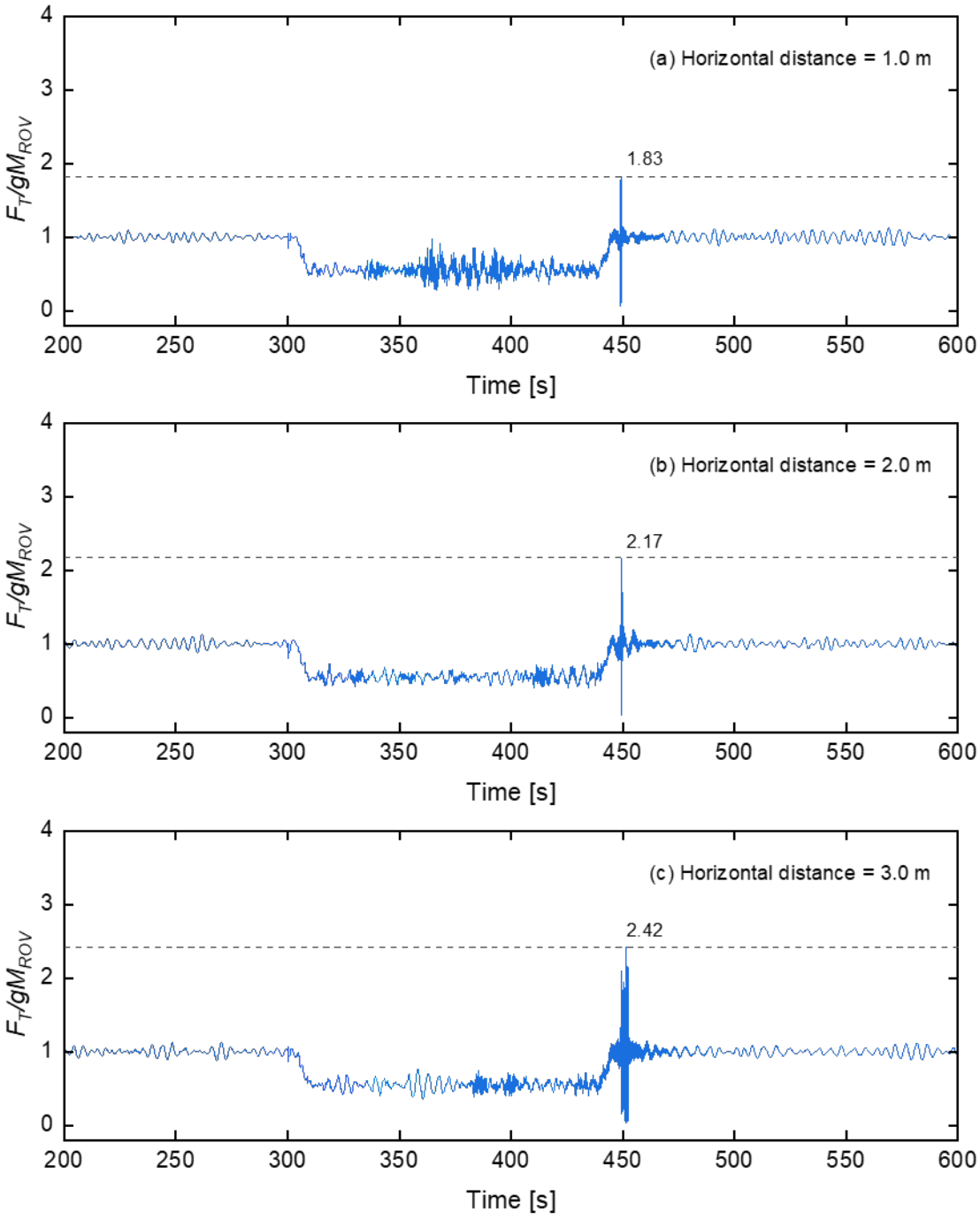


Figure 5.2 Time history of wire tension during ROV deployment from the vessel stern at horizontal distances of 1.0 m (a), 2.0 m (b), and 3.0 m (c).

The peak wire tension is observed when the crane halts during the recovery phase for the ROV being deployed at vessel stern, as illustrated in Figure 5.2. This peak is due to the abrupt cessation of winch speed, leading to transient fluctuations in wire tension. These fluctuations are seen gradually subside over time. The maximum wire tension

during the recovery phase is approximately 2.4 times higher than that during the launch phase for the same horizontal distance in Figure 5.2(c). While the increase in horizontal distance marginally affects wire tension during the launch phase, its impact on the maximum wire tension during the recovery phase is evidently more significant. This can be attributed to the fact that the horizontal distance acts as a radius of gyration, amplifying the ROV's movement and momentum with increased distance, especially under the vessel heave acceleration and water particle movements. Therefore, opting for a deployment position with a shorter horizontal distance is advantageous while ensuring the safety of the equipment by minimizing collision risks.

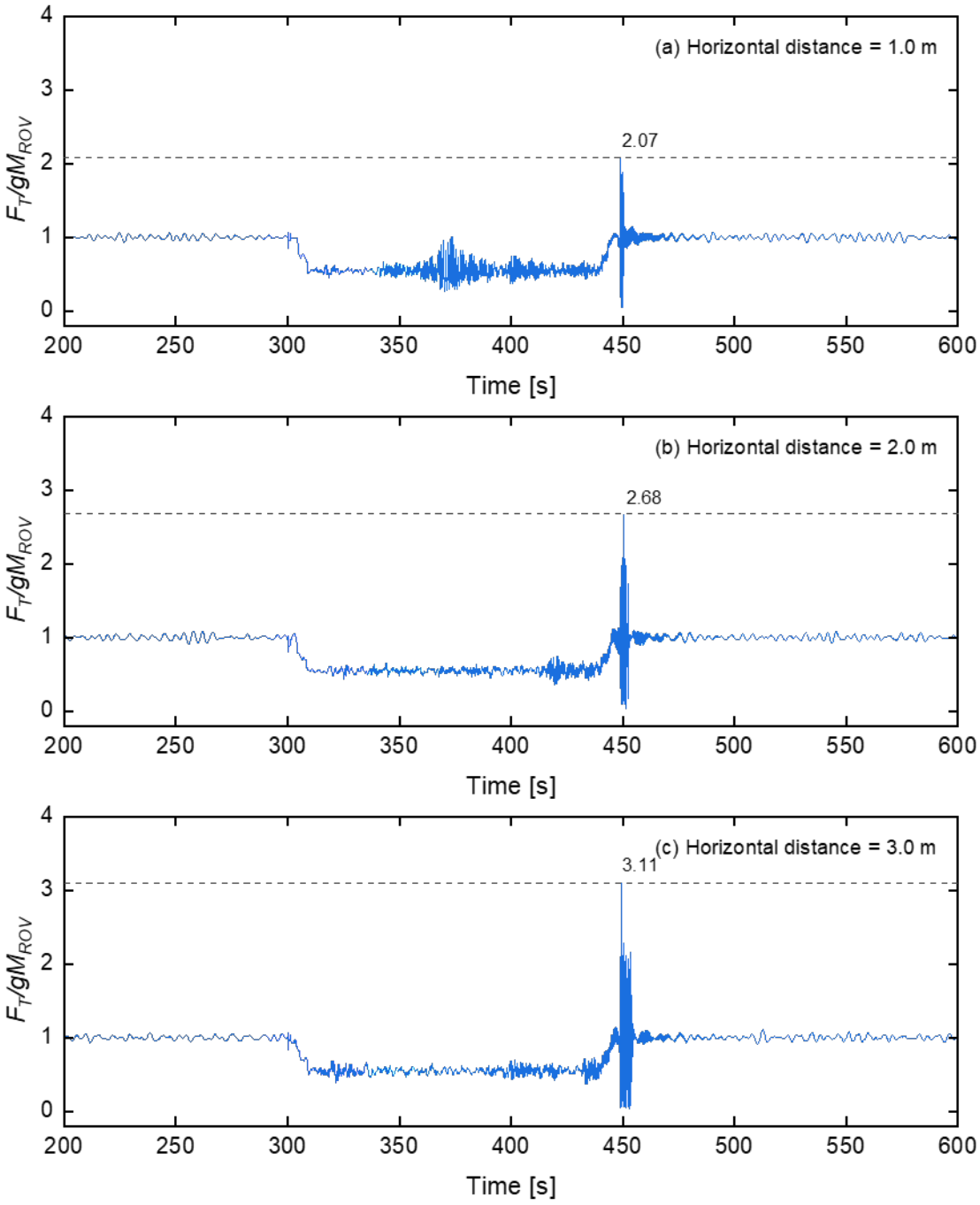


Figure 5.3 Time history of wire tension during ROV deployment from vessel side at horizontal distances of 1.0 m (a), 2.0 m (b), and 3.0 m (c).

Similar to the observations with stern deployment, Figure 5.3 indicates that snap loads occur when winch speed is abruptly halted during the recovery phase for ROV deployment from vessel side. In the descending phase, wire tension remains relatively stable; however, it evidently escalates with increased horizontal distance during the ascending phase. In Figure 5.2(c), the maximum wire tension is approximately 3.0

times the weight of ROV. As shown in Figure 5.3(c), it reaches about 3.1 times. Therefore, deploying the ROV from the side of the ship results in slightly higher wire tension than deploying it from the stern at the same horizontal distance, as depicted in Figure 5.2(c). This is attributed to the waves coming from the stern direction exerting less impact on the movement of the transverse radius of gyration.

### 5.2 Influence of winch speed

Optimizing winch speed selection is often a mean for minimizing sudden load occurrences during ROV operations. In a scenario where the ROV is deployed 2.0 m horizontally from the ship hull and other conditions are the same as in Figure 5.3, numerical simulations were performed using three field-standard winch speeds appropriate for the small OSV in the case study. The results, showcasing the time history of wire tension, is illustrated in Figure 5.4.

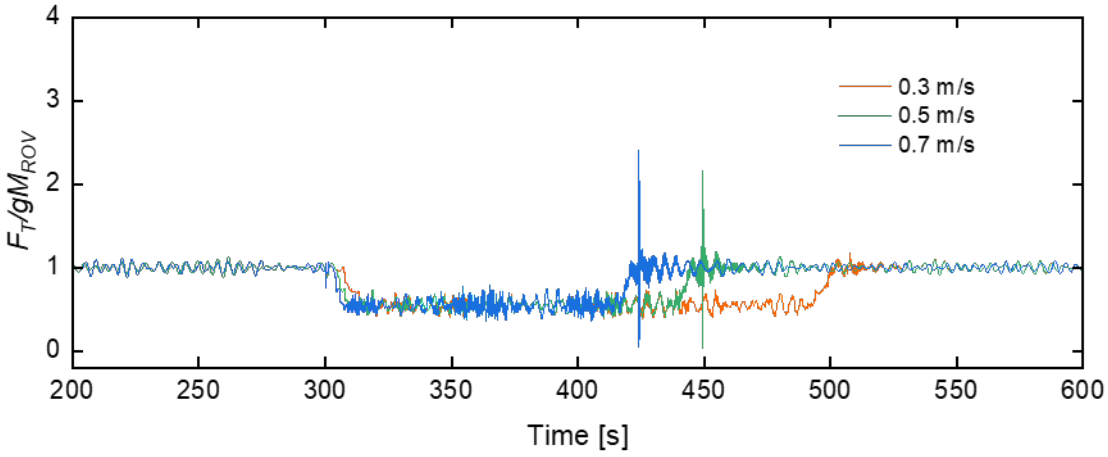


Figure 5.4 Time history of wire tension for ROV deployment 2.0 m from vessel stern at three different winch speeds.

Due to identical winch start time and total travelling distance, the stop time of ROV varies with each speed, as presented in Figure 5.4. The instantaneous wire tension escalates evidently during the recovery phase, as ROV moving at higher speeds exhibit increased inertia and acceleration. While higher winch speed is advantageous for descending the ROV, thereby shortening operation times, they have little effect on maximum wire tension during the launch phase. Conversely, adopting a lower winch

speed of 0.3 m/s, as opposed to the conventional 0.5 m/s, for ascending phases significantly reduces maximum wire tension from approximately 2.1 to 1.1 times respectively for the case demonstrated in Figure 5.4, enhancing operational safety.

### 5.3 Environmental limit of ROV operation

According to consultations with onboard operator of the OSV used in the case study, the current operational limit for ROV deployment in field operation is defined by a significant wave height of 1.0 m which was very much based on the operator's experience. To demonstrate the appropriateness of the current practice, as the first step, this study considers two significant wave heights, 0.75 m and 1.0 m, to reflect the existing operational threshold. The new procedure for ROV launch and recovery involves reductions in winch speed and horizontal distance, as detailed in Table 5.2. Figure 5.5 illustrates a comparison of wire tension under traditional field operational conditions and the new procedure based on the present numerical simulations.

Table 5.2 The deployment strategies in traditional field production and the new procedure.

| | Field production | New procedure |
|---|---|---|
| Environmental limit (m) | 0.75, 1.0 | 0.75, 1.0 |
| Deployment position | stern | stern |
| Horizontal distance (m) | 2.0 | 1.0 |
| Winch speed (m/s) | 0.5 | 0.3 |

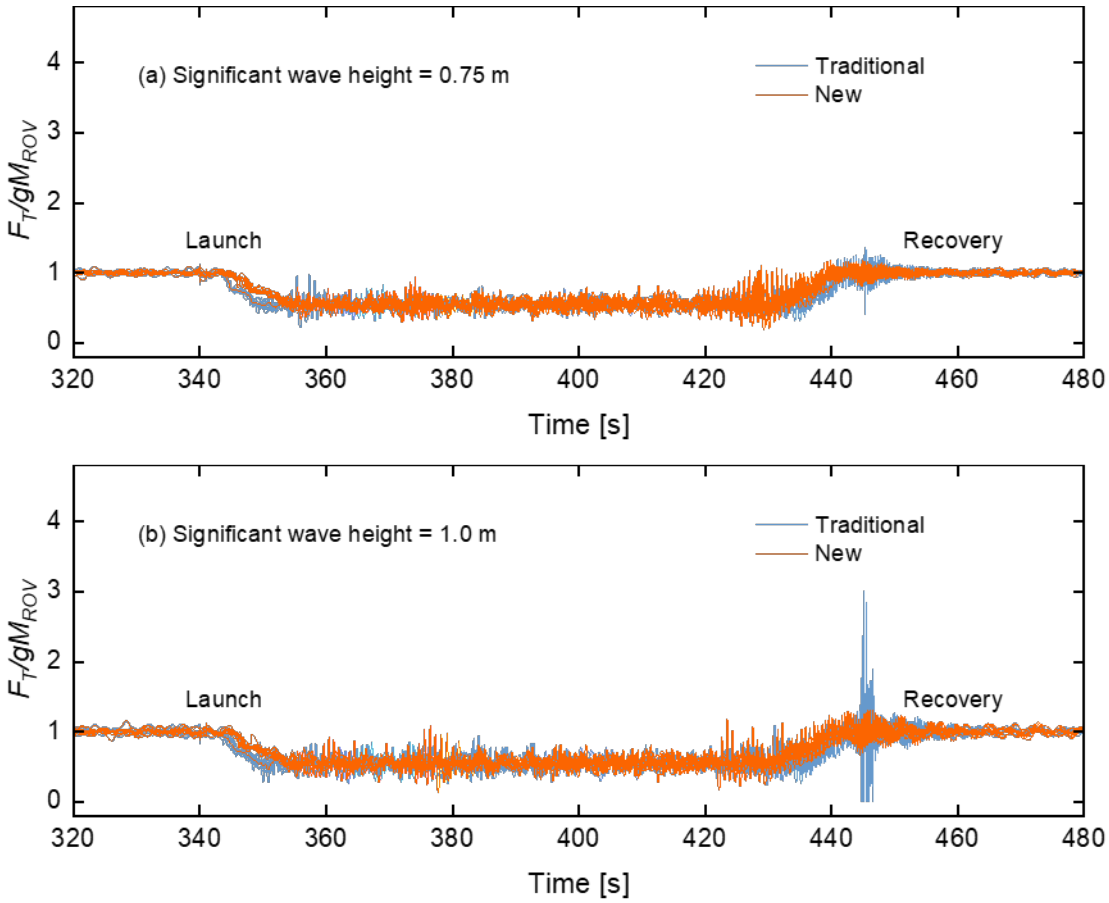


Figure 5.5 Comparison of time history of wire tension between traditional and new strategies under environmental limits when ROV deployment from vessel stern.

The maximum wire tension under the new procedure decreases slightly at a significant wave height of 0.75 m as shown in Figure 5.5(a). However, under the significant wave height of 1.0 m, as shown in Figure 5.5(b), the maximum wire tension during recovery phase under the new strategies is approximately one-third of that in traditional field production, equivalent to a reduction of about 2.0 times the ROV's weight. This substantial decrease in maximum wire tension underscores the effectiveness of the new procedure in enhancing both equipment and operational safety. It is worth pointing out that the rated break strength of winch wire, approximately 1.8 times the weight of ROV as listed in Table 2.8, is exceeded by the maximum wire tension under traditional field operation strategies. However, the new procedure maintains maximum wire tension within safe limits under a significant wave height of 1.0 m, as evidenced in Figure 5.5. To identify potential expansions of the ROV operational limit, the significant wave height is further increased, with findings presented in Figure 5.6.

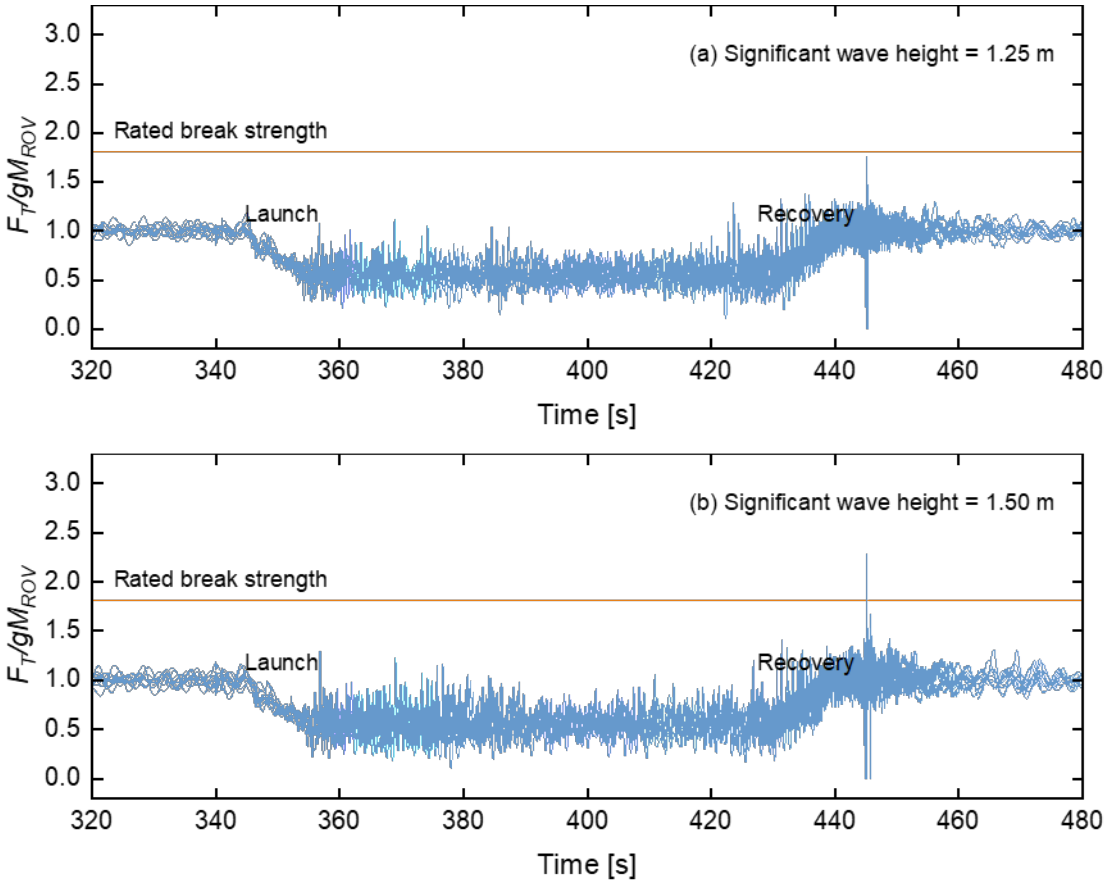


Figure 5.6 The environmental limit for ROV operation under new strategies when deployment from vessel stern.

Under a significant wave height of 1.25 m, the maximum wire tension approaches but does not surpass the rated break strength of winch wire as shown in Figure 5.6(a). However, this threshold is exceeded at a significant wave height of 1.50 m, as shown in Figure 5.6(b). Consequently, the new procedure potentially elevates the operational limit for ROV deployment in field operation to a significant wave height of 1.25 m.

### 5.4 Expansion of operational capacity

In contrast to the empirical approach of the current field operation at sea entirely based on the operator's experience, the present study aimed to provide informed recommendation based on rigorous numerical and experimental analysis. Expanding operational capacity through improved ROV deployment strategies is further examined

based on comprehensive numerical simulation. Figure 5.7 presents the statistics of significant wave heights at the DanTysk wind farm in May 2020 (31 days), sourced from StormGeo weather forecasts. As mentioned above, the operational limit is 1.0 m using the traditional methods, denoted as Trad, whereas the operational limit is 1.25 m under the new strategy, denoted as New. Under the conventional ROV launch and recovery procedures, 27 days (87.1%, 0-1.0 m significant wave height) per month typically align with the criteria for safe operations. However, with the implementation of the new safety guidelines developed in the present study for ROV operation, an additional two operating windows (6.5%, 1.25 m significant wave height) per month are anticipated. Assuming this month is representative while acknowledging the variation throughout different seasons of a year, the annual increase in operational windows is estimated to be approximately 6.5%.

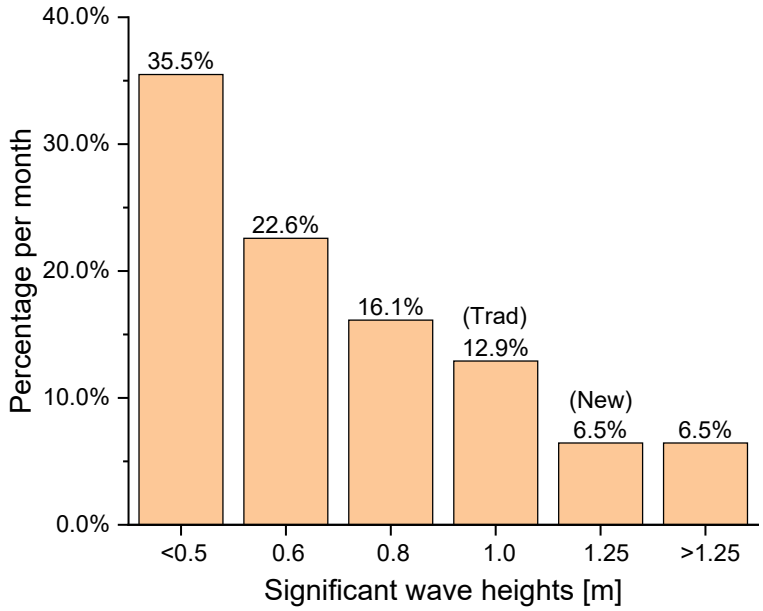


Figure 5.7 The statistics of significant wave heights at the DanTysk wind farm from StormGeo weather forecast.

### 5.5 Safe operating envelope

As a new development of the present study, the safe operating envelope of ROV deployment onboard a small OSV in the new procedure is defined as: 1) the maximum tension in winch wire does not exceed its rated break strength and 2) the maximum

tension in mooring lines does not exceed the rated break strength of the mooring line material. Given the variability of surface wave conditions, which can differ at any given moment or location even within the same significant wave height and peak period due to the stochastic nature of wave patterns, the present numerical simulations are carried out for 10 operating cycles for each wave condition using different wave seeds. This approach was taken to achieve statistical reliability and an accurate assessment of wire tension. The outcomes of these simulations are depicted in Figure 5.8.

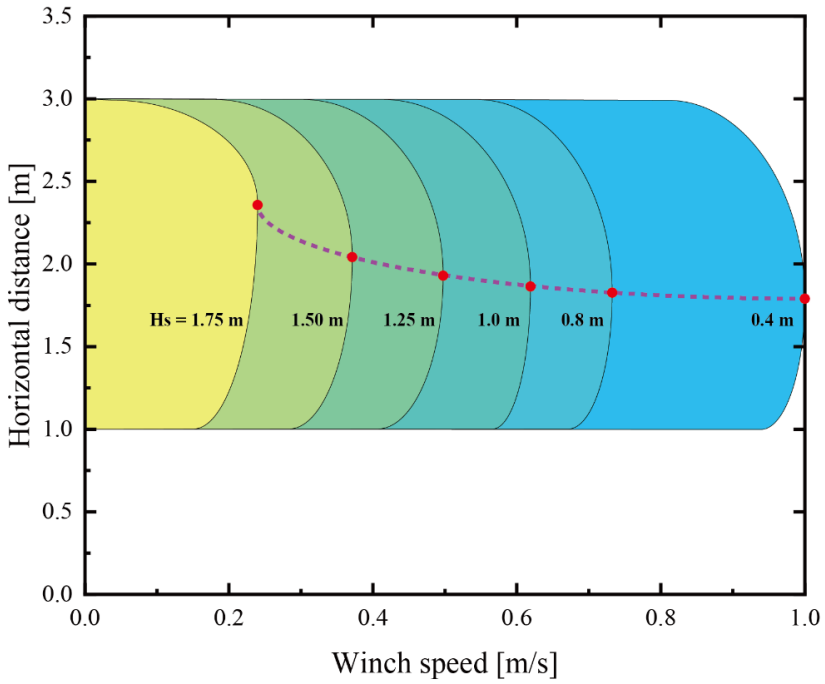


Figure 5.8 Safe operating envelope of ROV deployment from vessel stern under three primary environmental and operational parameters: significant wave height, winch speed, horizontal distance of ROV to the vessel hull.

The maximum horizontal distance 3.0 m is based on the limit of crane boom length of the OSV, Fortuna Kingfisher for the present case study, and the minimum is 1.0 m to ensure that the ROV avoids collision with the vessel hull during the operation. The winch speed is typically less than 1.0 m/s to avoid the excessive impact on winch wire as described previously. The critical curve (dotted line) that satisfies the definition of safe operating envelope of ROV deployment on vessel stern at maximum winch speed is shown in Figure 5.8. The curves corresponding to each significant wave height represent the combined critical values for safe ROV deployment. The significant wave

height of 1.75 m is considered the most extreme sea state for the small OSV in the present study, while Figure 5.8 shows that it is safe for ROV deployment across the whole range of the winch speed up to 1.0 m/s and the horizontal distance between 1m to 3m under the significant wave height less than 0.4 m. The dashed line intercepts with the curve of a significant wave height of 0.4 m representing the condition under which a maximum winch speed of 1.0 m/s can be used. The area enclosed by the curve represents the range of horizontal distance and winch speed under which the ROV can be safely operated under the sea state with the significant wave height. As environmental conditions become more severe with increased significant wave height, the enclosed area of the curve is markedly reduced indicating considerable restriction for safe operation towards lower winch speed with the set horizontal distance. The maximum winch speed can be safely operated for each given sea state is seen initially increases and then decreases as the deployment position of ROV gradually moves away from the vessel hull. The critical values shown as red dot points in Figure 5.8 reveal a combination of the maximum winch speed can be safely operated with the corresponding horizontal distance under the given sea state (significant wave height). The dotted curve in purple is formed by connecting the critical points in each sea state, representing the maximum winch speed the ROV can be safely operated at the horizontal distance under the given sea state. Figure 5.8 provides simple and straightforward guidance for onboard safe ROV operation crucial for the small OSV currently operating widely for offshore wind farms O&M in European waters. This is a significant step forward in improving the ROV safe operation from empirical onboard staff experience-based towards science/technology-based practice. The chart can also be used for future potential capability extension of the OSV operation.

## 6 ROV deployment onboard a small OSV coupled with a floating wind turbine

The main goal of Chapter 6 is to assess how environmental factors, relative distance, and wind-wave misalignment affect the dynamics of mooring and connecting lines during ROV deployment on a floating wind turbine. It also compares the performance of floating and fixed wind turbines to highlight differences in tension, providing insights for optimizing offshore wind turbine operations and ensuring safe ROV inspections and maintenance. The numerical model in Chapter 6 is shown in Figure 6.1, with the specific settings for each section explained in the corresponding sections. The numerical simulation environment has been introduced in Chapter 4, as shown in Table 6.1.

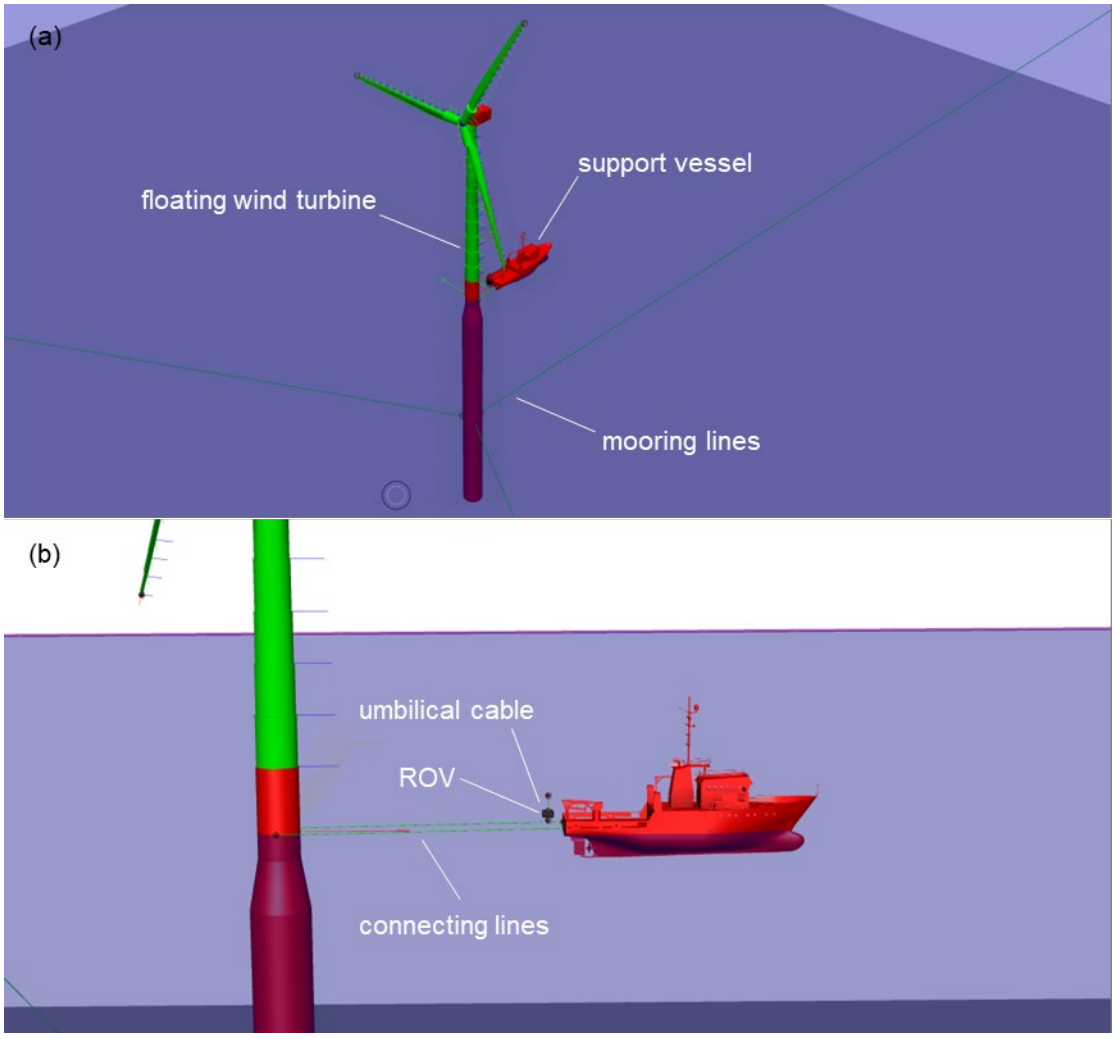


Figure 6.1 Diagonal view (a) and side view (b) of the coupled numerical model of floating wind turbine, support vessel and ROV model in SIMA.

Table 6.1 Environmental data collected from DanTysk weather forecast.

| Environmental condition | | LC | MC | HC |
|---|---|---|---|---|
| Wind | Direction (deg) | 0 - 30 | 0 - 30 | 0 - 30 |
| | Speed (m/s) | 3.4 | 5.4 | 7.9 |
| Wind wave | Direction (deg) | 0 - 30 | 0 - 30 | 0 - 30 |
| | Significant wave height (m) | 0.4 | 0.8 | 1.3 |
| | Peak wave period (s) | 4.5 | 5.5 | 6.5 |
| Swell wave | Direction (deg) | 40 | 40 | 40 |
| | Significant wave height (m) | 0.2 | 0.2 | 0.2 |
| | Peak wave period (s) | 4.5 | 4.5 | 4.5 |
| Current | Direction (deg) | 5 | 5 | 5 |
| | Velocity (m/s) | 0.5 | 0.75 | 0.75 |

## 6.1 Effect of SPMS and ROV deployment

The presence of SPMS and the deployment of ROV have an impact on the mooring lines of the FOWT. In this study, both wind and wave directions are set to 0°, originating from the vessel stern, with additional conditions detailed in Table 6.1. The initial relative distance between OSV and FOWT is set to 20 m. The ROV is launched from its initial position to 40 m below water surface, remains stationary for 100 s to represent underwater operations, and is then raised back to its initial position. Each numerical simulation runs for three hours to capture sufficient wave and current variations, ensuring reliable and comprehensive data for design and analysis. Figure 6.2 displays the maximum and mean tension in mooring lines of FOWT and connecting lines of SPMS under various sea conditions.

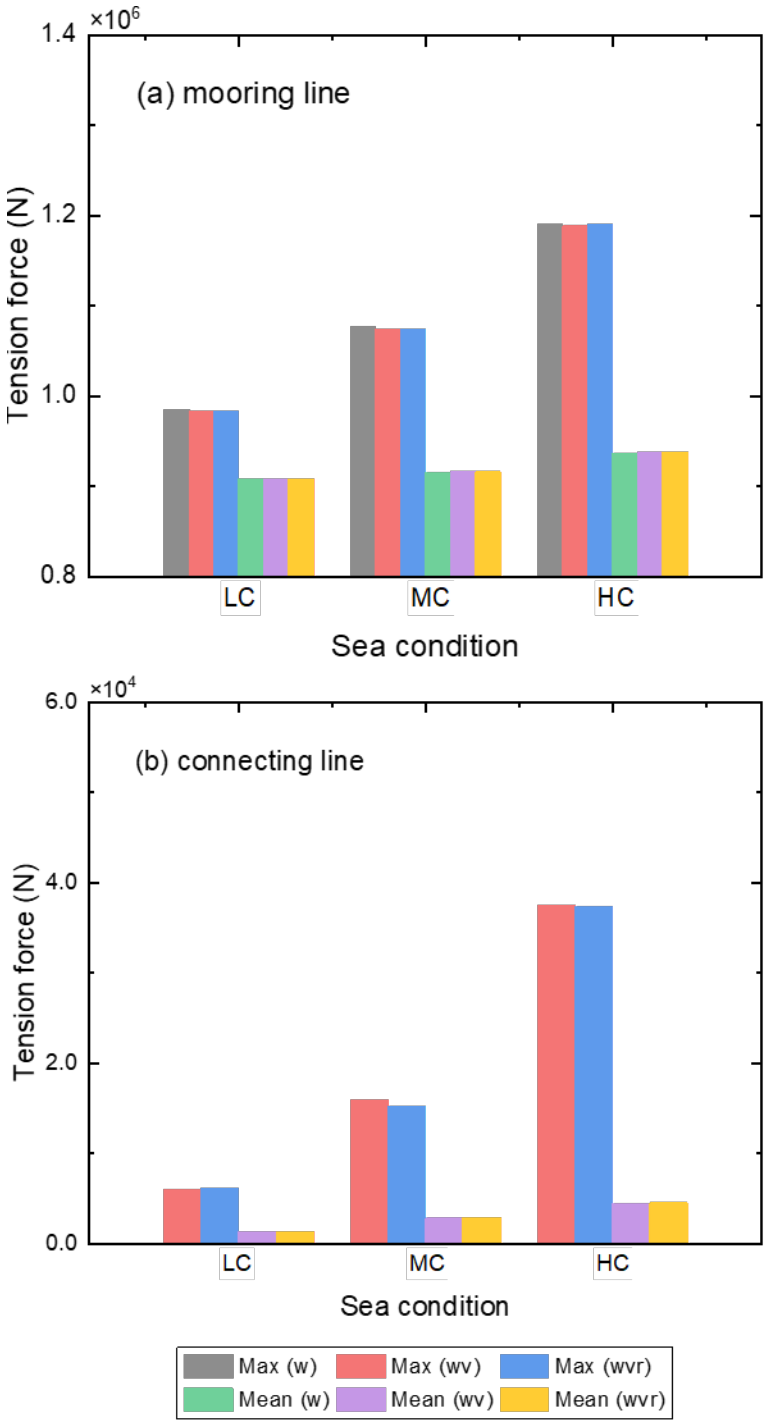


Figure 6.2 The maximum and mean tension in mooring lines of FOWT (a) and connecting lines of SPMS (b) under different sea conditions.

In Figure 6.2, "w" denotes a standalone floating wind turbine, "wv" represents the floating wind turbine connected to the offshore service vessel using SPMS method, and "wvr" signifies the floating wind turbine connected to the offshore service vessel with SPMS method carrying out ROV deployment. The maximum tension in mooring lines

increase progressively from approximately $0.98\times10^6$ N (LC) to $1.20\times10^6$ N (HC) as sea conditions becomes more severe as shown in Figure 6.2(a). Meanwhile, the mean tension in mooring lines also experiences a very slight increase, from approximately $0.92\times10^6$ N (LC) to $0.94\times10^6$ N (HC). However, it is noted that the maximum and mean tension in mooring lines of FOWT remain essentially constant under the same sea conditions. This is due to the minimal motion response of the relatively small offshore service vessel with or without the ROV operating onboard, indicating that the presence of offshore service vessel (wv) and the deployment of ROV (wvr) have minimal impact on the mooring lines of the floating wind turbine.

Though similar trend is observed, there is a striking difference in Figure 6.2(b) that the maximum tension in connecting lines of SPMS increases significantly from about $0.6\times10^4$ N (LC) to $3.7\times10^4$ N (HC) as wave conditions deteriorate. The mean tension in connecting lines of SPMS shows a similar trend of increase from approximately $0.1\times10^4$ N (LC) to $0.5\times10^4$ N (HC). Both the maximum and the mean tension in connecting lines of SPMS remain essentially constant under the same sea conditions, indicating that the deployment of ROV has a negligible impact on the dynamics of connecting lines of SPMS. Therefore, by employing SPMS with sufficient connecting lines, it is a clear demonstration that the SPMS method for ROV-based inspection and maintenance operations on floating wind turbine exhibits a satisfactory level of safety.

## 6.2 Effect of relative distance on line dynamics

The effect of relative distance between offshore support vessel and floating wind turbine on the maximum and mean tension in umbilical cable, connecting lines and mooring lines is of paramount importance for the safe operation of ROV on board during O&M. Insufficient relative distance can lead to collisions, whereas excessive distance can complicate ROV operations. Constrained by the length of umbilical cable, the initial relative distances are set to 10, 20, 30 and 40 m, covering the majority of operational scenarios for this type of offshore service vessel. Other detailed environmental conditions are listed in Table 6.1. The maximum and mean tension in umbilical cable, connecting lines and mooring lines under different relative distances are presented in Figure 6.3.

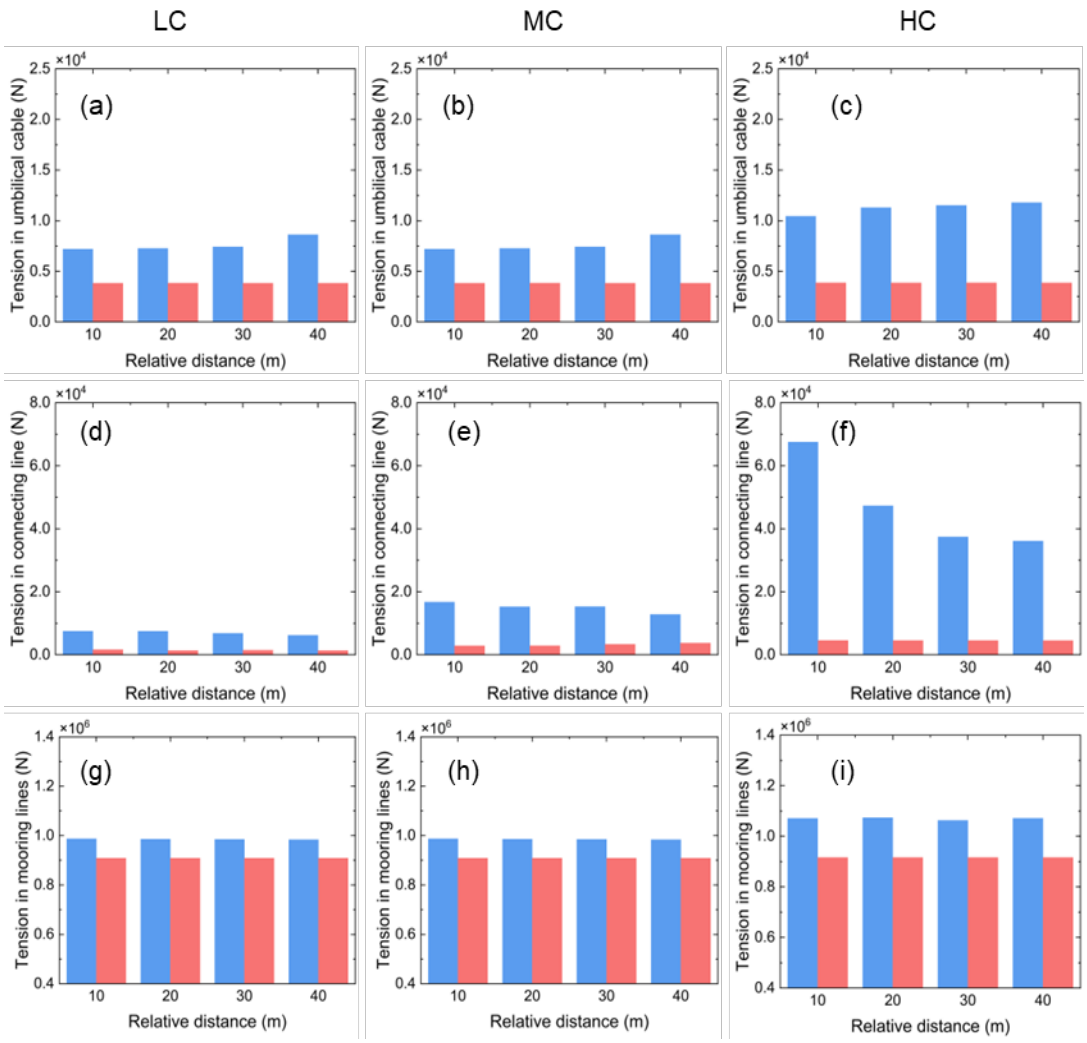


Figure 6.3 The maximum and mean tension in umbilical cable, connecting lines and mooring lines under different relative distances in sea condition LC, MC and HC.

It can be seen in Figure 6.3(a)-(c) that the maximum tension in umbilical cable used for ROV launch and recovery increases with the relative distance under all sea conditions, whereas the mean tension remains relatively constant at approximately $0.4\times10^4$ N. This phenomenon occurs because the ability of wind turbine to restrict vessel movement diminishes as the relative distance increases, resulting in larger motion amplitudes of the support vessel. The increase in maximum tension in umbilical cable is gradual and rather modest under LC and MC scenarios. However, it increases more rapidly under HC condition, rising from proximately $1.6\times10^4$ N (10 m) to $2.1\times10^4$ N (40 m) as shown in Figure 6.3(c).

The mean tension of connecting lines remains approximately constant with varying relatively distance under each sea condition, with approximate values of $1.4\times10^4$ N (LC), $3.3\times10^4$ N (MC), and $4.5\times10^4$ N (HC) respectively (see Figure 6.3(d)-(f)). The maximum tension of connecting lines exhibits a slight decrease with increasing relative distance under LC and MC conditions. However, it decreases more rapidly under HC conditions, falling from approximately $6.8\times10^4$ N (10 m) to $3.6\times10^4$ N (40 m) as shown in Figure 6.3(f). This significant reduction in maximum tension can be attributed to the increased relative distance diminishes the complex coupling effects between support vessel and floating wind turbine. Therefore, appropriately increasing the relative distance can effectively reduce the maximum tension of connecting lines. It is worth noting that the relative distance is also constrained by other conditions such as the overall configuration and arrangement of the wind turbines in the farm.

As illustrated in Figure 6.3(g)-(i), the maximum tension of mooring lines remains relatively constant as the relative distance increases, showing approximate values of $0.99\times10^6$ N (LC), $1.07\times10^6$ N (MC), and $1.19\times10^6$ N (HC) respectively. Similarly, the mean tension of mooring lines also remains stable at $0.91\times10^6$ N (LC), $0.92\times10^6$ N (MC), and $0.94\times10^6$ N (HC) for the corresponding sea conditions. This consistency is because the SPMS method adopted and the deployment of ROV on board a relatively small OSV have minimal impact on the mooring lines.

## 6.3 Effect of wind-wave misalignment

Wind-wave misalignment can exacerbate the tilting and swaying of offshore structures and reduce stability, complicating operations and raising accident risks, especially during installation and maintenance phases in offshore engineering. In the present study, the direction of wind wave is fixed at 0°, while the wind direction ranges from 0° to 180°. It is noted that the range from 0° to 40° is divided into finer increments since this covers 95% of the wind-wave direction difference observed at sea (Bachynski et al., 2014), and the remaining range is divided into coarser increments. The maximum tension in umbilical cable, connecting line and mooring line under the LC, MC, and HC condition with different wind-wave misalignment is shown in Figure 6.4.

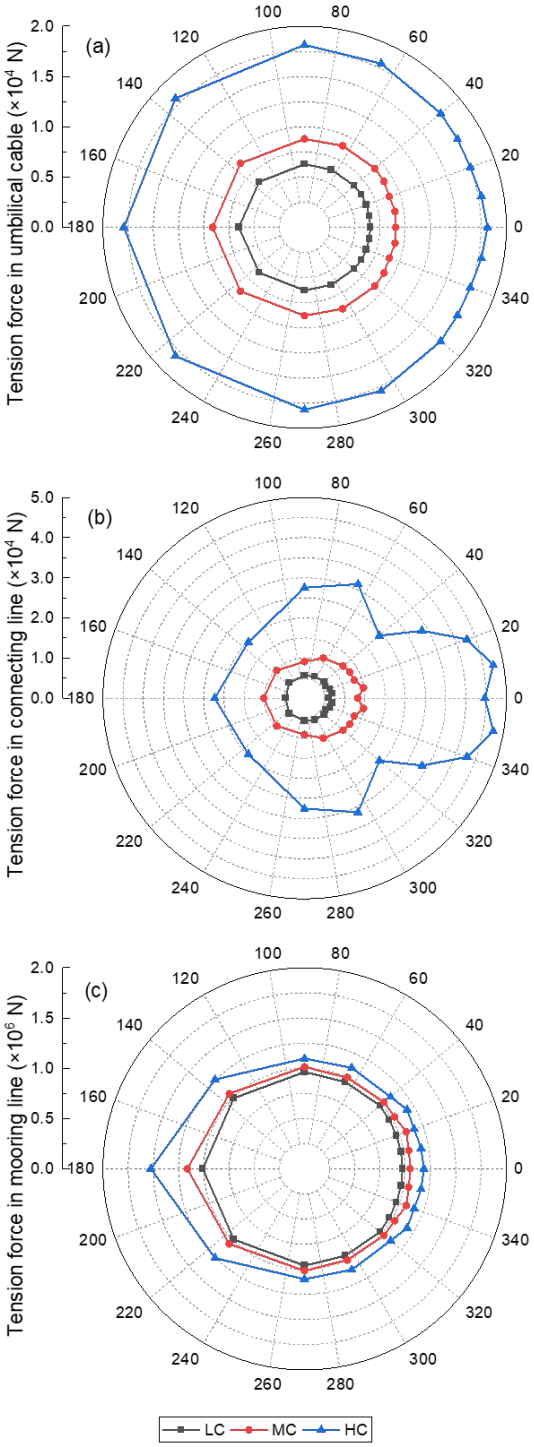


Figure 6.4 The maximum tension force in umbilical cable (a), connecting line (b) and mooring line (c) under the LC, MC, and HC condition with different wind-wave misalignment.

It can be observed in Figure 6.4(a) that the maximum tension in umbilical cable remains relatively stable during the launch and recovery of ROV under different wind and wave

directions, with values approximately at $0.7\times10^4$ N (LC), $0.9\times10^4$ N (MC), and $1.8\times10^4$ N (HC) respectively. This indicates that wind and wave misalignment have minimal impact on the deployment of ROV. The maximum tension in mooring lines of floating wind turbine increases slightly as environmental conditions worsen, but it remains around at $1.0\times10^6$ N (LC), $1.1\times10^6$ N (MC), and $1.2\times10^6$ N (HC) in Figure 6.4(c) under respective conditions. The maximum tension in mooring lines reaches its maximum value when the wind direction is at 180° for a wave direction at 0°, but this scenario is very rare if not completely impossible in reality. The maximum tension in connecting lines increases and then decreases with varying wind and wave conditions, particularly under HC condition as shown in Figure 6.4(b). In the present case study of the OSV and the FOWT, the maximum tension peaks at approximately 10 degrees with a tension value of $4.5\times10^4$ N, and it reaches its minimum at around 40 degrees, with a value of $2.4\times10^4$ N. Noting that the different force scale used in Figure 6.4(a)-(c), the maximum mooring line tension is the highest across all sea conditions among the three slender bodies (umbilical cable, connecting lines and mooring lines) in the coupled offshore system analyzed. The maximum tension in connecting lines is lower than that of umbilical cable under LC condition, but higher under MC and HC conditions.

## 6.4 Dynamics of SPMS connecting line for floating and fixed wind turbine

As the key element to the safe operation by using the SPMS method, the tension in connecting line for both floating and fixed wind turbines based on the SPMS method is further examined. In this section, the same floating wind turbine model is applied to the fixed wind turbine, but with its six degrees of freedom restricted, and other conditions remaining consistent to that in Section 6.1. Figure 6.5 compares the tension in connecting lines between operation with floating and fixed wind turbines under various conditions while a further comparison of connecting line tensions under different wind-wave misalignment conditions for both types of turbines is presented in Figure 6.6.

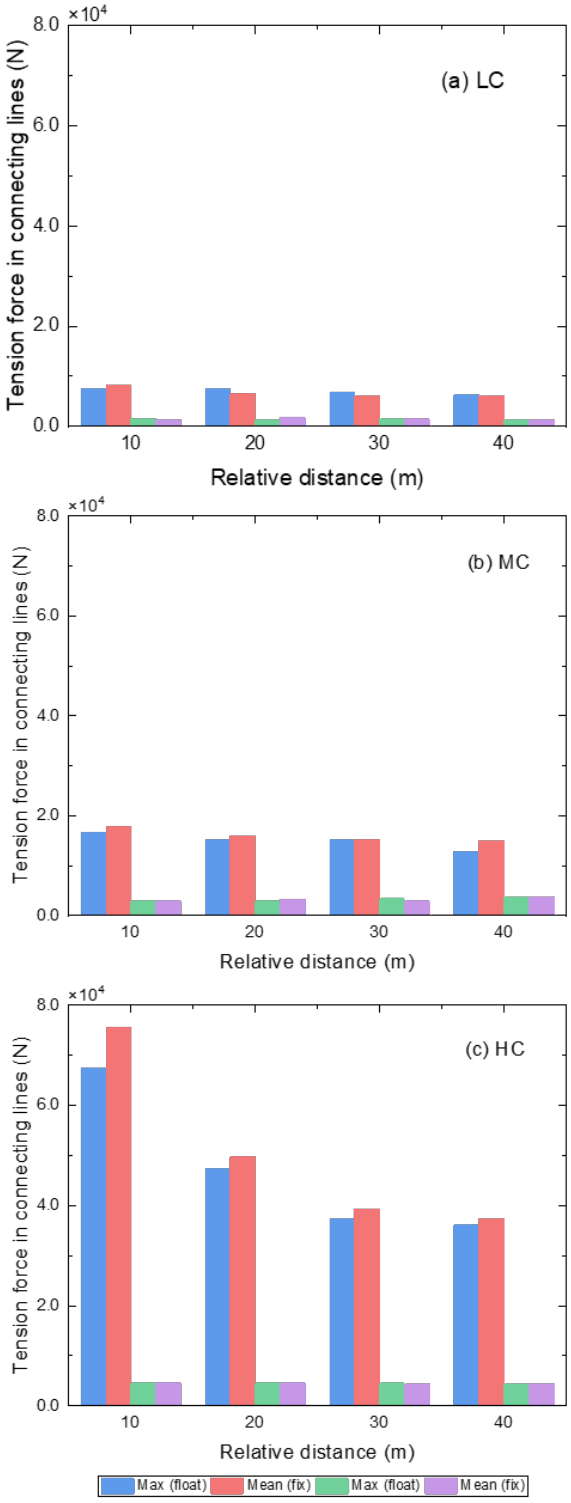


Figure 6.5 The comparison of maximum and mean tension in connecting lines between floating and fixed wind turbines under LC (a), MC (b) and HC (c) conditions.

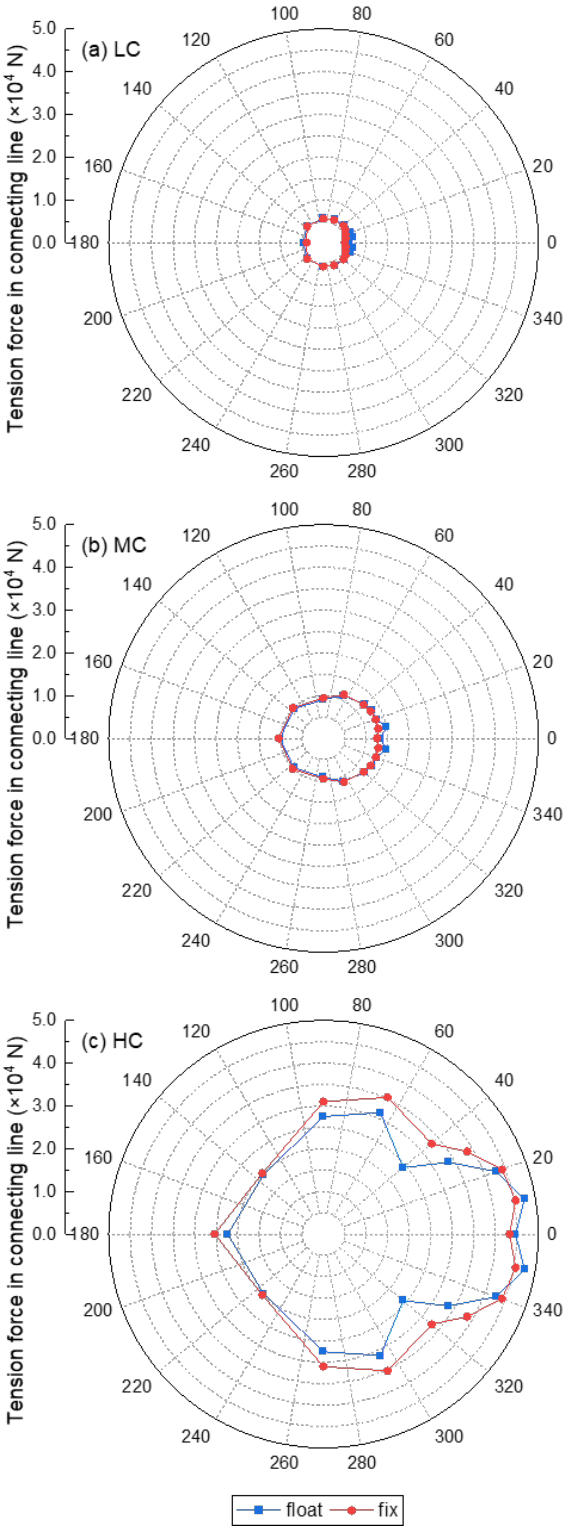


Figure 6.6 The comparison of maximum tension in connecting lines between floating and fixed wind turbines under LC (a), MC (b) and HC (c) conditions with different wind-wave misalignment.

In Figure 6.5 and Figure 6.6, "float" represents the floating wind turbine, "fix" denotes the fixed wind turbine. The mean tension in connecting lines remains nearly equal between floating and fixed wind turbines under various conditions and different relative distances in Figure 6.5. However, the maximum tension in connecting lines shows different trends. For floating wind turbine, the maximum tension in connecting lines is slightly higher than that of fixed wind turbine under LC condition, as shown in Figure 6.5(a). The maximum tensions for both wind turbine types are nearly identical under MC condition (see Figure 6.5(b)). However, the maximum tension in connecting lines for fixed wind turbine is significantly higher than that of operating with floating wind turbine under HC condition as shown in Figure 6.5(c), especially at a relative distance of 10 m, where the difference reaches $0.8\times10^4$ N. It is noted that the difference will gradually decrease as the relative distance increases. This indicates that as ocean environmental conditions worsen, difference in the maximum tension in connecting lines between floating and fixed turbines becomes more pronounced, with fixed wind turbines experiencing the highest maximum tension in their connecting lines.

The maximum tension in connecting lines for both floating and fixed wind turbines under LC condition is very close, maintaining around $0.5\times10^4$ N under different wind-wave misalignment conditions as shown in Figure 6.6(a). Similar to the trend under LC condition shown in Figure 6.6(a), the maximum tension in connecting lines for both floating and fixed wind turbines under MC conditions is generally the same, as shown in Figure 6.6(b). However, at a 10-degree misalignment angle, the maximum tension in connecting lines for operating with floating wind turbine is slightly higher than that for fixed wind turbine. The maximum tension in connecting lines shows significant differences in both floating and fixed wind turbines under HC condition due to wind-wave misalignment, as shown in Figure 6.6(c). For floating wind turbine, it increases to the maximum value of about $4.5\times10^6$ N (10 degree) and then decreases to the minimum value of approximately $3.3\times10^6$ N (40 degree) as the common misalignment angle increases (0-40 degrees). The tension in connecting lines for operating with fixed wind turbine exhibits a similar trend, but the maximum tension in connecting lines is lower than that for floating wind turbine between 0 and 15 degrees. However, from 15 to 40 degrees, it evident that the maximum tension of a fixed wind turbine exceeds that of a floating wind turbine.

To ensure the safety and efficiency of ROV deployment using the SPMS method on a FOWT, operations should fully consider environmental conditions, proactively assess variations in wind speed, wave height, and ocean currents. In HC condition, the tension in mooring and connecting lines increases significantly and requires close monitoring. Although the presence of SPMS has minimal impact on the mooring line tension of the FOWT, the tension in connecting lines increases with worsening wave conditions, necessitating a design that can withstand peak tension under different sea states. The relative distance between the OSV and the FOWT is critical for the safe operation of the ROV, and it is recommended to maintain a range of 20 m to 40 m to balance operational efficiency and safety. A distance of less than 10 m may increase the risk of collision, while a distance greater than 40 m may complicate ROV control. Particularly under HC conditions, appropriately increasing the relative distance can effectively reduce the tension in the connecting lines, which decreases significantly as distance increases. In wind-wave misalignment conditions, although the tension in the ROV umbilical cable and mooring lines remains relatively stable, the tension in connecting lines is significantly affected by wind direction, generally peaking at a 10° wind angle, while extreme conditions such as a 180° wind angle should be avoided to minimize operational risks. Additionally, to ensure operational safety, the SPMS connecting lines should be rated for peak tension under HC conditions, the monitoring frequency of umbilical cables and connecting lines should be increased during ROV deployment, and appropriate operational windows should be selected based on environmental forecasts to reduce risks and enhance operational reliability.

# 7 Conclusions and recommendation of future work

## 7.1 Conclusions

The deployment of a work class ROV from the small offshore service vessel based on single point mooring system method is studied using the newly developed numerical model for dynamics analysis of coupled multi-structure interaction problem. Key technical aspects crucial to the safe operation, including effects of winch speed and deployment position on the wire tension during launch and recovery process of ROV are investigated based on numerical simulation. The present numerical model is validated against experimental results of calm water and regular waves on a 1:10 scaled model tests conducted in a wave flume, as well as previous numerical study focused on single point mooring system. The StormGeo weather forecast data at the DanTysk wind farm in May 2020 is used to simulate realistic operating sea state and analyses operational capacity. A comprehensive numerical analysis of the coupled dynamics of an ROV deployment from a small offshore service vessel for inspection and survey of a floating offshore wind turbine using the newly proposed single point mooring system is conducted. The research provides valuable insights into the feasibility and safety of the innovative approach for inspection and maintenance operations in offshore wind farms. A new safe operation envelope is proposed for such category ROV operation onboard small OSV, and recommendations are made to guide the future operation with potential operational window expansion. Key findings include:

1. The safety of ROV deployment is found to be more critical in recovery process than in launch process. Higher winch speed can be used for descending ROV to reduce the operational time, but a lower winch speed for ascending is beneficial to reduce the maximum wire tension. The increase of horizontal distance has a little effect on the wire tension during launch phase. However, the maximum wire tension decreased with the decrease of horizontal distance in recovery stage. The horizontal distance has little influence on the probability of sudden loading, and its main influencing factor is the significant wave height.

2. With the deployment position at the stern, a horizontal distance of 1.0 m, and a winch speed of 0.3 m/s, the new safety strategy can reduce maximum wire tension

effectively, and the ROV operational limit is expanded to a significant wave height of 1.25 m based on the improvement measures. The operational capacity of ROV in this study can be expanded by up to 6.5% annually while ensuring safety of deployment operation.

3. The safe operating envelope of ROV deployment is proposed based on the comprehensive numerical simulation to guide the onboard ROV safe operation of winch speed and horizontal distance under given sea state. It is a significant step forward in improving the ROV safe operation from empirical onboard staff experience-based towards science/technology-based practice. The chart can also be used for potential capability extension of the OSV operation.

4. The presence of OSV and the deployment of ROV have minimal impact on the mooring lines of FOWT, with tension variations remaining within acceptable limits across different sea conditions. The relative distance between OSV and FOWT significantly affects the tension in umbilical cable and connecting lines. Increasing this distance generally reduces the maximum tension in connecting lines but increases the maximum tension in umbilical cable, particularly in harsh environmental conditions.

5. Wind-wave misalignment has a limited effect on ROV deployment operations, as evidenced by the relatively constant maximum tension in umbilical cable across different misalignment angles. The mooring lines of FOWT consistently experience the highest tension forces, followed by the connecting lines, and then the umbilical cable, with some variations depending on environmental conditions.

6. These findings demonstrate that the SPMS method for ROV-based inspection and maintenance operations on FOWTs can be conducted safely under a range of environmental conditions. However, careful consideration must be given to the relative positioning of the OSV and FOWT to optimize the tension distribution in the system.

The study contributes to the growing body of knowledge on cost-effective and sustainable offshore wind farm operations, especially in O&M. It provides a foundation

for further research into optimizing ROV deployment strategies and improving the overall efficiency of offshore wind turbine maintenance.

### 7.2 Suggestions for future work

Although the present thesis covered wide range aspects of the hydrodynamic interactions between a small offshore service vessel and a floating wind turbine using single point mooring system in ROV deployment. There are still limitations on aspects requiring further research and study.

1. Extended Environmental Conditions: Future research should consider a wider range of environmental conditions, including extreme weather scenarios such as hurricanes, typhoons, and severe storms. This will help validate the robustness of SPMS method and ROV deployment in various offshore environments. Additionally, studying the impact of seasonal variations and long-term climate changes on the operational efficiency and safety of the system can provide valuable insights for sustainable offshore operations.

2. Advanced numerical models: developing more sophisticated numerical models that incorporate additional factors such as sediment interaction, biofouling effects, and long-term wear and tear on the umbilical and mooring lines could provide deeper insights into the operational limits and maintenance needs. These models should also consider the effects of marine growth on the structural integrity and hydrodynamic performance of the system. Integrating machine learning algorithms to predict and mitigate potential failures can further enhance the reliability of these models.

3. Field Trials and Real-time Monitoring: Conducting extensive field trials and implementing real-time monitoring systems on OSVs and FOWTs can help gather empirical data to refine numerical models and improve the accuracy of tension predictions in umbilical and mooring lines. Real-time data analytics can also be used to optimize operational parameters and enhance decision-making processes during inspection and maintenance activities.

4. Optimization of ROV Operations: Investigating the optimization of ROV deployment strategies, including the use of autonomous or semi-autonomous ROVs, can enhance the efficiency and safety of inspection and maintenance operations. Research should focus on developing advanced control algorithms for ROV navigation and manipulation in complex underwater environments. Additionally, exploring the integration of ROVs with other robotic systems, such as ASVs, can provide a more comprehensive approach to offshore inspections.

## References

Amaechi, C.V., Wang, F., Ye, J., 2021. Mathematical Modelling of Bonded Marine Hoses for Single Point Mooring (SPM) Systems, with Catenary Anchor Leg Mooring (CALM) Buoy Application—A Review. Journal of Marine Science and Engineering 9, 1179. https://doi.org/10.3390/jmse9111179

Asmara, I.P.S., Sumardiono, N., Wibowo, V. a P., 2020. Safety analysis of mooring Hawser of FSO and SPM buoy in irregular waves. IOP Conference Series Earth and Environmental Science 557, 012003. https://doi.org/10.1088/1755-1315/557/1/012003

Bachynski, E.E., Kvittem, M.I., Luan, C., Moan, T., 2014. Wind-Wave misalignment effects on floating wind turbines: motions and tower load effects. Journal of Offshore Mechanics and Arctic Engineering 136. https://doi.org/10.1115/1.4028028

Bilgili, M., Alphan, H., 2022. Global growth in offshore wind turbine technology. Research Square (Research Square). https://doi.org/10.21203/rs.3.rs-1202466/v1

Bjerkholt, R.F., 2014. Analysis of ROV lift operation (Master thesis). Norwegian University of Science and Technology.

Buckingham, E., 1914. On physically similar systems; illustrations of the use of dimensional equations. Physical Review 4, 345–376. https://doi.org/10.1103/physrev.4.345

Carter, J.M.F., 2007. North Hoyle offshore wind farm: design and build. Proceedings of the Institution of Civil Engineers - Energy 160, 21–29. https://doi.org/10.1680/ener.2007.160.1.21

Chen, B.-Q., Liu, K., Yu, T., Li, R., 2024. Enhancing Reliability in Floating Offshore Wind Turbines through Digital Twin Technology: A Comprehensive Review. Energies 17, 1964. https://doi.org/10.3390/en17081964

Chen, Z., Zhao, T., Jiao, J., Mao, D., 2017. Simulation and Motion Analysis of Deepwater Manifold Lifting. Journal of Marine Science and Technology 25, 10. https://doi.org/10.6119/jmst-017-1226-10

Christ, R.D., Wernli, Sr., R.L., 2014. The ROV manual: A user guide for remotely operated vehicles, Elsevier eBooks. https://doi.org/10.1016/c2011-0-07796-7

Clough, R.W., Penzien, J., Griffin, D.S., 1975. Dynamics of structures.

DNV, 2017. Modelling and analysis of marine operations. Recommended Practice: DNV-RP-H103.

Driscoll, Lueck, R.G., Nahon, M., 2000. Development and validation of a lumped-mass dynamics model of a deep-sea ROV system. Applied Ocean Research 22, 169–182. https://doi.org/10.1016/s0141-1187(00)00002-x

Faltinsen, O.M., Landrini, M., Greco, M., 2004. Slamming in marine applications. Journal of Engineering Mathematics 48, 187–217. https://doi.org/10.1023/b:engi.0000018188.68304.ae

Feng, Z., Allen, R., 2004. Evaluation of the effects of the communication cable on the dynamics of an underwater flight vehicle. Ocean Engineering 31, 1019–1035. https://doi.org/10.1016/j.oceaneng.2003.11.001

Gordon, R.B., Grytøyr, G., Dhaigude, M., 2013. Modeling Suction Pile Lowering Through the Splash Zone. International Conference on Ocean, Offshore and Arctic Engineering 55317, V001T01A010. https://doi.org/10.1115/omae2013-10136

GRi Simulations Inc., 2018. LARS SIMULATION SYSTEM [WWW Document]. GRi Simulations Inc. URL https://grisim.com/products/lars-simulation-training/ (accessed 12.7.24).

Hennessey, C.M., Pearson, N.J., Plaut, R.H., 2004. Experimental snap loading of synthetic ropes. Shock and Vibration 12, 163–175. https://doi.org/10.1155/2005/734345

Hsu, W.-T., Thiagarajan, K.P., Manuel, L., 2017. Extreme mooring tensions due to snap loads on a floating offshore wind turbine system. Marine Structures 55, 182–199. https://doi.org/10.1016/j.marstruc.2017.05.005

Huo, P., Wang, D., Liu, K., 2018. Research on fishtailing oscillations of a single point moored vessel in shallow waters. The 28th International Ocean and Polar Engineering Conference.

IRENA, 2020. Global Renewables Outlook: Energy Transformation 2050 [WWW Document]. URL https://www.irena.org/publications/2020/Apr/Global-Renewables-Outlook-2020 (accessed 7.17.24).

James Fisher Renewables, 2023. Service operation vessels (SOVs): what's the issue? [WWW Document]. URL https://www.linkedin.com/pulse/service-operation-vessels-sovs-whats-issue-jamesfisherrenewables/ (accessed 7.17.24).

Jenssen, F.R., 2015. Dynamic analysis of ROV operation (Master thesis). Norwegian University of Science and Technology.

Jonkman, J., 2010. Definition of the floating system for Phase IV of OC3. https://doi.org/10.2172/979456

Jonkman, J., Butterfield, S., Musial, W., Scott, G., 2009. Definition of a 5-MW reference wind turbine for offshore system development. https://doi.org/10.2172/947422

Jonkman, J., Larsen, T.J., Hansen, A.M., Nygaard, T., Maus, K., Karimirad, M., Gao, Z., Moan, T., Fylling, I., Nichols, J., Kohlmeier, M., Vergara, J.P., Merino, D., Shi, W., 2010. Offshore Code Comparison Collaboration within IEA Wind Task 23: Phase IV

Results Regarding Floating Wind Turbine Modeling. https://doi.org/10.13140/2.1.3576.5768

Ju, X., Amaechi, C.V., Dong, B., Meng, X., Li, J., 2023. Numerical analysis of fishtailing motion, buoy kissing and pullback force in a catenary anchor leg mooring (CALM) moored tanker system. Ocean Engineering 278, 114236. https://doi.org/10.1016/j.oceaneng.2023.114236

Kimiaei, M., Xu, J., Yu, H., 2009. Comparing the Results of a Simplified Numerical Model With DNV Guidelines for Installation of Subsea Platforms. International Conference on Ocean, Offshore and Arctic Engineering 43413, 319–326. https://doi.org/10.1115/omae2009-79356

Lewis, S.G., Hudson, D.A., Turnock, S.R., Taunton, D.J., 2010. Impact of a free-falling wedge with water: synchronized visualization, pressure and acceleration measurements. Fluid Dynamics Research 42, 035509. https://doi.org/10.1088/0169-5983/42/3/035509

Li, L., Parra, C., Zhu, X., Ong, M.C., 2020. Splash zone lowering analysis of a large subsea spool piece. Marine Structures 70, 102664. https://doi.org/10.1016/j.marstruc.2019.102664

Lind, S.J., Stansby, P.K., Rogers, B.D., Lloyd, P.M., 2015. Numerical predictions of water–air wave slam using incompressible–compressible smoothed particle hydrodynamics. Applied Ocean Research 49, 57–71. https://doi.org/10.1016/j.apor.2014.11.001

Lubis, M.B., Kimiaei, M., 2021. Wave flume and numerical test on launch and recovery of ultra-deep-water ROV through splash zone under wave and ship motion. Ocean Engineering 238, 109767. https://doi.org/10.1016/j.oceaneng.2021.109767

Lubis, M.B., Kimiaei, M., Efthymiou, M., 2021. Alternative configurations to optimize tension in the umbilical of a work class ROV performing ultra-deep-water operation. Ocean Engineering 225, 108786. https://doi.org/10.1016/j.oceaneng.2021.108786

Marine Vision S.L, 2021. TMS 8 [WWW Document]. URL https://www.marinevision.es/en/diving-pro/saab/tms_8.html (accessed 7.14.24).

Nam, B.W., Kim, N.W., Hong, S.Y., 2017. Experimental and numerical study on coupled motion responses of a floating crane vessel and a lifted subsea manifold in deep water. International Journal of Naval Architecture and Ocean Engineering 9, 552–567. https://doi.org/10.1016/j.ijnaoe.2017.01.002

Nuernberg, M., Tao, L., Ren, X., Ramzanpoor, I., 2021. Single point mooring for subsea inspections of wind turbine foundations. Energy Technology Partnership (ETP) project report.

Offshore magazine, 2019. Dogger Bank wind farm to rival other offshore projects [WWW Document]. Offshore-mag.com. URL https://www.offshore-mag.com/field-development/article/14054153/dogger-bank-offshore-wind-farm-to-rival-other-offshore-projects (accessed 12.7.24).

OUCO Group, 2024. The Ultimate Guide to Mooring: Define, principle, and tips [WWW Document]. URL https://ouco-industry.com/the-ultimate-guide-to-mooring-define-principle-and-tips/ (accessed 7.17.24).

Ren, X., Tao, L., Nuernberg, M., Ramzanpoor, I., 2022. Interaction of Offshore Support Vessel With Adjacent Offshore Wind Turbine During Maintenance Operation. International Conference on Ocean, Offshore and Arctic Engineering 85932, V008T09A027. https://doi.org/10.1115/omae2022-79109

SAAB, 2021. Cougar-XT Compact [WWW Document]. URL https://www.saabseaeye.com/solutions/underwater-vehicles/cougar-xt-compact (accessed 7.17.24).

Sarkar, A., Gudmestad, O.T., 2010. Splash Zone Lifting Analysis of Subsea Structures. International Conference on Ocean, Offshore and Arctic Engineering 49095, 303–312. https://doi.org/10.1115/omae2010-20489

Sayer, P., 2008. Hydrodynamic loads during the deployment of ROVs. Ocean Engineering 35, 41–46. https://doi.org/10.1016/j.oceaneng.2007.07.005

Sayer, P., 1996. Hydrodynamic forces on ROVs near the Air-Sea interface. International Journal of Offshore and Polar Engineering.

Siemens Gamesa, 2023. SG 14-222 DD Offshore wind turbine [WWW Document]. URL https://www.siemensgamesa.com/global/en/home/products-and-services/offshore/wind-turbine-sg-14-222-dd.html (accessed 7.17.24).

Singh, A.K., Parida, S.K., 2012. Evaluation of current status and future directions of wind energy in India. Clean Technologies and Environmental Policy 15, 643–655. https://doi.org/10.1007/s10098-012-0554-6

SINTEF Ocean, 2022. SIMA documentation [WWW Document]. URL https://sima.sintef.no/ (accessed 7.17.24).

Statista, 2024a. Number of offshore wind farms operating worldwide as of June 2024 [WWW Document]. URL https://www.statista.com/statistics/264257/number-of-offshore-wind-farms-worldwide-by-country (accessed 7.17.24).

Statista, 2024b. Global capacity of offshore wind power 2009-2023 [WWW Document]. Statista. URL https://www.statista.com/statistics/476327/global-capacity-of-offshore-wind-energy/ (accessed 7.17.24).

Thiagarajan, K.P., Yann, N., 2001. Assessment of one company's regulations for offshore lifting operations. All Days. https://doi.org/10.4043/13242-ms

Tran, C., Gushkov, I., Nordvik, K., Røang, S.T., Lysthaug, S.B., Ommani, B., Fossen, T.I., Hassani, V., Smines, V., Johansen, T.A., 2023. Operability analysis of control system for ROV launch-and-recovery from autonomous surface vessel. Ocean Engineering 277, 114272. https://doi.org/10.1016/j.oceaneng.2023.114272

University of Michigan, 2023. Climate Change: Science and Impacts Factsheet [WWW Document]. Center for Sustainable Systems. URL https://css.umich.edu/publications/factsheets/climate-change/climate-change-science-and-impacts-factsheet (accessed 7.17.24).

Valen, M., 2010. Launch and recovery of ROV: Investigation of operational limit from DNV Recommended Practices and time domain simulations in SIMO (Master thesis). Norwegian University of Science and Technology.

Yettou, E.-M., Desrochers, A., Champoux, Y., 2005. Experimental study on the water impact of a symmetrical wedge. Fluid Dynamics Research 38, 47–66. https://doi.org/10.1016/j.fluiddyn.2005.09.003

Zan, Y., Guo, R., Yuan, L., Ma, Q., Zhou, A., Wu, Z., 2021. Experimental study of a suspended subsea module at different positions in the splash zone. Marine Structures 77, 102935. https://doi.org/10.1016/j.marstruc.2021.102935

Zhang, J., Wang, H., 2022. Development of offshore wind power and foundation technology for offshore wind turbines in China. Ocean Engineering 266, 113256. https://doi.org/10.1016/j.oceaneng.2022.113256

Zhang, X., Duan, M., Mao, D., Yu, Y., Yu, J., Wang, Y., 2016. A mathematical model of virtual simulation for deepwater installation of subsea production facilities. Ships and Offshore Structures 12, 182–195. https://doi.org/10.1080/17445302.2015.1123850

Zhao, C., Thies, P., Lars, J., Cowles, J., 2021. ROV launch and recovery from an unmanned autonomous surface vessel – Hydrodynamic modelling and system integration. Ocean Engineering 232, 109019. https://doi.org/10.1016/j.oceaneng.2021.109019

Zhixin, W., Chuanwen, J., Qian, A., Chengmin, W., 2007. The key technology of offshore wind farm and its new development in China. Renewable and Sustainable Energy Reviews 13, 216–222. https://doi.org/10.1016/j.rser.2007.07.004